# Electromagnetically induced transparency with localized impurity electron spins in a semiconductor

Chaubal, Alok

# Electromagnetically induced transparency with localized impurity electron spins in a semiconductor

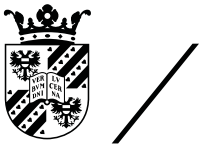

university of groningen

zernike institute for advanced materials

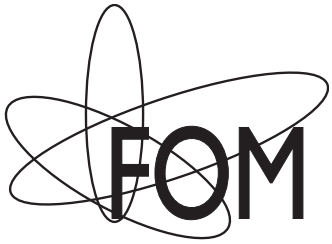



European Research Council

Established by the European Commission

Zernike Institute PhD thesis series 2018-08
ISSN: 1570-1530
ISBN: 978-94-034-0407-3 (printed version)
ISBN: 978-94-034-0406-6 (electronic version)

The work described in this thesis was performed in the research unit Physics of Nanodevices of the Zernike Institute for Advanced Materials at the University of Groningen, the Netherlands. The work was part of the programme *Solid state quantum information processing* of the Foundation for Fundamental Research on Matter (FOM), which is part of the Netherlands Organisation for Scientific Research (NWO). The project was mainly funded by FOM, and did profit from collaboration with projects funded through a Vidi grant from NWO and the national NanoNed and NanoLabNL initiatives. During the final years of this project, it was embedded in a project funded by the European Research Council via ERC Starting Grant 279931.

Thesis cover design: Marloes Viet
Cover page theme: The dancing couple in a starry night is an artistic visualization of a superposition of spin up and spin down for an electron in a GaAs nuclear spin environment.

Printed by: GVO Drukkers & Vormgevers (Ede)

university of groningen

# Electromagnetically induced transparency with localized impurity electron spins in a semiconductor

**PhD thesis**

to obtain the degree of PhD at the
University of Groningen
on the authority of the
Rector Magnificus Prof. E. Sterken
and in accordance with
the decision by the College of Deans.

This thesis will be defended in public on

Friday 16 February 2018 at 11.00 hours

by

Alok Chaubal

born on 20 October 1983
in Mumbai, India

**Supervisor**
Prof. C. H. van der Wal

**Assessment committee**
Prof. B. J. van Wees
Prof. D. Bouwmeester
Prof. S. F. Fischer

*This thesis is dedicated to my father Ulhas V. Chaubal, my mother Naina U. Chaubal, to the loving memories of my late aunt Snehalata V. Chaubal, and to my wife Mayuri Nalawade.*

# Contents

# Chapter 1

# Introduction

## 1.1 Quantum information science

Quantum information science is the part of information science that includes the possibility for information to behave quantum mechanically. Specifically, in digital format, classical information stored in a single bit can have the value 0 or 1. For the quantum case, the state of a bit (in that case named *qubit*) can be 0 and 1 at the same time, according to a quantum state $|\Psi\rangle = \alpha\,|0\rangle + \beta\,|1\rangle$. Here $|0\rangle$ and $|1\rangle$ represent two orthogonal quantum mechanical states (and $\alpha$ and $\beta$ are the probability amplitudes for a superposition state), which can for example be the spin-up and spin-down state of an electron, or two orthogonal polarization states of a photon. In addition, the quantum state of a system with many qubits can contain correlations between qubits (which are then said to be *entangled*) that have no classical analogue [1, 2].

As a research field, quantum information science has seen a strong development [3, 4, 5] since a few discoveries that showed that quantum information processing can perform significantly better than classical information processing. In 1984, Bennett and Brassard discovered the first of several protocols that enable complete protection of communication against eavesdropping [6, 7]. In 1997, Shor and Grover reported algorithms that can speed up certain computational and data-search tasks by many orders of magnitude [8, 9]. However, practical realization and widespread application in society is still under development. The field is showing steady progress, but realizing a large-scale quantum-information system remains challenging. This is mainly because noise from any environment around the qubits rapidly disturbs their quantum state, in particular for systems where one can also accurately and rapidly control the quantum states. Research has thus been focussed on developing qubits that show a good trade-off

between having long-lived quantum states and possibility of control. Quantum information systems with a few qubits have been realized, but scaling these up to many-qubit systems is even more challenging, and this is currently one of the main research topics in this field [3, 4, 5].

## 1.2 Goals and scope of this PhD research

The need for this scalability directed research to realizing qubits in solid state, with the prospect to build on technology and expertise from the semiconductor industry [10, 11]. The research presented in this PhD thesis is part of this development. Rather than directly investigating quantum information functionalities, the research had as goal to develop fundamental knowledge about the possibilities and limitations that come forward when implementing qubits in solid state. High-level control over quantum systems (including light-matter interactions) was initially mainly demonstrated in the fields of atomic physics, laser physics, and quantum optics. The research in this thesis explores similar laser control over systems in solid state, with optically-active systems inside a semiconductor material that have strong similarity with isolated atoms.

The potential relevance for quantum information science is mainly for quantum communication [6, 7]. Here, for many proposals, optical pulses (often called flying qubits) are used to transfer the information, since they travel with the speed of light and interact weakly with their surrounding. However, for high-level performance of such systems, a quantum communication network needs memory nodes that can store quantum information on long-lived states in matter, such as electronic or nuclear spin states [12, 13, 14]. To realize this, one needs to address the challenge to transfer the quantum information contained in an optical pulse onto a spin state, and to transfer it back from the spin onto a next optical pulse when needed [15]. Such dynamics was already widely studied with systems from atomic physics [16, 17, 18]. This PhD research explored whether it can also be implemented with spins in solid state.

The work thereby addresses two main challenges. First, the need for having optically-active material with spin degrees of freedom that have a very long coherence time. Second, the need for having such a material with spins that can also give a very strong interaction between spins and optical pulses. In several experiments strong coupling is realized by placing the material in a high-finesse optical cavity. However, it is technologically very demanding to fabricate and tune such cavities [19, 20, 21]. This thesis has relevance for an alternative ap-

proach, where the strong coupling is realized by working with an ensemble of (ideally) identical qubit systems, that together act as one functional qubit and together form a medium with high optical density. Earlier proposals showed that this provides a route to very robust quantum-optical control schemes that can be applied for preparing non-local entanglement between spins, quantum communication, and functions that use strong optical non-linearities [12, 16, 17, 18]. A critical step toward implementing these schemes is the realization of Electromagnetically Induced Transparency (EIT, see below).

For these studies, our material system of choice was the silicon (Si) donor center in the semiconductor gallium arsenide (GaAs), in its neutral charge state. This systems is called the $D^0$ system [22], and behaves as an artificial hydrogen atom (or any other alkali atom) in solid state: it has a single donor electron that is in orbit (localized) around the donor impurity atom, and it has optical transitions to excited states that can be addressed with laser fields (with photon energies that are less than the band gap of GaAs). Via the polarization of the laser fields, or by applying magnetic fields, one can selectively address the spin states of the $D^0$ electron. The rational to work with this material system is that GaAs material can be grown as an ultra-clean single crystal, with a low concentration of Si donor impurities. Further, the physics of semiconductor optics with GaAs has already been studied for decades, as well as the related semiconductor device technology. This together makes GaAs one of the best available material systems for studies of optically controlling quantum states in matter, and quantum-optical interactions with these states.

With this material system, this PhD research investigated laser control of an ensemble of $D^0$ systems. This has a strong analogy with addressing a vapor of alkali atoms, but the differences with the solid-state version bring some interesting advantages and open questions. A first advantage is that the $D^0$ systems are at fixed positions in the solid, while experiments that address a vapor of alkali atoms suffer from atoms drifting out of the control volume. Further, the GaAs version can easily be implemented in micrometer-scale GaAs structures, while atomic vapors need control systems (vacuum spaces) that are large and difficult to operate. However, operating such an atom-like ensemble in solid state possibly also brings new limitations for using them as qubits, and open questions on the physics that governs their behavior. This thesis addresses four topics for this line of research.

**1)** (*Chapter 2*) The realization and study of *Electromagnetically Induced Transparency* (EIT) with a $D^0$ ensemble. EIT is a two-laser control technique where two lasers together (both with high photon energies) can control the quantum state of an electron spin (with two states at much lower energies that can have long-lived quantum coherence). EIT is a fundamental effect that underlies many quantum-enhanced functionalities that use both long-lived spin states and optical signals, and has been widely studied with alkali-atom vapors [18]. EIT can also give extreme non-linearity for an optical medium, and a dynamical form of EIT can be operated as a storage technique for optical pulses [16, 17, 18]. Chapter 2 reports the first realization of EIT with a semiconductor, and several aspects that limit the quality of EIT with GaAs $D^0$ systems.

**2)** (*Chapter 3*) A spectroscopic study of the optically-excited state manifold of the $D^0$ system. While earlier work already described the structure of the $D^0$ excited state, our EIT experiments showed that identifying these levels in EIT experiments is nontrivial and requires new spectroscopic studies. In addition, better understanding of these levels, and the optical transitions to these levels, is essential for optimizing EIT-type control of GaAs $D^0$ systems.

**3)** (*Chapter 4*) Developing how EIT can be used as a tool for controlling and detecting interactions between $D^0$ electron spins and the nuclear spins of Ga and As atoms in their direct vicinity. In an alkali atom, the active outer electron has hyperfine interaction with one nuclear spin. However, the orbital cloud of the $D^0$ electron in GaAs has a radius that is about a factor 20 larger, and it thus covers many GaAs lattice sites. All Ga and As atoms have nonzero nuclear spins. Consequently, each $D^0$ electron spin has hyperfine interaction with about $10^5$ nuclear spins. Understanding the physics of these interactions is essential for optimal application of $D^0$ electron-spin states. This chapter reports how EIT can be used to control and study these hyperfine interactions.

**4)** (*Chapters 5 and 6*) The studies of EIT effects in micrometer-scale GaAs structures required new dedicated experimental setups and instruments. Chapters 5 and 6 report on the development and testing of these experimental setups and instruments.

The remainder of this first chapter provides a further introduction to the research field and the contents of this PhD thesis.

## 1.3 The $D^0$ system in GaAs

### 1.3.1 Bulk GaAs and the $D^0$ system

This section provides a further introduction into the properties of the $D^0$ system in GaAs, as formed by Si donor atoms at low concentration. In that case, for the material at temperatures below about 10 K, and without background light, the Si donors will not be ionized, and thus form centers where single excess (donor) electrons are localized in the GaAs host. Further, the Si atoms fit in the GaAs lattice, all in the same way, replacing Ga atoms. Consequently, when the GaAs host is a single crystal and kept strain free in further processing, the quantum systems formed by the Si $D^0$ systems all have nearly identical properties: as compared to many other optically-active centers in solid state such a $D^0$ ensemble is typically very homogeneous for properties like its energy-level spacings.

High-quality and high-purity GaAs crystals with a low concentration of intentional Si doping can be grown with molecular-beam epitaxy (MBE) techniques. For the research in this thesis we uniquely worked with MBE-grown material from the group of A. D. Wieck and D. Reuter at the Ruhr University Bochum, Germany. In our materials, the concentration of Si donors was typically around $3 \times 10^{13}$ cm$^{-3}$, which corresponds to an average distance of about 180 nm between the Si donors (while the $D^0$ electron orbit has a radius of about 10 nm). A background of other impurity atoms had a total concentration that was about a factor 100 lower, and mainly carbon.

GaAs is a semiconductor with a direct band gap, meaning that it has strong optical transitions for excitations from the top of the valence band to the bottom of the conduction band. For such optical transitions across the gap, there are clear selection rules that correlate the polarization of optical fields to the spin of charge carriers involved in the transition [22, 23]. Already several decades ago it was studied how this can be used for optical orientation of electron spins in bulk GaAs, and how this can in turn also polarize nuclear spins [24]. More recently, with pump-probe (preparation-detection) pulsed-laser control, time-resolved studies of these effects showed that spin coherence of free conduction-band electrons can have dephasing times in excess of 100 ns [25]. Besides the photo-excitation of free charge carriers, optical excitation can lead to the formation of excitons (hydrogen-atom-like bound electron-hole pairs). For the exciton in its lowest energy state, this is an excitation with an energy of the bulk band gap (1.519 eV at low temperatures) minus the exciton binding energy (4.2 meV) [23]. These

optical properties for bulk GaAs will still play a role for the localized $D^0$ systems, with optical transitions just inside the bulk GaAs band gap.

The $D^0$ system is a shallow donor. When not ionized and with the donor electron in its ground state, the electron is in a localized state with an energy that is 5.8 meV below the bottom of the conduction band. This is the binding energy of the donor electron to the Si core ion. The bound states of this hydrogen-like system are well described with effective-mass theory [22], using the time-independent Schrödinger equation

$$\Big( -\frac{\hbar^2 \bigtriangledown^2}{2m_e^*} - \frac{e^2}{4\pi\epsilon_0\epsilon_r r}\Big) F_n(\overrightarrow{r}) = E_n F_n(\overrightarrow{r}), \tag{1.1}$$

for describing the envelope wave function $F_n(\overrightarrow{r})$ and energies $E_n$. Here $m_e^*$ is the effective mass of the electron in GaAs (0.067 $m_e$, where $m_e$ is the free electron mass). Further, $e$ is the electronic charge, $\epsilon_0$ is the permittivity of the free space, $\epsilon_r$ is the relative permittivity for GaAs (12.56), and $n$ labels the quantum number. The quantized energies $E_n$ have values (with respect to the bottom of the conduction band) that can be expressed as

$$E_n = -\frac{m_e^*}{m_e}\frac{1}{\epsilon_r^2}\frac{R_H}{n^2}. \tag{1.2}$$

Here $R_H$ is the Rydberg constant for the hydrogen atom (13.6 eV). This yields the 5.8 meV binding energy for the system in its $n = 1$ ground state. For the ground state $F_n(\overrightarrow{r})$ has a form similar to the $1s$ ground state of hydrogen (Fig. 1.1). However, its Bohr radius is significantly larger ($a_0$ = 9.9 nm) due to the low value for the effective mass and the high value for the relative permittivity. This justifies the effective-mass approach. Note that for the full wave function of the $D^0$ electron $F_n(\overrightarrow{r})$ must be multiplied with a Bloch function, which then describes the structure in the wave function at the scale of the lattice periodicity (lattice constant is 0.565 nm) [23].

### 1.3.2 $D^0$-$D^0X$ optical transitions

For optical control and probing of the $D^0$ system we will consider excitations to a state where an additional exciton ($X$) is bound to the $D^0$ system, see Fig. 1.1. This excited system is denoted as $D^0X$, often called the (neutral) donor-bound exciton, but sometimes also referred to as a bound trion system (Fig. 1.1). This $D^0X$ system can thus be seen as an atom with three interacting charge carriers, but analyzing its energy eigenstates is much more complex due to the solid-state

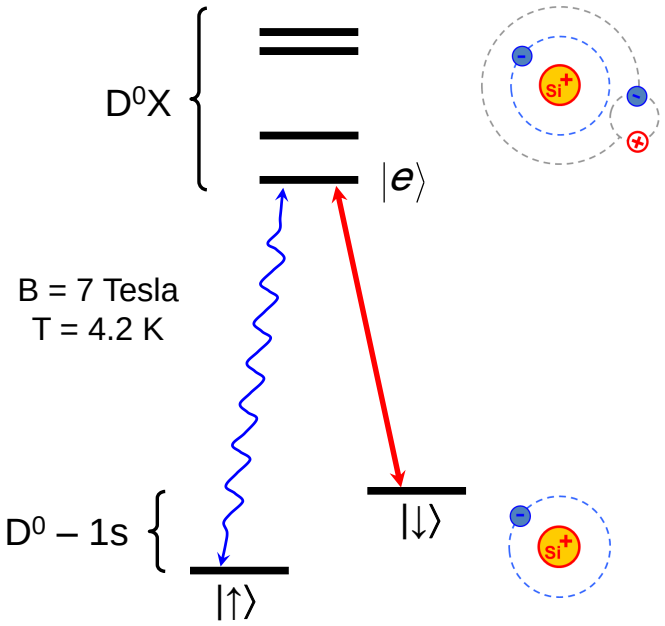


**Figure 1.1:** Level scheme (left) and cartoon representations (right) of the $D^0$ and $D^0X$ energy eigenstates in a magnetic field of 7 T. For the $D^0$ ground state we only consider the lowest-energy orbital state ($1s$ envelope wave function). The $D^0$-$1s$ state has two energy levels, the Zeeman-split states spin-up $|\uparrow\rangle$ and spin-down $|\downarrow\rangle$ for the localized electron. The optically excited states are a series of levels for the $D^0X$ complex, which has an additional electron-hole pair (exciton, $X$) bound at the $D^0$ site. With two electrons and one hole in a three-body bound state around the Si core ion, these $D^0X$ states are also referred to as trion states. The arrows in the level scheme represent laser fields that drive transitions between the levels, selectively addressing the $D^0$ spin states and one level $|e\rangle$ of the $D^0X$ complex.

environment. This $D^0X$ system was extensively studied before, both in theory and in experiment. Part of this work identified valid approximations for the description, and it showed good agreement between experiment and a theoretical framework for analysis. Still, the complexity of the system is too high for a general theoretical description (either analytical or numerical) that cover all aspects (such as magnetic field dependence). New investigations in this area are presented in Chapter 3.

The $D^0X$ system has many energy eigenstates. In a magnetic field of about 7 T, the lowest levels appear as well-separated lines in spectroscopy (typically at least 6 lines can be observed). The splittings correspond to typical values for electronic Zeeman splittings. For an order of magnitude of the energies, we consider here further the case of zero magnetic field. The energy of a $D^0$-$D^0X$

transition (assuming lowest energy eigenstate for both) is then the GaAs band gap, minus the free-exciton binding energy, minus the binding energy of the exciton to the $D^0$ system (and a further small correction from interactions and re-arrangement of the three charge carriers). These are all terms at the few meV scale, and experimentally the spectral line of the $D^0$-$D^0X$ transition appears 0.9 meV lower in energy than the transition for creating $n = 1$ free excitons, at an energy of $\sim(4.2 + 0.9) = 5.1$ meV below the band gap [23] (see Fig. 2.1(a)). The wavelength difference for the $X_{n=1}$ and $D^0$-$D^0X$ transition thus corresponds to $\triangle\lambda = 55$ Å, with the central wavelength for $D^0$-$D^0X$ at ∼8188 Å (small shifts are observed due to strain). In an applied magnetic field of $B = 7$ T, the Zeeman splitting $E_Z = g\mu_B B$ for the $D^0$ electron is 0.166 meV, which corresponds to a shift in wavelength of about 0.9 Å (where the $D^0$ g-factor is $g = -0.42$ [26, 27], and $\mu_B$ is the Bohr magneton).

### 1.3.3 Lambda system

For getting EIT-type control, the $D^0$-$D^0X$ must be operated as a *lambda system* (a three-level scheme that resembles the Greek letter Λ, see Figs. 1.1, 1.3). This is realized by applying a field of about 7 T to the GaAs material, which Zeeman splits the two spin states $|\uparrow\rangle$ and $|\downarrow\rangle$ of the $D^0$-1$s$ system (Fig. 1.1). These two spin states both have dipole-allowed optical transitions to the $D^0X$ complex, and often both to the same level $|e\rangle$ of this complex. For realizing a lambda-type control scheme, we tune two lasers such that each drive a transition from one of the states $|\uparrow\rangle$ and $|\downarrow\rangle$ to the same level $|e\rangle$ (we mostly work with one of the lowest levels $|e\rangle$ of $D^0X$, Fig. 1.1). Most of the lowest optical transitions only couple to laser fields with a particular polarization (Chapter 2).

### 1.3.4 Experimental considerations and setup

Before further describing the EIT control scheme that we aim to investigate with $D^0$ ensembles, we use the properties described till now for listing the implications for experimental work on this system. First, the requirement to avoid ionization of a significant fraction of the $D^0$ systems and (since our experiments use the excited states) $D^0X$ systems gives in practice that the temperature should be well below 10 K. This is most conveniently implemented by doing all experiments in a helium bath cryostat (4.2 K sample temperature). This also allows for using superconducting magnets for applying tunable fields of about 7 T in the sample volume. These two aspects together compromise the ease of optical access: the

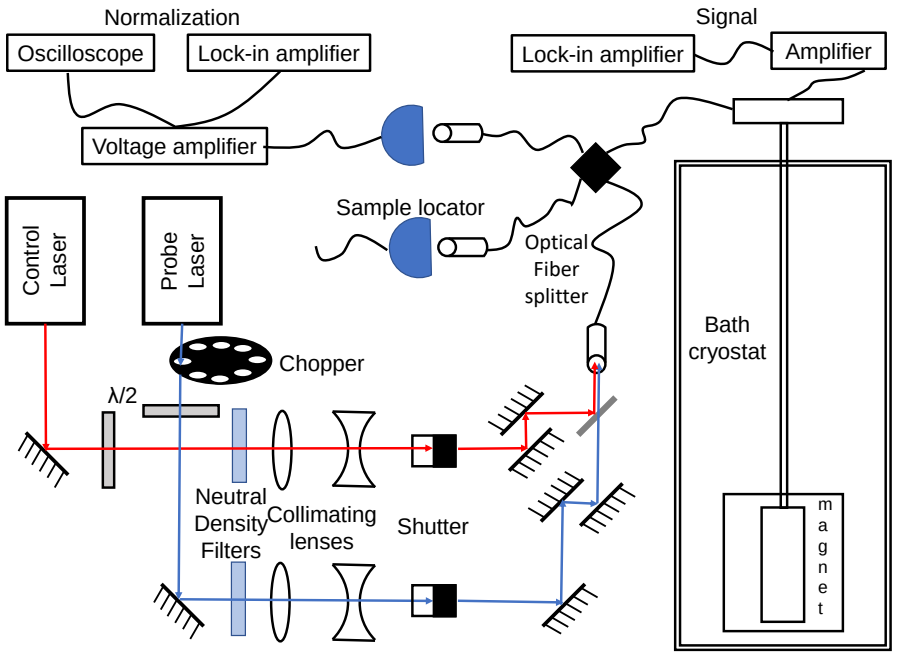


**Figure 1.2:** Schematic of the the experimental setup, see main text for details. Further details and a photograph of parts inside the bath cryostat are presented in Fig. 5.1.

sample volume is deep inside a cryostat, and it is limited in size due to the surrounding magnetic coil (a cylinder of 50 mm diameter, see Fig. 5.1). Still, it is needed to deliver and extract optical fields to this sample volume with well-defined optical polarizations and beam profiles.

For this approach, we build a dedicated experimental setup where laser fields reach the sample volume via polarization maintaining fibers, while light could also be coupled out of the measurement volume via fibers (see Fig. 1.2, more detailed descriptions are presented in Chapters 5 and 6). In the sample volume, for a typical experiment, we mounted small lenses and a transparent heat-sinked sapphire working surface, on which we adhered a 10 $\mu$m-thick GaAs layer (simply using Van der Waals adhesion, as an approach to get low strain in the GaAs layer from its mounting). This allowed for optical transmission experiments with the GaAs layer. Compact piezo motors in the sample volume were applied for focussing the laser fields to micrometer-scale spots (see Fig. 5.1), and allow for focussing on different areas of the GaAs layer.

Figure 1.2 presents the overall experimental setup in one of its typical forms. Several aspects were varied or improved during the course of the research, and this will be specified along with specific results in the chapters of this PhD thesis. Essential instruments and functionalities in the schematic of Fig. 1.2 are as

follows. Two tunable lasers with 75 kHz linewidth with 50 GHz mode-hop-free scanning capability (optimized for use around 820 nm wavelength) provided the optical fields. Half-wave-plates were used in the laser path to define linear polarizations. A chopper was used to modulate the scanning probe laser (but for part of the measurements we used the chopper in the beam of the fixed control laser). Collimating lenses were used to shape the beam and minimize its divergence. The laser light was steered into the fiber-optic-coupler using mirrors and beam splitters. A polarization-maintaining optical-fiber beam splitter was used. It has three channels excluding the input channel. One channel was used to connect another polarization-maintaining optical fiber to steer light into the bath cryostat. Inside the cryostat, light falls on the sample and transmitted light was detected using a photodiode in the sample volume (or steered to detectors outside the cryostat via additional optical fibers). The signal from the photodiode was amplified and detected using a lock-in amplifier. The second channel of the optical-fiber beam splitter was used as a normalization channel. The normalization channel was coupled to a photodiode with amplifier and was further connected to an oscilloscope and lock-in amplifier. The third channel could be used to detect reflection from the sample. This was only used for locating and positioning the sample inside the cryostat.

## 1.4 Electromagnetically induced transparency

Electromagnetically induced transparency (EIT) is the phenomenon that an absorbing optical transition becomes transparent for a probe-laser field because destructive quantum interference in the dynamics of a quantum system prohibits populating the optically excited state. The destructive quantum interference can occur because two laser fields (the probe laser field, and a control laser field) both drive optical transitions. EIT can occur with three-level systems as in Fig. 1.3(a), for which it is essential that the two low-energy spin states can have a long-lived quantum coherence and that one can selectively address the two optical transitions. In Fig. 1.3(a) this is depicted for the Zeeman-split spin states of the $D^0$ system and one of the lowest states $|e\rangle$ of the $D^0X$ complex.

A homogeneous ensemble of these systems can become transparent for the probe laser when it meets the condition for two-photon Raman resonance with the applied control laser (the difference in laser photon energy exactly matches the energy splitting between $|\uparrow\rangle$ and $|\downarrow\rangle$). Under these conditions the systems are trapped in a dark state, which is in the case of ideal spin coherence the quantum

superposition state

$$|\Psi_{dark}\rangle = \frac{\Omega_c |\uparrow\rangle - \Omega_p |\downarrow\rangle}{\sqrt{|\Omega_c|^2 + |\Omega_p|^2}}, \tag{1.3}$$

where $\Omega_c$ (control) and $\Omega_p$ (probe) are the Rabi transition frequencies associated with the driven optical transitions [18, 28]. The phenomenon is closely related to Coherent Population Trapping (CPT). CPT only concerns the trapping in a dark state upon two-laser driving. EIT concerns the optical transmission properties of a medium with identical systems in, or nearly in, a CPT state. Notably, the requirement for homogeneity of energy splittings mainly concerns the ground-state spin splitting, since the two-photon resonance condition is insensitive to shifts of the energy of state $|e\rangle$. Indeed, CPT and EIT are robust against a moderate amount of inhomogeneity for the energy of state $|e\rangle$ (strong inhomogeneity can still comprise EIT when it becomes very much larger than the homogeneous line width of transitions to $|e\rangle$, or when the energy shifts become as large the splitting between $|e\rangle$ and other excited-state levels [18]). This makes EIT-based control schemes robust against a range of technical and material imperfections.

The experimental fingerprint of EIT is shown in Fig. 1.3(b,c). For the description here we assume that fully on resonance the medium has an optical thickness of about 3 (significant absorption, but no strong influence yet on the line width of spectral lines). With only the probe laser on, and frequency scanning it across the $|\uparrow\rangle$-$|e\rangle$ resonance, the transmission spectrum show a single dip (assuming that the probe laser is weak enough to avoid complete optical pumping into the state $|\downarrow\rangle$, as balanced by spin relaxation). The line width corresponds to the dephasing rate for the state $|e\rangle$ (when not significantly power broadened by the laser).

Now assume that both the probe and the control laser are on, and tuned to photon energies near two-photon resonance. When the probe scan passes the detuning of exact two-photon resonance, the lambda systems get trapped in the dark state, and no longer absorb the laser fields. Hence, the medium becomes transparent, which appears in the spectrum as a narrow EIT peak inside the absorption dip. For strong enough control laser and a long spin dephasing time, the transmission is fully restored to unity. The EIT line width can be as narrow as the spin dephasing rate (when not significantly power broadened by the lasers). The spectra in Fig. 1.3(b,c) are calculated with standard EIT theory [18], with parameters that are typical for the $D^0$ system (further discussed in Chapter 2).

For the case of a finite spin dephasing time (in the sense of an inhomogeneous dephasing time $T_2^*$ for a spin ensemble), the EIT peak only develops when the control laser is of high enough intensity: the cycling between the ground state

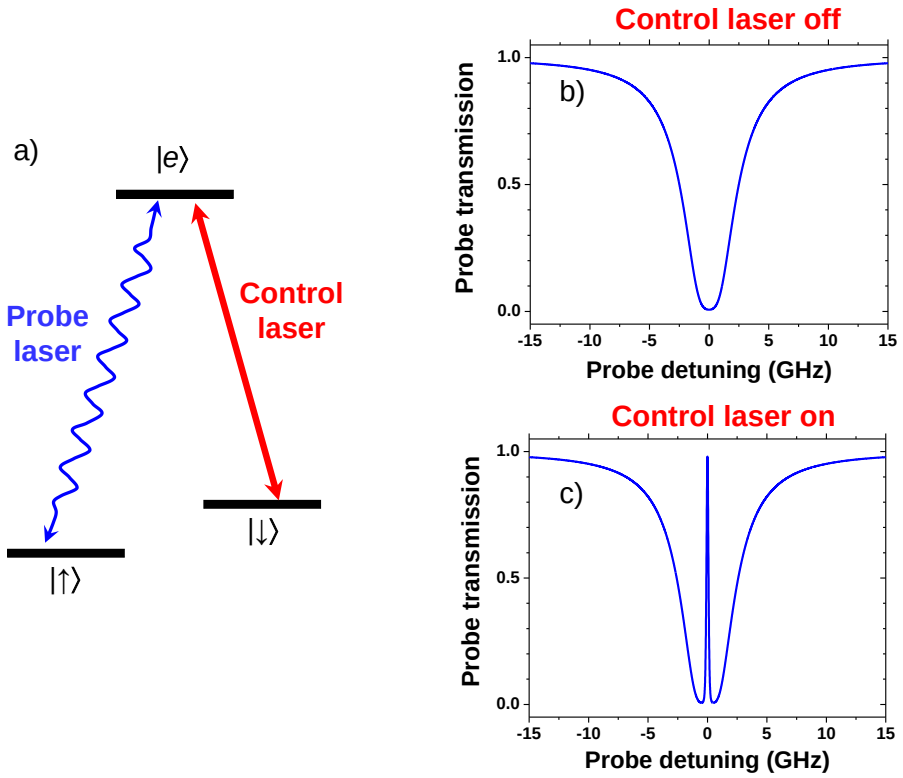


**Figure 1.3:** **(a)** Lambda energy-level scheme with a probe and control laser coupled to the system in a manner that can drive EIT. **(b)** Probe-laser transmission spectrum for the case that the control laser is off (weak probe laser, no complete optical pumping). In that case, the transmission spectrum shows a dip that corresponds to resonance with the $|\uparrow\rangle$-$|e\rangle$ transition. **(c)** Probe-laser transmission spectrum for the case that the EIT control laser is on. In this case, the transmission spectrum shows a sharp peak (the EIT transmission peak) inside the absorption dip of panel (b). The probe frequency scan is referenced with respect to the condition for two-photon resonance (see main text).

and excited state should be fast enough to experience the quantum coherence contained in the superposition of the two spin states, such that the destructive quantum interference in the dynamics can play a role. When assuming that the control laser has a higher intensity than the probe laser ($\Omega_c > \Omega_p$), the condition for getting EIT is (accurate for optical thickness $\lessapprox 1$)

$$|\Omega_c| > \sqrt{\gamma_e \, \gamma_{\uparrow\downarrow}}, \tag{1.4}$$

where $\gamma_e$ and $\gamma_{\uparrow\downarrow}$ are, respectively, the excited-state and spin dephasing rate [18].

For these same conditions, the width of the EIT peak is approximately [18]

$$\triangle_{EIT} \approx \sqrt{\gamma_{\uparrow\downarrow}^2 + |\Omega_c|^2}. \tag{1.5}$$

For systems with slow spin dephasing, EIT can give a very significant yet extremely sharp spectral feature, which is a controllable optical non-linearity: the sharpness of the feature can be controlled via $\Omega_c$. This provides the basis for strong interaction between optical pulses and spin states. More in general, it is a path for controlling absorption and refraction of the medium.

At the start of this PhD research, EIT was most extensively studied with ensembles of alkali atoms. A key result from this field was that it established that EIT gives access to very robust quantum optical techniques for controlling strong correlations between the quantum state of a collective spin excitation in an ensemble and the state of the probe field [12, 16, 17, 18]. Such experiments are technically less demanding than similar quantum optical experiments that use a single atom in a high-finesse optical cavity [19, 20, 21]. In particular, this field realized studies of quantum entanglement between atomic ensembles with several meters spatial separation, with state preparation and readout via a quantum optical measurement scheme [29, 30]. Notably, this was realized only a few years after initial work on EIT applications demonstrated slow light (down to $\sim$17 m/s) [31] and storage of light [32]. The work in this PhD research investigated initial steps for light storage and studies of nonlocal quantum entanglement with spins in solid state [28, 33].

## 1.5 Nuclear environment and dynamic nuclear polarization

The previous section discussed that high-quality EIT needs a spin ensemble with a long dephasing time. For the $D^0$ electrons in GaAs the spin dephasing in mainly due to hyperfine interactions between each $D^0$ electron and about $2 \times 10^5$ nuclear spins within the $D^0$ electron cloud (all stable Ga and As isotopes have non-zero nuclear spin). When the magnetic field is below 20 T and the temperature above a few mK, the state of such a nuclear spin ensemble is that the spins have almost fully randomized orientations at thermal equilibrium. That is, for the thermal-equilibrium conditions as in our experiments the average nuclear spin polarization is very close to zero in all directions. However, when randomly orienting $N$ nuclear spins, there will be statistical fluctuations around zero polarization with

a magnitude of $\sqrt{N}$. Hence, each $D^0$ spin will experience hyperfine interaction with a small non-zero nuclear spin polarization, that has a random value in the range of $\pm\sqrt{N}$ oriented nuclear spins. Via the hyperfine interaction this acts as an effective magnetic field (called Overhauser field) on the $D^0$ spin [34, 35], with a random value in the range $\pm 15$ mT. This results in the spin dephasing time $T_2^* \approx 2$ ns for a $D^0$ ensemble. Notably, when removing this mechanism the spin dephasing times will be in excess of 7 $\mu$s, as demonstrated with optically-controlled spin-echo experiments [36].

Consequently, the $T_2^*$ value for a $D^0$ ensemble can be made longer if the nuclear spins can be driven into a more ordered state. A path to such control can be based on using Dynamic Nuclear Polarization (DNP). DNP is the phenomenon that a nuclear spin ensemble can get polarized due to hyperfine interaction with an electron spin that is driven away from it thermal-equilibrium polarization. When (in part) the electron spin polarization relaxes via hyperfine interaction with the nuclear spins, the polarization of the electron spin will be transferred onto the nuclear spin ensemble. In its most basic form, such a relaxation process is a electron-nuclear spin flip-flop process, where angular momentum is conserved [34]. However, the full dynamics of DNP can be much more complex, with a role for energy and/or angular momentum transfer by control fields, or interactions with a reservoir in the environment. In particular various studies on quantum dots containing a single electron have shown that such DNP can indeed reduce the nuclear spin fluctuations [37, 35].

As further discussed in Chapter 4 of this thesis, we investigated the interaction between EIT driving and the occurrence of DNP, with the prospect to suppress the nuclear spin fluctuations via DNP by using EIT itself [38, 39]. As a first step, we used the EIT control-lasers to create a small nuclear spin polarization via DNP, and also used EIT as a probe for to studying the effect of it on the $D^0$ spin splitting, in a time-resolved manner.

## 1.6 Localized quantum systems in solids

Besides the $D^0$ system in GaAs, several other atom-like or molecule-like systems in solids (often with long-lived spin states) are currently investigated for quantum-information applications. In this section we will shortly review the most significant material systems and developments, and compare the properties to the $D^0$ system in GaAs. We restrict the discussion to optically-active quantum systems in solids.

### 1.6.1 Quantum dots

Optical manipulation of the spin states of single-electron and single-hole [40] systems has been widely studied already with single quantum dots, or ensembles of quantum dots [41]. A good example and important result is EIT-type control with a single quantum dot, that contained one electron [37]. These systems are mostly realized with III-V semiconductors, by growing small islands of III-V material with a lower band gap inside a host material with a higher band gap, such that charge carriers can be localized in the dots, and optical control is possible. The most widely studied example is InAs dots in a GaAs host. Since all stable isotopes that can form III-V semiconductors have non-zero nuclear spin, also in these systems the spins of localized charge carriers always have significant interaction with the ensemble of nuclear spins in the dot material. This implies that hyperfine interactions also contribute to limiting the electronic spin coherence time for III-V dots [37, 42, 35].

As compared to the $D^0$ system, the system-to-system variation due to limited control during quantum-dot growth is much larger (no control at the atomic scale), typically by a factor $10^5$. Also, there are no clear technological prospects to improve on this. Consequently, state-of-the-art results on quantum-communication functionalities were mostly performed with a single quantum dot per functional qubit, and often required delicate tuning of the energy levels when working with more than one dot, or a dot coupled to a particular optical frequency [43, 44, 45, 46]. Still, despite these non-ideal aspects, III-V quantum dots have been studied extensively for quantum applications, since they were among the first material systems available for proof-of-principle studies. This led to demonstrations of various quantum-optical phenomena such as indistinguishable photons, photon bunching, and quantum entanglement between optical pulses and spins in quantum dots [21, 35, 47, 48, 49, 50, 51, 52, 53, 54, 55, 56].

### 1.6.2 Color centers in diamond and silicon carbide

A system that has been widely and very successfully studied as a qubit since 2003 is the nitrogen-vacancy (NV) center in diamond [11, 57, 58]. Driven by its favorable qubit properties, the material and device technology for diamond has been showing a very rapid development in this period as well. This system has very favorable properties: they can be studied as single centers, the optical emission is bright, and it has millisecond spin coherence times (spin echo) up to room temperature. In addition, with NMR and ESR control, advanced quantum

processing with electron-to-nuclear spin-state transfer has been demonstrated. It is a deep defect, and its electronic states are much more localized, roughly at the atomic scale. This also gives less favorable properties. The energy levels show stronger inhomogeneity from local strain variations in the material than the GaAs $D^0$ system. Further, upon optical emission, more than 95% is emitted via a phonon side band. Still, for solid-state qubits, the NV center has shown the most advanced performance, with as state of the art in 2015 a loop-hole free test of Bell inequalities [59] (advanced test of quantum entanglement with two spins widely separated in space).

More recently, a few other color centers with properties similar to the NV center were identified [60]. An interesting example is the divacancy in the wide-band-gap semiconductor SiC. This system also shows millisecond spin coherence times (spin echo) at room temperature, it has its optical transitions near telecom wavelength, and semiconductor device technology is already well developed for SiC [61]. EIT with a SiC divacancy ensemble was recently demonstrated [62].

### 1.6.3 Rare-earth doped crystals

Another interesting class of materials with quantum emitters are rare-earth doped crystals. Here, hyperfine levels can be spectrally resolved, giving access to direct optical control of the nuclear spin of the defect, which can show coherence times in excess of seconds. The optical transitions are weak, but also have a long coherence time. Strong inhomogeneous broadening of the optical transition is typical, but this can be remedied via long-lived spectral hole burning. While material and device technology are here not strongly developed, these systems have shown record performance for optical quantum memories, [14, 63, 64, 65], and very recently the first quantum-optical device structures were reported [66].

### 1.6.4 $D^0$ centers in silicon

Shallow $D^0$ donor systems also occur in silicon. The fact that silicon has an indirect band gap strongly compromises optical control. Despite this limitation, research with the Si $D^0$ system has shown record values for control of spin coherence, since bulk Si material can be isotopically enriched to a form where (nearly) all Si atoms having nuclear spin zero. Such materials can thus be used for studies of long electron spin coherence that is not compromised by hyperfine interactions. Even more interesting is that the $D^0$ electron then only has hyperfine interaction with a single nuclear spin: that of the $D^0$ core ion itself. An experiment on such a

$D^0$ ensemble that combined optical control, electron-nuclear spin-state transfer, and controlled $D^0$ ionization, showed a nuclear spin coherence time of 39 minutes at room temperature [67] (obtained while applying NMR spin-echo corrections).

### 1.6.5 $D^0$ centers in II-VI semiconductors

More recently, the $D^0$ systems in II-VI semiconductors were also investigated as a potential qubit (see for example Ref. [68] on ZnSe). The II-VI semiconductors have typically good optical properties (direct band gap), but with a band gap that is higher than GaAs. Here material technology is not as well developed as for GaAs. An interesting aspect of II-VI semiconductors is that some isotopes of the basic elements have nuclear spin zero. As for silicon, with isotopic enrichment this gives access to studies where hyperfine interactions do not limit electron spin coherence.

### 1.6.6 The $D^0$ system in GaAs: its contributions to the field

Before and in parallel with this PhD research, several other groups worked on the $D^0$ system in GaAs, and their results were of great value for this PhD research. Key examples since 2005 are CPT with $D^0$ ensembles [27, 28], pulsed optical control of spin states [69, 70, 36], and spin-noise spectroscopy [71].

Research on the $D^0$ system in GaAs has relevance for the entire field reviewed in this section. Arguably, a comparison with the other systems presented here indicates that it is not very likely that the GaAs $D^0$ system will come forward as the best platform for quantum applications. Still, besides some weak points, it also has some strong points. It is unique in combining strong optical transitions with a high degree of ensemble homogeneity in state-of-the-art materials. This makes it currently still one of the best systems for investigating EIT physics in solid-state material, while any limitations in EIT can be linked to solid-state properties that are (relative to other available materials) well understood and well controlled.

## References

[1] M. A.Nielsen and I. L. Chuang, *Quantum Computation and Quantum Information* (Cambridge University Press, 2000).

[2] N. D. Mermin, *Quantum Computer Science* (Cambridge University Press, 2007).

[3] For a review of recent developments see: K. Southwell *et al.*, *Quantum coherence - Nature insight*, Nature **453**, 1003 (2008).

[4] For a review of recent developments see: T. D. Ladd *et al.*, *Quantum computers*, Nature **464**, 45 (2010).

[5] For a review of recent developments see: J. Stajic *et al.*, *The Future of Quantum Information Processing*, Science **339**, 1163 (2013).

[6] C. H. Bennett and G. Brassard, *Quantum cryptography: Public key distribution and coin tossing*, Proceedings of IEEE International Conference on Computers, Systems and Signal Processing **175**, 8 (1984).

[7] N. Gisin, G. Ribordy, W. Tittel, and H. Zbinden, *Quantum cryptography*, Rev. Mod. Phys. **74**, 145 (2002).

[8] P. W. Shor, *Polynomial-time algorithms for prime factorization and discrete logarithms on a quantum computer*, SIAM J. Comput. **26**, 1484 (1997).

[9] L. K. Grover, *Quantum Mechanics Helps in Searching for a Needle in a Haystack*, Phys. Rev. Lett. **79**, 325 (1997).

[10] D. D. Awschalom, N. Samarath, and D. Loss (eds.), *Semiconductor Spintronics and Quantum Computation* (Springer, Heidelberg, 2002).

[11] R. Hanson and D. D. Awschalom, *Coherent manipulation of single spins in semiconductors*, Nature **453**, 1043 (2008).

[12] L. M. Duan, M. D. Lukin, J. I. Cirac, and P. Zoller, *Long-distance quantum communication with atomic ensembles and linear optics*, Nature **414**, 413 (2001).

[13] H. J. Kimble, *The quantum internet*, Nature **453**, 1023 (2008).

[14] C. Simon *et al.*, *Quantum memories: A review based on the European integrated project "Qubit Applications (QAP)"*, Eur. J. Phys. D **58**, 1 (2010).

[15] T. E. Northup and R. Blatt, *Quantum information transfer using photons*, Nature Photonics **8**, 356 (2014).

[16] M. D. Lukin and A. Imamoglu, *Controlling photons using electromagnetically induced transparency*, Nature **413**, 273 (2001).

[17] M. D. Lukin, *Colloquium: Trapping and manipulating photon states in atomic ensembles*, Rev. Mod. Phys. **75**, 457 (2003).

[18] M. Fleischhauer, A. Imamoglu, and J. Marangos, *Electromagnetically induced transparency: Optics in coherent media*, Rev. Mod. Phys. **77**, 633 (2005).

[19] M. Mücke *et al.*, *Electromagnetically induced transparency with single atoms in a cavity*, Nature **465**, 755 (2010).

[20] J. McKeever *et al.*, *Deterministic generation of single photons from one atom trapped in a cavity*, Science **303**, 1992 (2004).

[21] K. Hennessy *et al.*, *Quantum nature of a strongly coupled single quantum dot-cavity system*, Nature **445**, 896 (2007).

[22] M. Cardona and P. Y. Yu, *Fundamentals of Semiconductors* (Springer-Verlag, 2001).

[23] M. Fox, *Optical Properties of Solids* ($2^{nd}$ edition, Oxford University Press, 2010).

[24] F. Meier and B. P. Zakharchenya (eds.), *Optical orientation* (Elsevier, Amsterdam, 1984).

[25] J. M. Kikkawa and D. D. Awschalom, *Resonant Spin Amplification in n-Type GaAs*, Phys. Rev. Lett. **80**, 4313 (1998).

[26] V. A. Karasyuk, D. G. S. Beckett, M. K. Nissen, A. Villemaire, T. W. Steiner, and M. L. W. Thewalt, *Fourier-transform magnetophotoluminescence spectroscopy of donor-bound excitons in GaAs*, Phys. Rev. B **49**, 16381 (1994).

[27] K.-M. Fu, C. Santori, C. Stanley, M. Holland, and Y. Yamamoto, *Coherent Population Trapping of Electron Spins in a High-Purity n-Type GaAs Semiconductor*, Phys. Rev. Lett. **95**, 187405 (2005).

[28] T. Wang, R. Rajapakse, and S. F. Yelin, *Electromagnetically induced transparency and slow light with semiconductor bound excitons*, Optics Comm. **272**, 154 (2007).

[29] C. W. Chou *et al.*, *Measurement-induced entanglement for excitation stored in remote atomic ensembles*, Nature **438**, 828 (2005).

[30] D. N. Matsukevich *et al.*, *Entanglement of Remote Atomic Qubits*, Phys. Rev. Lett. **96**, 030405 (2006).

[31] L. V. Hau *et al.*, *Light speed reduction to 17 metres per second in an ultracold atomic gas*, Nature **397**, 594 (1999).

[32] D. F. Phillips *et al.*, *Storage of Light in Atomic Vapor*, Phys. Rev. Lett. **86**, 783 (2001).

[33] C. H. van der Wal and M. Sladkov, *Towards quantum optics and entanglement with electron spin ensembles in semiconductors*, Solid State Sci. **11**, 935 (2009).

[34] A. Abragam, *The Principles of Nuclear Magnetism* (Oxford University Press, 1961).

[35] B. Urbaszek *et al.*, *Nuclear spin physics in quantum dots: An optical investigation*, Rev. Mod. Phys. **85**, 79 (2013).

[36] S. M. Clark, K.-M. C. Fu, Q. Zhang, T. D. Ladd, C. Stanley, and Y. Yamamoto, *Ultrafast optical spin echo for electron spins in semiconductors*, Phys. Rev. Lett. **102**, 247601 (2009).

[37] X. Xu *et al.*, *Optically controlled locking of the nuclear field via coherent dark-state spectroscopy*, Nature **459**, 1105 (2009).

[38] A. R. Onur, *Optical control of mesoscopic spin ensembles in gallium arsenide* (PhD thesis, University of Groningen, 2015).

[39] J. P. de Jong, *Optically addressing semiconductor electron-spin ensembles with tunable nuclear-spin environments* (PhD thesis, University of Groningen, 2016).

[40] D. Brunner *et al.*, *A coherent single-hole spin in a semiconductor*, Science **325**, 70 (2009).

[41] R. J. Warburton, *Single spins in self-assembled quantum dots*, Nature Materials **12**, 483 (2013).

[42] C. Latta *et al.*, *Confluence of resonant laser excitation and bidirectional quantum-dot nuclear-spin polarization*, Nature Physics **5**, 758 (2009).

[43] M. T. Rakher *et al.*, *Externally Mode-Matched Cavity Quantum Electrodynamics with Charge-Tunable Quantum Dots*, Phys. Rev. Lett. **102**, 097403 (2009).

[44] R. B. Patel *et al.*, *Two-photon interference of the emission from electrically tunable remote quantum dots*, Nature Photonics **4**, 632 (2010).

[45] J. Gudat *et al.*, *Permanent tuning of quantum dot transitions to degenerate microcavity resonances*, Appl. Phys. Lett. **98**, 121111 (2011).

[46] J. H. Prechtel *et al.*, *Frequency-stabilized source of single photons from a solid-state qubit*, Phys. Rev. X **3**, 041006 (2013).

[47] C. Santori *et al.*, *Indistinguishable photons from a single-photon device*, Nature **419**, 594 (2002).

[48] S. Strauf *et al.*, *High-frequency single-photon source with polarization control*, Nature Photonics **1**, 704 (2007).

[49] J. Berezovsky *et al.*, *Picosecond coherent optical manipulation of a single electron spin in a quantum dot*, Science **320**, 349 (2008).

[50] D. Press, T. D. Ladd, B. Zhang, and Y. Yamamoto, *Complete quantum control of a single quantum dot spin using ultrafast optical pulses*, Nature **456**, 218 (2008).

[51] E. B. Flagg *et al.*, *Interference of Single Photons from Two Separate Semiconductor Quantum Dots*, Phys. Rev. Lett. **104**, 137401 (2010).

[52] A. N. Vamivakas *et al.*, *Observation of spin-dependent quantum jumps via quantum dot resonance fluorescence*, Nature **467**, 297 (2010).

[53] K. De Greve *et al.*, *Quantum-dot spin-photon entanglement via frequency downconversion to telecom wavelength*, Nature **491**, 421 (2012).

[54] Y.-M. He *et al.*, *On-demand semiconductor single-photon source with near-unity indistinguishability*, Nature Nano. **8**, 213 (2013).

[55] A. V. Kuhlmann *et al.*, *Transform-limited single photons from a single quantum dot*, Nature Comm. **6**, 8204 (2015).

[56] A. Delteil *et al.*, *Generation of heralded entanglement between distant hole spins*, Nature Physics **12**, 218 (2016).

[57] C. Santori *et al.*, *Coherent Population Trapping of Single Spins in Diamond under Optical Excitation*, Phys. Rev. Lett. **97**, 247401 (2006).

[58] V. V. Dobrovitski *et al.*, *Quantum Control over Single Spins in Diamond*, Annual Review of Condensed Matter Physics **4**, 23 (2013).

[59] B. Hensen *et al.*, *Loophole-free Bell inequality violation using electron spins separated by 1.3 kilometres*, Nature **526**, 682 (2015).

[60] J. R. Weber *et al.*, *Quantum Computing with Defects*, Proc. Nat. Acad. Sci. **107**, 8513 (2010).

[61] W. F. Koehl *et al.*, *Room temperature coherent control of defect spin qubits in silicon carbide*, Nature **479**, 84 (2011).

[62] O. V. Zwier, *Two-laser spectroscopy and coherent manipulation of color-center spin ensembles in silicon carbide* (PhD thesis, University of Groningen, 2016).

[63] J. J. Longdell, *et al.*, *Stopped light with storage times greater than one second using electromagnetically induced transparency in a solid*, Phys. Rev. Lett. **95**, 063601 (2005).

[64] M. P. Hedges *et al.*, *Efficient quantum memory for light*, Nature **465**, 1052 (2010).

[65] Georg Heinze, Christian Hubrich, and Thomas Halfmann, *Stopped Light and Image Storage by Electromagnetically Induced Transparency up to the Regime of One Minute*, Phys. Rev. Lett. **111**, 033601 (2013).

[66] D. Ding *et al.*, *Multidimensional Purcell effect in an ytterbium-doped ring resonator*, Nature Photonics **10**, 385 (2016).

[67] K. Saeedi *et al.*, *Room-Temperature Quantum Bit Storage Exceeding 39 Minutes Using Ionized Donors in Silicon-28*, Science **342**, 830 (2013).

[68] T. D. Ladd *et al.*, *Fluorine-doped ZnSe for applications in quantum information processing*, Phys. Stat. Sol. B **246**, 1543 (2010).

[69] K.-M. C. Fu *et al.*, *Millisecond spin-flip times of donor-bound electrons in GaAs*, Phys. Rev. B **74**, 121304 (2006).

[70] K.-M. C. Fu *et al.*, *Ultrafast control of donor-bound electron spins with single detuned optical pulses*, Nature Physics **4**, 780 (2008).

[71] F. Berski *et al.*, *Interplay of Electron and Nuclear Spin Noise in n-Type GaAs*, Phys. Rev. Lett. **115**, 176601 (2015).

# Chapter 2

# Electromagnetically induced transparency with an ensemble of donor-bound electron spins in a semiconductor

**Abstract**

We present measurements of electromagnetically induced transparency with an ensemble of donor-bound electrons in low-doped $n$-GaAs. We used optical transitions from the Zeeman-split electron spin states to a bound trion state in samples with optical densities of 0.3 and 1.0. The electron spin dephasing time $T_2^* \approx 2$ ns was limited by hyperfine coupling to fluctuating nuclear spins. We also observe signatures of dynamical nuclear polarization, but find these effects to be much weaker than in experiments that use electron spin resonance and related experiments with quantum dots.

This chapter is based on Refs. 1 and 2 on p. 127.

## 2.1 Introduction

A localized electronic spin in a semiconductor is a promising candidate for implementing quantum information tasks in solid state. Optical manipulation of single-electron and single-hole systems has been realized with quantum dots [1, 2, 3, 5, 4] and by using donor atoms that are not ionized at low temperature ($D^0$ systems) [6, 7, 8]. These results illustrate the potential of quantum-optical control schemes that come within reach when adapting techniques from the field of atomic physics. An advantage of the $D^0$ systems over dots is that these can be operated as an ensemble with very little inhomogeneity for the optical transition energies. Such ensembles at high optical density are key for robust quantum-optical control schemes that have been designed for preparing nonlocal entanglement between spins, quantum communication, and applying strong optical nonlinearities [9, 10]. A critical step toward implementing these schemes is the realization of electromagnetically induced transparency (EIT). We present here measurements of EIT with an ensemble of donor-bound electron spins in low-doped $n$-GaAs, in samples with optical densities of 0.3 and 1.0 [11]. We build on an earlier indirect observation of coherent population trapping with this system [6]. Extending this to a direct realization of EIT with an optically dense medium is essential for getting access to strong field-matter interactions without using optical cavities, and for the application and study of transmitted signal fields [9, 10].

We implemented EIT in its most typical form where a spin-up and a spin-down state ($|\uparrow\rangle$ and $|\downarrow\rangle$ of the electron in the $D^0$ system) have an optical transition to the same excited state $|e\rangle$ (Fig. 2.1(e)). We Zeeman-split the states $|\uparrow\rangle$ and $|\downarrow\rangle$ with an applied magnetic field. For the state $|e\rangle$ we used the lowest energy level (that is strongly optically active) of a donor-bound trion system. This excited system ($D^0X$) has two electrons in a singlet state and a spin-down hole with $m_h = -\frac{1}{2}$ [8] localized at the donor site. EIT is then the phenomenon that absorbtion by one of the optical transitions is suppressed because destructive quantum interference with the other transition prohibits populating the state $|e\rangle$. The $D^0$ systems are then trapped in a dark state that is in the ideal case a coherent superposition of the states $|\uparrow\rangle$ and $|\downarrow\rangle$ only [6, 11]. This state is proportional to $\Omega_c\,|\uparrow\rangle - \Omega_p\,|\downarrow\rangle$, with $\Omega_c$ and $\Omega_p$ the Rabi frequencies of the control and probe field that drive the two transitions [10].

We present results of implementing EIT in GaAs, and we studied the interactions between the solid-state environment and driving EIT. In particular, the $D^0$ systems have a single electron in a hydrogen-like $1s$ wave function with a

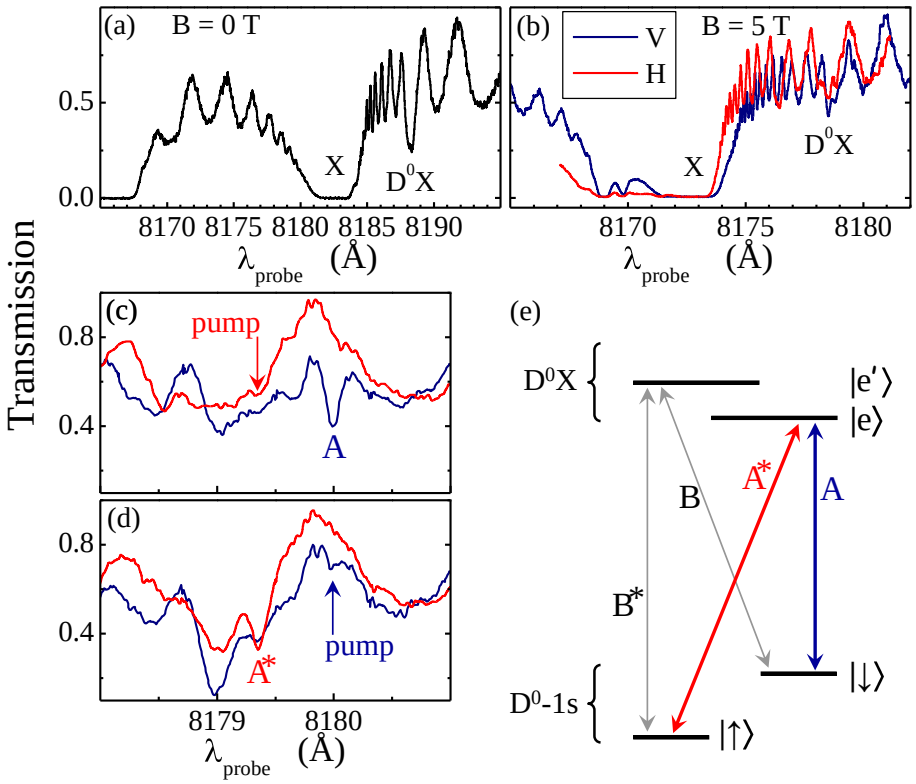


**Figure 2.1:** **(a)** Transmission spectroscopy at $B = 0$ T. **(b)** Transmission at $B = 5.0$ T for H and V polarization. **(c)** Pump-assisted spectroscopy with H-polarized pumping at the $A^*$ transition shows enhanced absorption for the $A$ transition for the scan with a V-polarized probe (blue trace), but not with an H-polarized probe (red trace). **(d)** Complementary to (c), V-polarized pumping at $A$ shows enhanced absorption for the $A^*$ transition with an H-polarized probe. **(e)** Energy levels and optical transitions of the $D^0$-$D^0X$ system.

Bohr radius of ∼10 nm, and each electron spin has hyperfine coupling to $\sim 10^5$ fluctuating nuclear spins. We studied how this limits the electron spin dephasing time and how driving EIT can result in dynamical nuclear polarization (DNP). In addition, we find that it is crucial to suppress heating effects from the nearby free exciton resonance, and demonstrate that with direct heat sinking of GaAs layers EIT can be driven with $\Omega_c/2\pi$ up to 2 GHz, while keeping the spin dephasing time $T_2^* \approx 2$ ns near the level that results from the nuclear spin fluctuations.

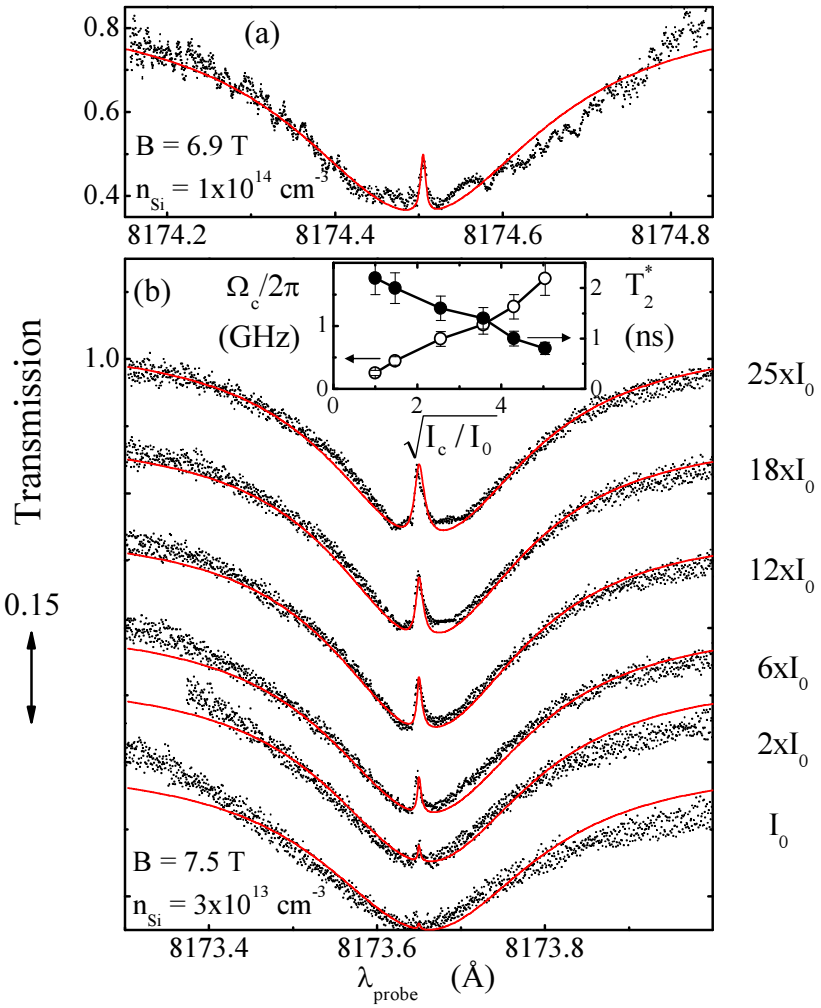


**Figure 2.2:** **(a)** EIT spectrum from sample with Si doping at $1 \times 10^{14}$ cm$^{-3}$. Dots - experiment. Line - numerical fit. **(b)** EIT spectra from sample with Si doping at $3 \times 10^{13}$ cm$^{-3}$, for probe-field intensity 0.04 Wcm$^{-2}$ and a range of control-field intensities $I_c$ with $I_0 = 0.4$ Wcm$^{-2}$. The inset shows the fitting results for Rabi frequency $\Omega_c$ and spin dephasing time $T_2^*$.

## 2.2 Materials and methods

We used epitaxially grown GaAs films of 10 $\mu$m thickness with Si doping at $n_{\rm Si} = 3 \times 10^{13}$ and $1 \times 10^{14}$ cm$^{-3}$. At these concentrations the wave functions of neighboring donor sites do not overlap, which yields an ensemble of non-interacting $D^0$ systems. The films were transferred to a wedged sapphire substrate with an epitaxial lift-off process [12], and fixed there by Van der Waals

forces which assures high heat sinking. The sapphire substrate was mounted on the copper cold finger of a bath cryostat (4.2 K) in the center of a superconducting magnet with fields $B$ up to 8 T in the plane of the sample ($z$-direction). Laser light was brought to the films at normal incidence (Voigt geometry) via a polarization-maintaining single-mode fiber. The two linear polarizations supported by the fiber are set parallel (V polarization) and orthogonal (H polarization) to the applied magnetic field. The V polarization can drive $\pi$ transitions (no change of $z$-angular momentum) and the H polarization can drive transitions with a change in $z$-angular momentum of $\pm\hbar$.

Two CW Ti:sapphire lasers (Coherent MBR-110, linewidth below 1 MHz) provided tunable probe and control fields. Focussing in the sample volume was achieved with a piezo-motor controlled confocal microscope. During transmission experiments we defocussed the microscope to a spot of $\sim$16 $\mu$m diameter to avoid interference effects from the cavity that is formed between the sample surface and the facet of the fiber. The probe field was amplitude modulated at 6 kHz and we used lock-in techniques for detecting light that is transmitted trough the sample with a photodiode directly behind the sample. The signal due to unmodulated control field is rejected by AC coupling of the measurement electronics.

## 2.3 Transmission spectroscopy

We first report transmission experiments that identify the spectral position of the $D^0X$ related resonances. Only the probe laser was used. Figure 2.1(a) shows a spectrum taken at $B = 0$ T (identical result for H and V polarization), and Fig. 2.1(b) shows a result for $B = 5.0$ T with a separate trace for H and V polarization. The strong absorbtion labeled $X$ is due to excitation of free excitons. Resonant absorption by donor-bound excitons ($D^0X$) occurs at 8187.5 Å for $B = 0$ T and at 8179.5 Å for $B = 5.0$ T. The shift of the resonances with magnetic field is the diamagnetic shift. The spacing of 5 Å between the $X$ and $D^0X$ resonances is in good agreement with previously reported binding energies [13, 14]. The oscillating background superimposed on the resonances is due to a Fabry-Pérot effect in the GaAs film, and its chirped wavelength dependence around $X$ is due to the wavelength dependent refractive index that is associated with the strong free exciton absorption.

For identifying the $A$ and $A^*$ transitions of Fig. 2.1(e) within the fine structure of $D^0X$ spectra at high fields we performed scanning-probe laser spectroscopy while the control laser is applied for optical pumping of a particular $D^0X$ tran-

sition (this also eliminates bleaching by the probe). Figure 2.1(c) shows spectra obtained with pumping at $A^*$ (8179.3 Å) with H polarization. This leads to enhanced absorbtion at the $A$ resonance (8180.0 Å) for the probe scan with V polarization. The complementary experiment with pumping V-polarized light into this $A$ transition leads to enhanced absorption of H-polarized light at transition $A^*$ (Fig. 2.1(d)). We could also perform such cross-pumping experiments using the $B$ and $B^*$ transitions to the level $|e'\rangle$ (the first excited state of the series of energy levels of the $D^0X$ complex, see Fig. 2.1(e)). We thus confirmed that the pair of transitions labeled as $A$ and $A^*$ address a so-called closed three-level $\Lambda$-system, and that this is the pair with lowest energies for the (significantly strong) $D^0X$ resonances. This interpretation is also consistent with the polarization dependence of these transitions [14, 6]. In the field range 5 to 8 T, the $A$ and $A^*$ transitions are spectrally well separated from the transitions $B$, $B^*$, and transitions to higher excited states of the $D^0X$ complex. The observed $D^0$ Zeeman splitting corresponds to an electron $g$ factor $|g| = 0.42$, and also agrees with previous reports [14, 6].

## 2.4 Demonstration of EIT

We now turn to the observation of EIT (Fig. 2.2). For these results we fixed the control laser central on the $A$ transition (V polarization), while the probe laser is scanned across the $A^*$ transition (H polarization). When the control and probe field meet the condition for two-photon Raman resonance (the difference in photon energy exactly matches the $D^0$ spin splitting), a narrow peak with enhanced transmission appears inside the broader $A^*$ absorption dip, which is the fingerprint of EIT. In Fig. 2.2(a) this occurs inside an $A^*$ absorption with optical density 1.0, while for the sample with $n_{\mathrm{Si}} = 3 \times 10^{13}$ cm$^{-3}$ this is 0.3 (Fig. 2.2(b)). We further focus on this latter sample since higher resolution of the EIT spectra makes it more suited for our further studies.

The lines in Fig. 2.2 and 2.3 are results of fitting EIT spectra with the established theory [10]. This involves calculating the steady-state solution of a density-matrix equation for the three-level system, and accounts for coherent driving by the lasers and relaxation and dephasing rates between the levels. The free parameters are the inhomogeneous broadening $\gamma_{A^*}$ (typically 6 GHz) for the optical transition $A^*$, the spin dephasing time $T_2^*$ and the control-field induced Rabi frequency $\Omega_c$ (and $\Omega_p << \Omega_c$). The rest of the parameters are the same as in Ref. [6], and we found $\Omega_c$ always consistent with an independent estimate

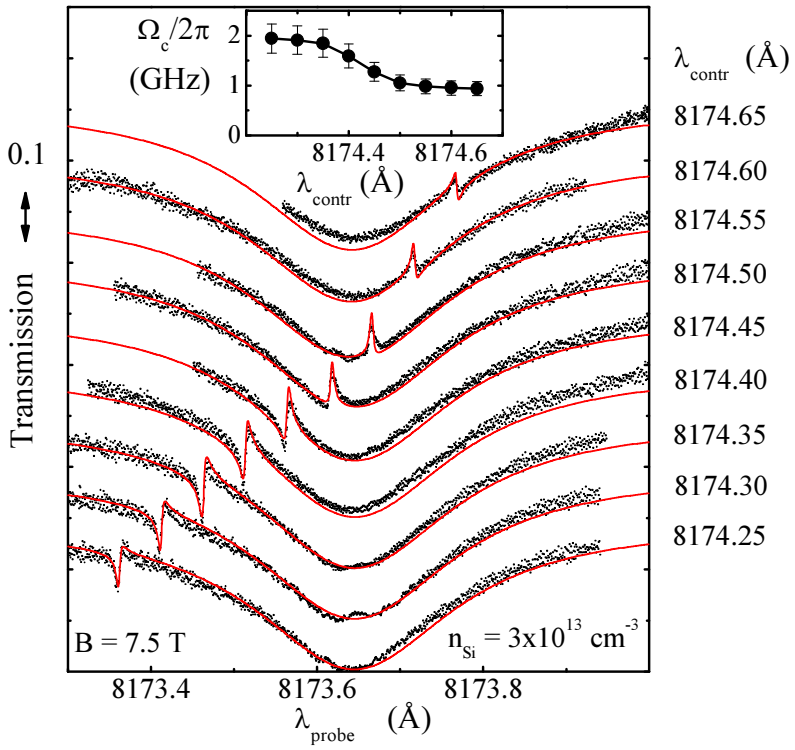


**Figure 2.3:** Dependence of EIT spectra on control-field detuning. The position of the EIT peak follows precisely the control-field detuning from transition $A$. Dots - experiment with control (probe) intensity 6 (0.04) Wcm$^{-2}$. Lines - fits with $T_2^* = 2$ ns and $\Omega_c$ as presented in the inset.

from the optical intensity and electric dipole moment. We obtain good fits and the main features in our results are consistent with EIT, as we discuss next.

Figure 2.2(b) shows EIT spectra taken at different intensities $I_c$ of the control field, where a stronger control field yields a higher and broader EIT peak. As expected for EIT, we observe that $\Omega_c$ from fits scales linearly with $\sqrt{I_c}$ (Fig. 2.2(b), inset). The $\Omega_c$ values reach $2\pi \cdot 2$ GHz, and we could only obtain clear EIT spectra with such high $\Omega_c$ in samples with complete adhesion onto the sapphire substrate. Our results from samples with incomplete adhesion (and work with epi-layers that are not removed from the original GaAs substrate [6, 7, 8]) suffer from heating, which is observed as a broadening of the free exciton line into the region of the $D^0X$ resonances. The values of $T_2^*$ that we find in our experiments are discussed below.

Figure 2.3 shows how the EIT peak position depends on detuning of the control field from the $A$ transition. As expected, the EIT peak follows the detuning

of the control field. However, the EIT peak in the blue-detuned traces is clearly more prominent than in the red-detuned cases. We attribute this to a change in the effective Rabi frequency $\Omega_c$ that results from the weak Fabry-Pérot interference within the GaAs film, and we can indeed fit the results with fixed $T_2^* = 2$ ns and varying $\Omega_c$ (Fig. 2.3, inset). We can exclude that the difference in the quality of EIT spectra is coming from optical coupling to a level outside our $\Lambda$-system, since all other transitions are well separated spectrally and in polarization dependence (*e.g.* the $B$ and $B^*$ transitions, see Fig. 2.1(e)).

## 2.5 Spin coherence time $T_2^*$ and signatures of Dynamic Nuclear Polarization

An important topic that needs to be addressed next with this realization of EIT concerns the influence of the hyperfine coupling between each electron spin and $\sim 10^5$ nuclear spins. A polarization of the nuclear spins acts on the electron spin as an effective magnetic field $B_{nuc}$. The average polarization affects the Zeeman splitting, and this can be directly observed in EIT spectra as a red (blue) shift of the EIT peak for a reduced (enhanced) Zeeman splitting. The nuclear spin fluctuations around the average dominate via this mechanism the inhomogeneous electron spin coherence time $T_2^*$. This is a key parameter for the shape of the EIT peak (longer $T_2^*$ gives a sharper peak), and the magnitude of these fluctuations can therefore be derived from the EIT spectra as well. At our fields and temperature nuclear spins are in equilibrium close to full random orientation. The expected value for $T_2^*$ for this case is $\sim$2 ns [6, 15], and is in agreement with the values that we observe.

The hyperfine coupling can also result in dynamical nuclear polarization (DNP), which is the transfer of angular momentum from the electron to the nuclear spins when the electron spin is driven out of equilibrium. Earlier experiments on our type of $D^0$ system with microwave-driven electron spin resonance (ESR) [15] and optical experiments on quantum dots showed strong DNP [3, 4]. In both cases the effects were so strong that it gave an unstable resonance condition for tuning at ESR and EIT (the systems trigger a DNP cycle that drives them out of resonance). DNP can also result in a suppression of the nuclear spin fluctuations, which yields a longer $T_2^*$ [2, 3, 4, 16]. Our experiment, however, only shows weak DNP. We never observed a significant change in the Zeeman energy (as derived from subtracting the probe and control photon energies at the

EIT peak) from the EIT driving itself. We only observed in several data sets a moderate EIT peak narrowing over the course of a few hours of data taking (at fixed settings of the EIT parameters). In order to confirm the role of nuclear spins we carried out various attempts to induce stronger DNP effects.

An example of the strongest DNP effects that we could induce is presented in Fig. 2.4. Here we first applied strong driving of the $A^*$ transition for 30 min with an intensity equivalent to a Rabi frequency of $2\pi \cdot 10$ GHz. This should pump the system fully into $|\downarrow\rangle$. After pumping we take fast 'snapshots' of the EIT peak (50 sec $A^*$ scans, $\Omega_p/2\pi = 25$ MHz and control at $A$ with $\Omega_c/2\pi = 1$ GHz). Between scans we kept the system in the dark for 10 min. Figure 2.4 shows 6 subsequent snapshots. Right after pumping we observe a blue-shifted and sharpened EIT peak ($T_2^* = 3$ ns). This enhancement of $T_2^*$ probably results from suppressed nuclear spin fluctuations, which generally occurs when the polarization gets squeezed between a polarizing and depolarizing mechanism with rates that are both enhanced due to the DNP [3, 4, 16]. The peak shift agrees in sign with Ref. [15] but corresponds to $B_{nuc} = 21$ mT only (the ESR studies [15] and the work on dots easily induced 200 mT - 1 T). Subsequent spectra show a clear broadening of the EIT peak, which also shifts back to the red. After about 1 hour, $T_2^*$ (Fig. 2.4, inset) and the peak position stabilize at the values that were observed before pumping. This agrees with the relaxation time for DNP with $D^0$ systems [15]. Upon exploring how DNP occurs for various EIT and pump conditions we found the effects to be too weak for systematic control and drawing further conclusions, and full understanding goes beyond the study that is reported in this chapter. Follow-up experiments on this are presented in Chapter 4, and these confirm that the DNP effects are not easy to reproduce, due to being very sensitive to the exact settings of the control lasers. These results, and also work with quantum dots [3, 4], confirmed that the mechanisms that dominate the DNP rate are often complex and need to account for driving-field assisted processes. We can nevertheless conclude that our spin dephasing time is indeed limited by coupling to nuclear spins.

## 2.6 Conclusions

In conclusion, we presented direct evidence that a $D^0$ ensemble in GaAs can be operated as a medium for EIT. The electron spin dephasing time limits the quality of the EIT, and is in the range $T_2^* \approx 2$ ns that results from hyperfine coupling to fluctuating nuclear spins. The EIT spectra form a sensitive probe for detecting

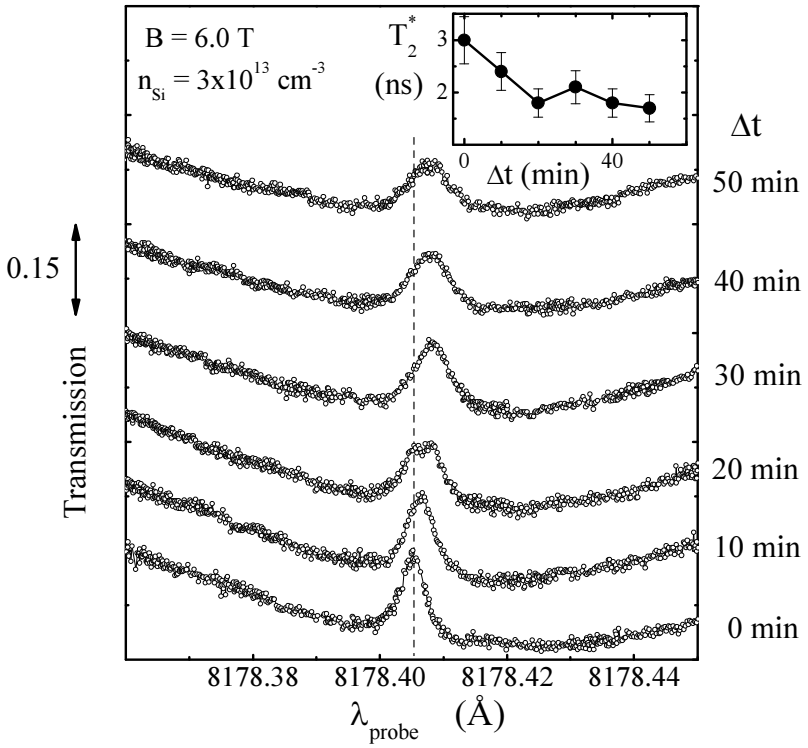


**Figure 2.4:** Evolution of the EIT peak after 30 min pumping of the $A^*$ transition. Fast EIT 'snapshots' were taken at 10 min intervals during which the sample was kept in the dark. The dashed line is a guide for showing the shift in peak position. The inset presents fitting results that show the change in $T_2^*$.

how DNP changes the fluctuations and the average of nuclear spin polarization. However, direct optical driving of $D^0$ transitions yields much weaker DNP effects than in electron spin resonance experiments with $D^0$ systems and related EIT experiments on quantum dots, and a complete physical picture of DNP effects in our system is at this stage not available. Still, initial signatures of controlled DNP effects show that the electron spin-dephasing time can be prolonged. Our experimental approach is suited for exploring this further in conjunction with experiments that aim to implement various applications of EIT [9, 10]. Initial steps for such follow-up experiments are presented in Chapter 4.

# Acknowledgements

We thank B. Wolfs, J. Sloot and S. Lloyd for contributions, and the Dutch NWO and FOM, and the German programs DFG-SPP 1285, BMBF nanoQUIT and

Research school of Ruhr-Universität Bochum for support.

# References

[1] D. Press, T. D. Ladd, B. Zhang, and Y. Yamamoto, *Complete quantum control of a single quantum dot spin using ultrafast optical pulses*, Nature **456**, 218 (2008).

[2] A. Greilich, Sophia E. Economou, S. Spatzek, D. R. Yakovlev, D. Reuter, A. D. Wieck, T. L. Reinecke and M. Bayer, *Ultrafast optical rotations of electron spins in quantum dots*, Nature Physics **5**, 262 (2009).

[3] X. Xu, W. Yao, B. Sun, D. G. Steel, A. S. Bracker, D. Gammon, and L. J. Sham *Optically Controlled Locking of the Nuclear Field via Dark State Spectroscopy*, Nature **459**, 1105 (2009).

[4] C. Latta, A. Högele, Y. Zhao, A. N. Vamivakas, P. Maletinsky, M. Kroner, J. Dreiser, I. Carusotto, A. Badolato, D. Schuh, W. Wegscheider, M. Atature and A. Imamoglu, *Confluence of resonant laser excitation and bidirectional quantum-dot nuclear-spin polarization*, Nature Physics **5**, 758 (2009).

[5] D. Brunner, B.D. Gerardot, P. A.Dalgarno, G. Wüst, K. Karrai, N. G. Stoltz, P. M. Petroff, and R. J. Warburton, *A coherent single-hole spin in a semiconductor*, Science **325**, 70 (2009).

[6] K.-M. Fu, C. Santori, C. Stanley, M. Holland, and Y. Yamamoto, *Coherent Population Trapping of Electron Spins in a High-Purity n-Type GaAs Semiconductor*, Phys. Rev. Lett. **95**, 187405 (2005).

[7] K.-M. C. Fu, S. M. Clark, C. Santori, C. R. Stanley, M. C. Holland, and Y. Yamamoto, *Ultrafast control of donor-bound electron spins with single detuned optical pulses*, Nature Physics **4**, 780 (2008).

[8] S.M. Clark, K-M. C. Fu, Q. Zhang, T.D. Ladd, C. Stanley, and Y.Yamamoto, *Ultrafast optical spin echo for electron spins in semiconductors*, Phys. Rev. Lett. **102**, 247601 (2009).

[9] L. M. Duan, M. D. Lukin, J. I. Cirac, and P. Zoller, *Long-distance quantum communication with atomic ensembles and linear optics*, Nature **414**, 413 (2001).

[10] M. Fleischhauer, A. Imamoglu, and J.Marangos, *Electromagnetically induced transparency: Optics in coherent media*, Rev. Mod. Phys. **77**, 633 (2005).

[11] T. Wang, R. Rajapakse, and S. F. Yelin, *Electromagnetically induced transparency and slow light with n-doped GaAs*, Optics Communications **272**, 154, (2007).

[12] E. Yablonovitch, T. Gmitter, J. Harbison, and R. Bhat, *Extreme selectivity in the lift-off of epitaxial GaAs films*, Appl. Phys. Lett. **51**, 2222 (1987).

[13] Bogardus and H. Bebb, *Bound-Exciton, Free-Exciton, Band-Acceptor, Donor-Acceptor, and Auger Recombination in GaAs*, Phys. Rev. **176**, 993 (1968).

[14] V. A. Karasyuk, D. G. S. Beckett, M. K. Nissen, A. Villemaire, T. W. Steiner, and M. L.W. Thewalt, *Fourier-transform magnetophotoluminescence spectroscopy of donor-bound excitons in GaAs*, Phys. Rev. B **49**, 16381 (1994).

[15] T. A. Kennedy, J. Whitaker, A. Shabaev, A. S. Bracker, and D. Gammon, *Detection of magnetic resonance of donor-bound electrons in GaAs by Kerr rotation*, Phys. Rev. B **74**, 161201 (2006).

[16] I. Vink *et al.*, *Locking electron spins into magnetic resonance by electron-nuclear feedback* Nature Physics **5**, 764 (2009).

# Chapter 3

# High-resolution magneto-optical transmission spectroscopy on the donor-bound-exciton complex in GaAs

**Abstract**

We present high-resolution magneto-optical spectroscopy studies of the donor-bound exciton ($D^0X$) states in $n$-GaAs. In our approach we resonantly excite transitions from one of the two spin states of localized donor electrons ($D^0$ systems) to specific levels of the $D^0X$ complex, and derive spectroscopic signals from laser fields transmitted through the material. Our goal was to characterize the $D^0X$ levels in terms of their quantum numbers, level splittings, and the purity of polarization selection rules of the $D^0$-$D^0X$ transitions. While we can partly link our analysis to earlier experimental studies of this system (mainly photoluminescence results, PL), our conclusion is that we cannot fully identify the correspondence between these PL results and our transmission results. We also conclude that the existing theoretical models for the $D^0X$ system can only partly describe our observations.

This chapter is based on Ref. 5 on p. 127.

## 3.1 Introduction

As introduced in Chapter 1, the research presented in this thesis aims to investigate how quantum-optical control techniques can be implemented and optimized with a solid-state material system, for the long-term goal of realizing quantum-information processing. Optimally using the spin coherence of the $D^0$ system via the $D^0$-$D^0X$ optical transitions requires knowledge of the $D^0X$ levels, including their behavior in an applied magnetic field. In particular, an approach based on Electromagnetically Induced Transparency (EIT, see Chapters 1, 2) works optimal with strong optical transitions that obey clear polarization selection rules, to a $D^0X$ level that is energetically well separated from other levels. Knowledge of the selection rules for the various $D^0X$ levels, and how they shift when applying a magnetic field in a particular direction, is then indispensable. While purely phenomenological data on this is already of great value, the goal of the research presented in this chapter is to also identify the quantum numbers of the observed $D^0X$ states, and to confirm the correspondence between our magneto-optical $D^0X$ observations and theoretical modeling. Given that extensive earlier work by others in this direction had only limited success (see below), our expectations for success should be moderate. Our motivation to nevertheless study again it is twofold. Most earlier studies used signals from photoluminescence, while our approach may have an advantage from direct resonant excitation of transitions, and studying signals from this in transmission. Further, we need to establish to what extent the predicted behavior of the models really occurs for our approach.

Earlier work by our team on the GaAs $D^0$ system gave specific additional motivations for such a spectroscopic study. For one, we found that in applied magnetic fields between 7 T and 8 T, experimentally finding the $D^0$-$D^0X$ transitions and realizing EIT was typically much harder (and for several samples impossible) as compared to such work below 7 T or above 8 T. Understanding of this observation is till now fully lacking. Further, for Dynamic Nuclear Polarization (DNP, see also Chapters 1, 2, 4), direct electron-nuclear spin flip-flops are energetically forbidden when their Zeeman splittings differ significantly. More complex mechanisms then dominate the process, possibly mediated by optical transitions [1]. Understanding what mechanisms could here be at play clearly needs insight into the spin and orbital-momentum quantum numbers of the involved $D^0X$ levels, as well as the associated selection rules.

The $D^0X$ system in GaAs and similar semiconductors has already been studied for more than 50 years (further reviewed in the next section, see also Chap-

ter 1). Still, this line of research (in particular the theoretical description) left several open questions, since the $D^0X$ system is rather complex. The relevant energy splittings are rather small, such that it is at the edge of what can be reliably addressed with numerical approaches such as Density Functional Theory. An analytical approach is also challenging. The $D^0X$ system is an atom-like system in a solid-state environment, where three charge carriers (two electrons and a hole) are in orbit around the donor (Si) core ion (which has in this description a charge of $+|e|$). Since it concerns a shallow donor, the state has to obey the symmetries of the atomic lattice and the ∼10-nm-radius (in zero field spherical) envelope wave function, while this latter symmetry is distorted towards cylindrical cyclotron states when a magnetic field is applied. In addition, the three charge carriers have interactions at an energy scale similar to that of the confinement potentials, and spin-orbit couplings are significant. A theoretical model that captures all aspects of this system's behavior has not been presented yet, and will be very complex. Approximations for this, and theoretical concepts underlying the complete behavior, will be introduced in Section 3.2 and throughout the main text.

A further outline of this chapter is as follows. Section 3.3 presents the approach and results for single-laser spectroscopic studies, and Section 3.4 presents this for two-laser spectroscopic studies. The results are collected and analyzed in Section 3.5, and Section 3.6 presents the conclusions. Section 3.7 is an appendix where we present an overview of various notations used in the literature, since the use of these has not been consistent, and we ran into several (apparent) errors or points of confusion. Two more appendices present details of our analysis.

### 3.1.1 Materials and experimental methods

We will only provide here a brief summary of the $n$-GaAs material and experimental methods used for the work presented in this chapter, since most aspects are identical to those presented in Chapter 2 and Chapter 5. Specific details of how single- and two-laser spectroscopy were carried out for the results presented in this chapter are discussed in the sections where these results are presented.

All spectroscopy results were obtained from laser transmission studies on a 10-$\mu$m thick GaAs layer that contained silicon atoms as donor impurities at a concentration of $\sim 3 \times 10^{13}$ cm$^{-3}$. The material was MBE grown along the [001] crystal direction (orthogonal to the layer). All results were obtained at 4.2 K. The magnetic field was applied parallel to the [110] crystal direction, with magnitudes

from $B = 0$ T to $B = 9.4$ T. The propagation of the laser fields was along the growth axis, and the fields reached the sample with linear polarization that was either parallel (denoted as V[ertical]) or orthogonal (denoted as H[orizontal]) to the direction of the magnetic field. This chapter only presents results where shifts of the $D^0X$ levels due to strain in the material are not significant (conclusion based on comparison with results in the literature [2] and related results from our team [3]).

## 3.2 Properties and models of the $D^0X$ system in GaAs

Building on the basic descriptions of the $D^0$ and $D^0X$ systems in Section 1.3, we will present here further properties and models of the $D^0X$ system in GaAs. This system has already been studied for decades (with many corrections on the way), and state-of-the-art results and an authoritative review are provided by Ref. [4], and more recent extensions of this work are reported in Ref. [5]. As a basis for using these reports, we also used several earlier publications [6–23].

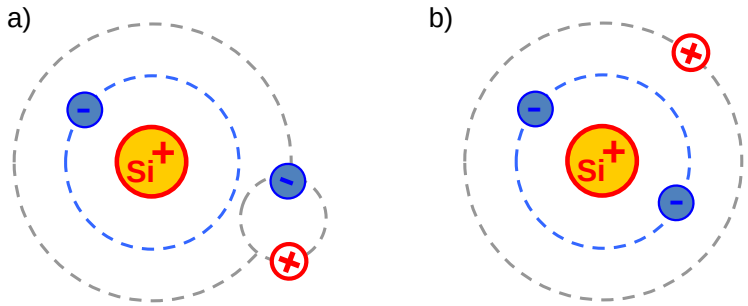


**Figure 3.1:** Orbiting-particle illustrations of the $D^0X$ system with two electrons and one hole bound by the Si-donor core ion. Theoretical modeling assumed as starting points **(a)** that an exciton (bound electron-hole pair) is in orbit around a non-ionized Si donor, or **(b)** that the Si core ion has two electrons in a singlet state tightly bound to it, and that this system has –in turn– a hole in orbit around it. Further refinements of the modeling considered superpositions of the two cases.

The physical picture that emerges is that the $D^0X$ has two electrons and one hole localized in a bound state around the core ion of the Si donor. For the lowest energy levels, the two electrons are always in a singlet state (the triplet state has much higher energies, never observed as a stable state). In a magnetic

field, the $D^0X$ system still shows a set of at least 6 different energy eigenstates (discrete $D^0X$ levels) that are easily observed. These levels result from two different degrees of freedom.

First, there are the Zeeman sub-levels of the hole. The hole states at the top of the valence band have a wave function (at the scale of the lattice) that has a total angular momentum characterized by quantum number $j = \frac{3}{2}$, and quantum numbers $m_j = \pm\frac{1}{2}, \pm\frac{3}{2}$ for the component along the field. These four eigenstates are often described as the four spin (or quasi-spin) levels of the hole, even though they are in fact eigenstates of the spin-orbit coupled electronic state.

Second, there are at low energies different states for the angular momentum of the envelope wave function of the orbiting complex with two electrons and one hole (which are for the bound state strongly interacting particles). This envelope wave function has azimuthal quantum number $L$, and magnetic quantum number $M_L$. The lowest optically active states have $L = 0$ (and thereby $M_L = 0$), or $L = 1$ and $M_L = 0$. The literature never discusses the states with $L = 1$ and $M_L = \pm 1$ (and only on a few occasions $L = 2, 3$, mainly for $B = 0$ T [5, 17]), presumably because they have much higher energy, or because selection rules associated with the envelope wave function prohibit transitions into these states from the $D^0$ ground state.

As discussed in the previous section, detailed modeling of the $D^0X$ states in magnetic field is still beyond the capabilities of modern theoretical physics. Various approximations have been tried (see e.g. Ref. [12], illustrated in Fig. 3.1), but even the very extensive work of Ref. [4] still concludes that it can only link part of the observed levels to theoretical descriptions.

For our goal to assign $m_j$ quantum numbers to $D^0X$ levels, a proper approach should account for the fact that in strong magnetic fields along crystal directions that differ from <100> (in our studies we use [110], building on the results of Ref. [5]), $m_j$ is no longer a good quantum number ($m_j$ states get mixed). We introduce this better in Appendix 3.8. At this stage we did not perform a complete analysis ourselves for expected behavior of this effect. Further, we find that a significant part of the literature discusses $m_j$ values for the $D^0X$ hole while (seemingly) fully ignoring this mixing of $m_j$ states. We carried out and report our analysis in a manner that can link our results to the literature, and also expect that at the field values used in our study the levels are still dominated by one particular $m_j$ state.

## 3.3 Single-laser spectroscopy

For our studies in magnetic fields between $B = 0$ T and 2 T we used transmission studies with a single scanning laser. The photodiode was directly behind the GaAs layer in the cryogenic measurement volume. For improving signal-to-noise, the laser beam was chopped at 6 kHz and the photodiode signal was recorded with a lock-in amplifier. The laser intensities were typically a factor 10 lower than those used in Chapter 2 for the EIT studies. The signals were corrected for small drifts in the laser power by normalizing them to a reference signal (here, and for all other results in this chapter).

Figure 3.2(a) presents results of such measurements for $B = 0$ T. The results for the laser field with H and V polarization were identical. At spectral positions far away from material absorptions, the *transmittance* (defined as the ratio between transmitted and incident optical powers) of the system shows Fabry-Pérot oscillations that modulate the transmittance between values of ∼0.4 and ∼0.9 (for a detailed analysis see Ref. [3]). The Fabry-Pérot effects are mainly due to reflections at the front and back side of the GaAs layer. At the frequency where we resonantly excite the $X_{n=1}$ free exciton, the transmittance is close to zero. In our report here we further mostly present lock-in signals in arbitrary units, as a generic transmission signal. If desirable, the actual values for the corresponding transmittance can be estimated by looking up the spectral lines in Fig. 3.2(a).

The most prominent spectral lines in Fig. 3.2(a) are the broad dips for the $X_{n=1,2,3,...}$ free exciton resonances. The associated modulation of the index of refraction of the GaAs layer is near these resonances so strong that it chirps the Fabry-Pérot oscillations. The spectral distance between the $X_n$ lines for $n = 1, 2, 3...$ is well described by the hydrogen-like series levels for the free exciton [21] (for $n = 2, 3$ we observed them more clearly as separate lines in in other data sets). Spectral lines from $D^0$-$D^0X$ transitions are indicated with red arrows. These have been identified before [4, 5], and the lowest two lines (see also inset) are transitions to a degenerate set of $D^0X$ levels with $L = 0$ (lowest energy) and $L = 1$.

Figure 3.2(b) presents similar measurements for $B = 1$ T, taken with H and V polarization for the laser field. The inset focusses again on transitions to the $D^0X$ levels with $L = 0$ (lowest energies) and $L = 1$. As compared to the data for $B = 0$ T, all features of the spectrum show a significant shift to higher energies, predominantly due to diamagnetic shifts. For the $D^0$-$D^0X$ transitions, this has contributions from both the diamagnetic shift of the $D^0$ systems and the $D^0X$

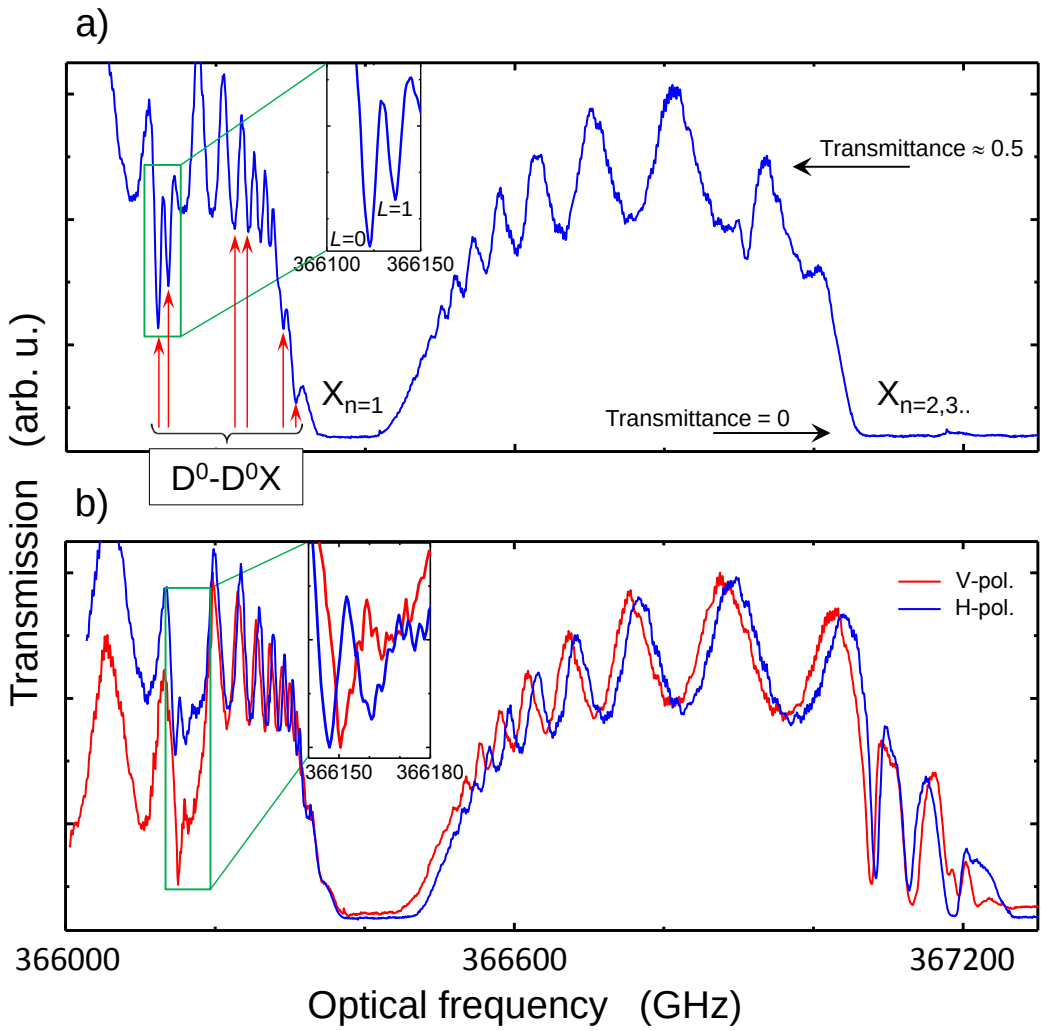


**Figure 3.2:** **(a)** Transmission spectrum of a GaAs layer from a single-laser scan at zero magnetic field (results identical for V and H polarization). The spectrum caries signatures of $D^0$-$D^0X$ transitions (six red arrows, see main text), excitation of free excitons ($X_n$, with $n = 1, 2, 3, ...$), and oscillations from the Fabry-Pérot effect in the GaAs layer (with a chirped wavelength dependence, in particular chirped around the very strong $X_{n=1}$ transition due to the associated wavelength dependence of the refractive index). The transmittance of the system varies between near-zero at the $X_n$ dips and a value of ∼0.5 where only the Fabry-Pérot effect modulates the transmission. The inset zooms in on the two lowest $D^0$-$D^0X$ transitions, which are for $L = 0$ and $L = 1$. **(b)** Similar transmission spectrum recorded for an applied magnetic field of 1 T, for V polarization (red) and H polarization (blue), again with an inset zooming in at the lowest two $D^0$-$D^0X$ transitions.

system.

For the $D^0$-$D^0X$ transitions, both the $L = 0$ line and $L = 1$ line are in fact a manifold of multiple lines that have level splittings that are smaller than the width of these lines. Thus, the energy distance between the $L = 0$ line for the red and blue data cannot be simply interpreted as the Zeeman splitting for the $D^0$ electron. The various levels (for example levels for different $m_j$ values) that belong to the $L = 0$ and $L = 1$ manifolds of $D^0X$ also have Zeeman shifts, and the transition strength into each of them (from a particular $D^0$-electron spin state) will not be the same.

Without bringing in further knowledge about the $D^0X$ levels, these results can thus only give a limited contribution to our $D^0$-$D^0X$ magneto-spectroscopy. For fields below $B \approx 2$ T, the individual levels of the $L = 0$ and $L = 1$ manifolds cannot be resolved, and here these results only provide information about the overall diamagnetic shift for the associated transitions. At $B \approx 2$ T, the single-laser approach also stops working well, since optical pumping into one of the two $D^0$ spin levels causes a loss of signal.

## 3.4 Two-laser spectroscopy

This section presents results from a two-laser spectroscopy approach to studying the $D^0$-$D^0X$ transitions, for fields $B > 2$ T. The main benefit as compared to the single-laser approach is that it remedies the loss of signal due to optical pumping into one of the two $D^0$ spin levels. Before presenting the results, we first introduce the experimental method, and present high-resolution measurements of the Zeeman splitting of the $D^0$ electron. The latter is needed for deriving the energies of $D^0X$ levels from measured values of $D^0$-$D^0X$ transition energies.

### 3.4.1 Experimental method

Our studies with this two-laser approach were again transmission studies with the photodiode directly behind the GaAs layer. For improving signal-to-noise, one of the laser beams was chopped at 6 kHz and the photodiode signal was recorded with a lock-in. One laser was fixed at a frequency where it counteracts optical pumping into one of the two spin states of the $D^0$ system (suitable transitions for this were identified beforehand, using the results of Chapter 2, see also Fig. 3.3). The optical frequency of the other laser was scanned over the range where $D^0$-$D^0X$ transitions occur. Unlike the results in Chapter 2, the chopper

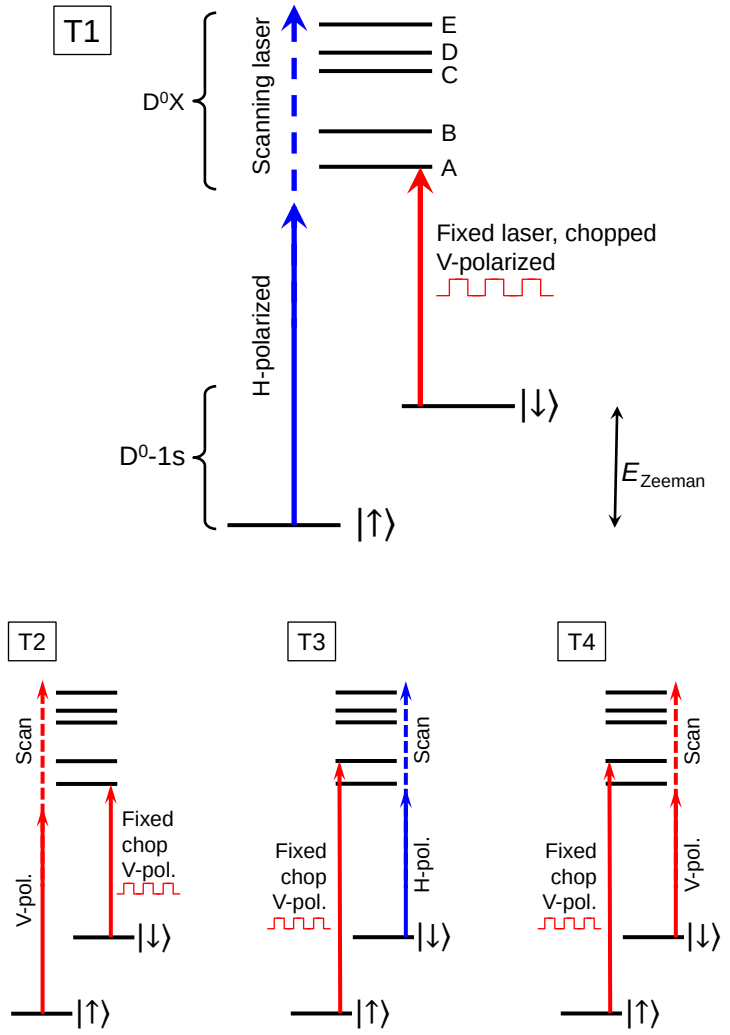


**Figure 3.3:** Energy-level schematics (not to the scale, and with $D^0X$ levels labeled $A$, $B$, $C$,..) for illustrating how with two lasers a pump-assisted spectroscopy (PAS) technique was used for identifying $D^0$-$D^0X$ transitions. Four different configurations are labeled T1, T2, T3, and T4. The colored arrows represent laser fields with H (blue) and V (red) polarization. For the configuration T1, a V-polarized laser field is fixed in frequency to efficiently drive transition from $|\downarrow\rangle$ to one of the lowest levels (labeled $A$) of $D^0X$, such that it counteracts any optical pumping into $|\downarrow\rangle$. An H-polarized laser field scans across $D^0$-$D^0X$ transitions, mainly causing signal when transitions out of $|\uparrow\rangle$ are addressed with this polarization. The PAS signal arises from lock-in detection synchronized to chopping of the fixed laser beam (see main text). For configurations T3 and T4, the fixed laser efficiently drives transitions from $|\uparrow\rangle$ to level $B$ of $D^0X$.

was in the fixed laser beam. Due to this, $D^0$-$D^0X$ transitions are observed as transmission dips in a nearly flat background (see Fig. 3.5(a), much less influence of the Fabry-Pérot effect is seen, for a detailed analysis see Ref. [3]). A signal occurs when both the two lasers drive a transition out of one of the $D^0$ spin levels (competitive optical pumping, or cross modulation). We call this method pump-assisted spectroscopy (PAS). The laser intensities were again typically a factor 10 lower than those used in Chapter 2 for the EIT studies (see also Ref. [3]).

| Label | Polarization of scan laser | Signal due to pumping out of |
|---|---|---|
| T1 | H | $\|\uparrow\rangle$ |
| T2 | V | $\|\uparrow\rangle$ |
| T3 | H | $\|\downarrow\rangle$ |
| T4 | V | $\|\downarrow\rangle$ |

**Table 3.1:** Summary of the essence of the T1, T2, T3 and T4 measurement scheme.

Figure 3.3 presents in more detail how the above scheme was implemented. In particular, we carried out measurements that focussed on transitions out of the $|\uparrow\rangle$ and $|\downarrow\rangle$ state of the $D^0$ system, and studied this with H- and V-polarization for the scanning laser. This gives four measurement configurations, that we label T1, T2. T3 and T4 (see Fig. 3.3). For easy referencing, we summarize the main features of each configuration in Table 3.1.

### 3.4.2 Measuring the $D^0$ Zeeman splitting via EIT

Figure 3.4 presents results for determining the Zeeman splitting for the $D^0$-1$s$ electron with high accuracy via EIT measurements as presented in Chapter 2 (we verified that for these measurements the EIT-peak position had no significant shift from DNP effects). A fit of the observed Zeeman splitting ($E_{Zeeman}$) in this figure to the function $E_{Zeeman} = \gamma_1 B + \gamma_2 B^2$ yields $\gamma_1 = 6.346 \pm 0.004$ GHz T$^{-1}$ and $\gamma_2 = -0.0796 \pm 0.0005$ GHz T$^{-2}$. The (field-dependent) effective Landé g-factor $g = E_{Zeeman}/\mu_B B = h/\mu_B \cdot (\gamma_1 + \gamma_2 B)$ can thus be determined with an accuracy of about one part in thousand ($\mu_B$ is the Bohr magneton). We use these values in our analysis of the $D^0$-$D^0X$ transition energies in the remainder of this chapter. As an indication for the values of the electron g-factor that result from this expression, we present them here for three values of $B$ (minus sign taken from the literature):

$g = -0.4534 \pm 0.0003$ for zero field,

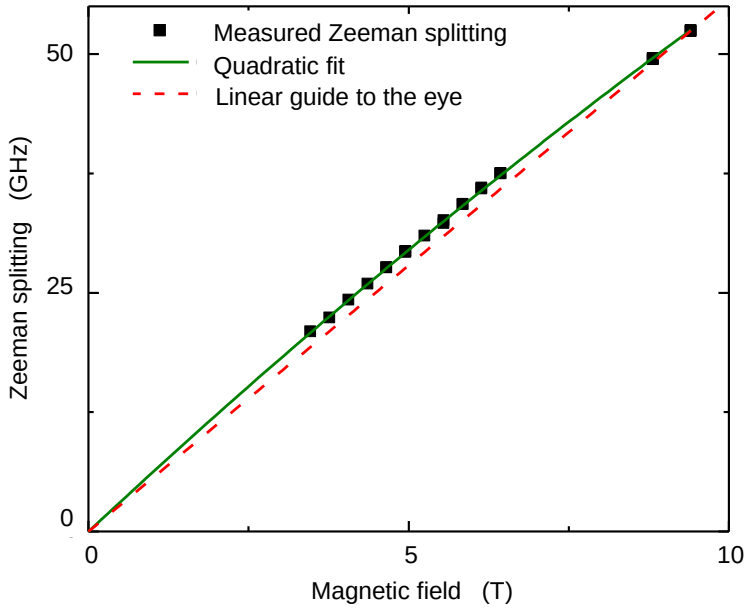


**Figure 3.4:** The Zeeman splitting for the $D^0$-1$s$ electron, determined with high precision by deriving it from the EIT resonance (measured as in Chapter 2), as a function of applied magnetic field. The red dashed line going through the origin is a guide to the eye for linear dependence, and shows that the measured Zeeman splitting has a weakly nonlinear dependence on magnetic field. The green curve is a quadratic fit, see main text.

$g = -0.4170 \pm 0.0006$ at a field of $B = 6.4$ T, and
$g = -0.3965 \pm 0.0007$ at a field of $B = 10$ T.
These observations are in good agreement with earlier high-resolution studies of the $D^0$-electron Zeeman splitting [4, 5].

### 3.4.3 Two-laser spectroscopy of $D^0X$ levels

Figure 3.5(a) presents results from the two-laser spectroscopy schemes T1..T4, introduced in this section. Resonances with $D^0$-$D^0X$ transitions appear as dips. The results for T3 and T4 have been shifted by $E_{Zeeman}$ to higher energies, such that dips for a transition to a particular $D^0X$ level appear at the same optical frequency as for T1 and T2 results. The traces are normalized to a ∼0.1 reduction of the signal as in Fig. 3.2(a).

The traces in Fig. 3.5(a) show prominent dips for known transitions (Chapter 2), and various smaller features which can either result from weaker $D^0$-$D^0X$

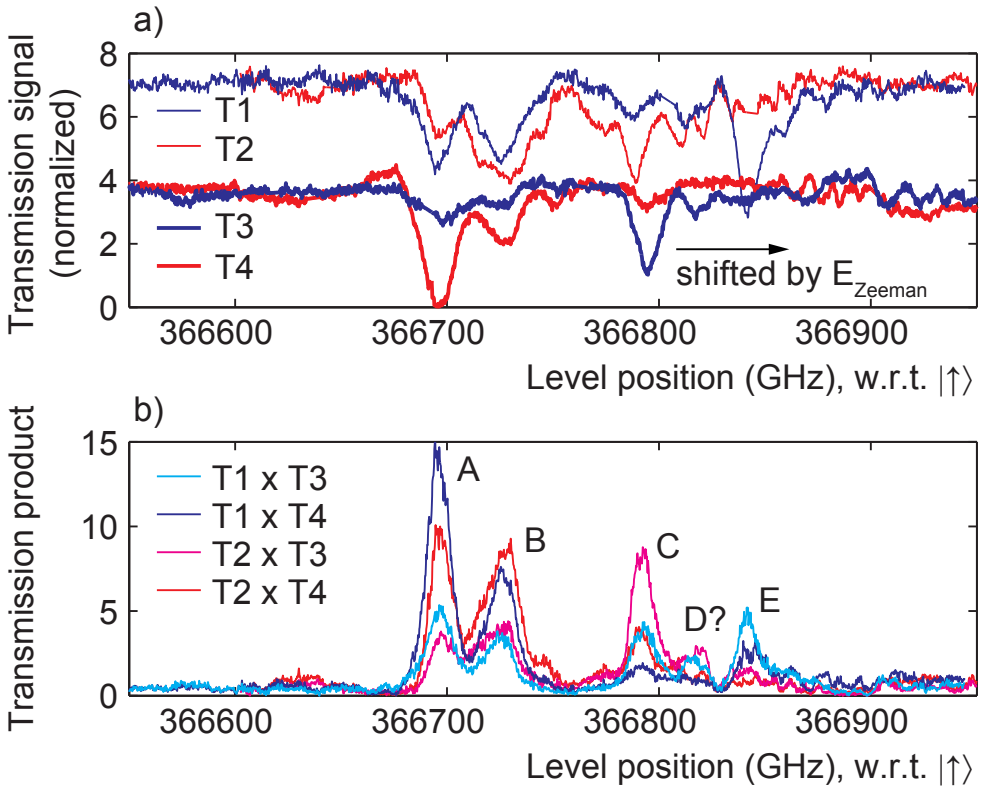


**Figure 3.5:** **(a)** Normalized pump-assisted spectroscopy (PAS) results from configurations T1-T4 (see main text, traces offset for clarity). Resonances with $D^0$-$D^0X$ transitions appear as dips in the transmission signal. Results from T3 and T4 are displayed after shifting them to higher frequencies over a distance that corresponds to $E_{Zeeman}$, such that resonance frequencies (dip positions) for specific $D^0X$ levels observed in T3 and T4 traces coincide with the corresponding resonances in T1 and T2 traces. The occurrence of dips thus identify the energy of $D^0X$ level with respect to the energy of the $|\uparrow\rangle$ level. **(b)** Traces that represent the product of trace T1 and T3 of panel (a) (baseline subtracted and inverted), and similar cases as labeled. Peaks in the T1×T3 trace only occur when both the T1 and the T3 trace contain a dip from a transition to a particular $D^0X$ level, from $|\uparrow\rangle$ and $|\downarrow\rangle$ respectively. This representation shows peaks (labeled $A$, $B$, $C$,...) that reflect $D^0$-$D^0X$ transitions while uncorrelated noisy structure in the original T1 and T3 traces is suppressed. It also helps with evaluating the polarization dependence of the transitions, see main text.

transitions (given the polarization of the scanning laser) or from spurious effects such as a residual influence of the Fabry-Pérot effect in the GaAs layer. To better discriminate these cases, we identify $D^0$-$D^0X$ transitions (and better identify

their sensitivity to either H- or V-polarization) by processing these signals as in Fig. 3.5(b). This plot presents products of signals such as T1×T3 (original signals inverted and background set to zero). These product-signals (such as T1×T3) only show peaks when dips at a particular frequency were present in both the T1 and T3 trace, thus removing a portion of the spurious contributions. Further discrimination between peaks of weak transitions and spurious structure on these traces was obtained by following whether the peaks consistently keep appearing when altering the magnetic field in small steps (see Fig. 3.6). By also looking at the height and polarization dependence of the peaks, this approach also confirmed that the order of peaks did not have crossings in the field range $B = 2.5$ T to 9.4 T. In Fig. 3.5(b), we label peaks as $A$, $B$, $C$,... in a manner that agrees with how we used this labeling in earlier publications from our team. However, as presented in Fig. 3.6(c), we will introduce new generic labeling Line 1..Line 8 for the observed lines with the 8 lowest energies, for an analysis independent of earlier assumptions.

Notably, a peak in Fig. 3.6(c) directly identifies the energy of a $D^0X$ level with respect to the energy of the $|\uparrow\rangle$ state of the $D^0$ electron. In our further analysis as a function of magnetic field, we will always present the energies of $D^0X$ levels with respect to the energy of the $|\uparrow\rangle$ level at each particular magnetic field. The observed shifts in the energy of the $D^0X$ level as a function of field thus have contributions that include Zeeman and diamagnetic shifts from both the $|\uparrow\rangle$ level of $D^0$ and the particular $D^0X$ level.

Energies of $D^0X$ levels derived in this manner (from the set peaks labeled as Line 1..Line 8, Fig. 3.6(c)) were analyzed from data as in Fig. 3.5 obtained at magnetic fields between $B = 2.5$ T and 9.4 T. The results are presented in Fig. 3.6(a). This figure also presents data for $B < 2$ T, for the $D^0X$ levels with $L = 0$ and $L = 1$ (for these points we applied a corresponding approach for defining the energies with respect to $|\uparrow\rangle$ [24]). The full data set presented in this manner shows that all transitions associated with Line 1..Line 8 show a strong energy increase with field (about 1000 GHz over 9.4 T) due to diamagnetic shifts, while splittings between $D^0X$ levels increase continuously, up to values on the order of 50 GHz at 9.4 T. The diamagnetic shift shows the expected behavior of a parabolic dependence on $B$ at low fields, crossing over to a linear dependence at high fields [21], with the cross-over at about 5 T [4, 5, 21]. In the next section we aim to assign quantum numbers $L$ and $m_j$ to the $D^0X$ levels associated with Line 1..Line 8, and we aim to link and compare several aspects of this data set to earlier $D^0X$ studies that have been reported.

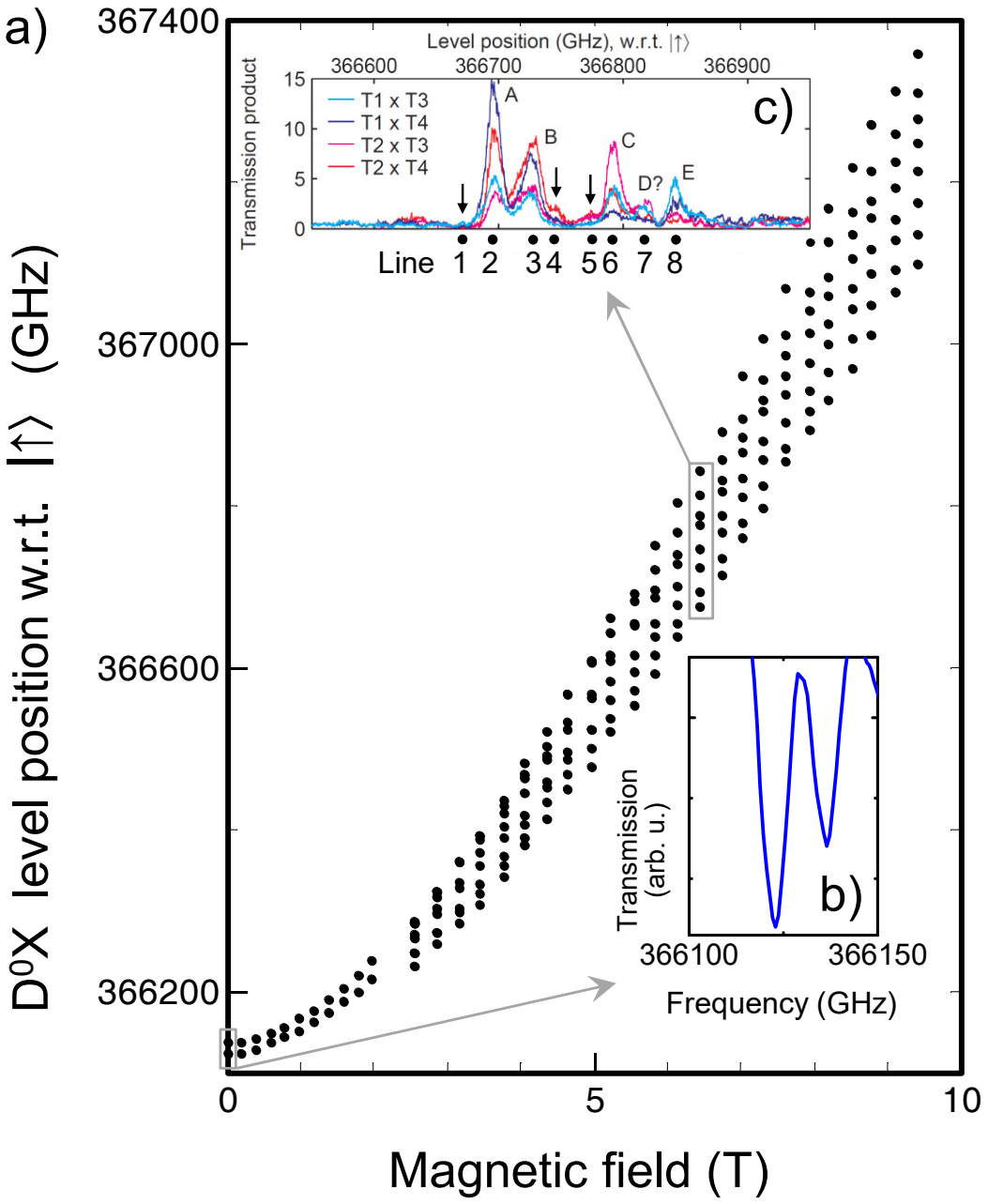


**Figure 3.6:** **(a)** Magnetic-field dependence of the lowest 8 observed $D^0X$ levels, characterized as a transition frequency with respect to the $|\uparrow\rangle$ level. For fields $B > 2$ T, the level positions are derived from results as in Fig. 3.5(b) (also in panel **(c)**, for $B = 6.4$ T). For fields $B < 2$ T, only two levels can be identified from results as in Fig. 3.2 (also in panel **(b)**, for $B = 0$ T).

## 3.5 Analysis and discussion

Using various approaches (in part explained here, in part further below), Table 3.3 presents the outcome of our attempt to assign quantum numbers $L$ and $m_j$ to the $D^0X$ levels associated with Line 1..Line 8. We assumed that all of these lowest levels should have quantum number $L = 0$ or $L = 1$ [4, 5]. Assigning a value of $L$ is in part based on checking whether a full fit to a line (details explained in Appendix 3.9) yields a smooth connection between the high-field data and either the $L = 0$ or the $L = 1$ data at low field. A clear case is illustrated in Fig. 3.9: trying a fit (gray) that connects the high-field data for Line 2 to the $L = 0$ low-field data gives a much more convincing result than such a fit (red) to the $L = 1$ low-field data. Further, we studied the splittings between pairs of lines (see for example Line 4−Line 2 and Line 8−Line 6 in Fig. 3.8), for the high-field data ($B > 2.5$ T). In some cases this showed linear behavior (Fig. 3.8(a)), while in another cases it clearly differed from linear behavior (Fig. 3.8(b)). Behavior that strongly differs from linear points to a different diamagnetic shift for the two lines, and thereby a different $L$ value for the two lines.

For assigning an $m_j$ value to a $D^0X$ level, we looked at the polarization dependence of the line. A clear example is Line 2 (see Table 3.3): it has a strong transition from $|\uparrow\rangle$, but only for H polarization, and a strong transition from $|\downarrow\rangle$ for V polarization. This points to a $\Delta m_j = \pm 1$ transition [21] from $|\uparrow\rangle$ and a $\Delta m_j = 0$ from $|\downarrow\rangle$ (see also Chapter 2), and thus to $m_j = -\frac{1}{2}$ for the $D^0X$ level. Another rather clear example is Line 8: here there is only a strong response from $|\uparrow\rangle$ for H polarization ($\Delta m_j = \pm 1$), which points to $m_j = +\frac{3}{2}$ for the $D^0X$ state. However, for several of the lines the polarization dependence does not yield a clear indication for an $m_j$ value that governs the level predominately.

A different approach to finding a match with the physical picture presented in Section 3.2 is to search for a group of four lines with energy splittings between them that behave as the Zeeman splittings of the hole for the lowest $D^0X$ levels (electronic state with $j = \frac{3}{2}$ and $m_j = -\frac{3}{2}, -\frac{1}{2}, +\frac{1}{2}, +\frac{3}{2}$). The expected linear level splittings (in GHz T$^{-1}$) are illustrated in Fig. 3.7. The relevant g-factors for the $m_j = \pm\frac{3}{2}$ and $m_j = \pm\frac{1}{2}$ states are calculated in Appendix 3.8. Table 3.2 presents the observed splittings between Line 1..Line 8, derived from fits as presented in Fig. 3.8. We now search for a correspondence between a part of Table 3.2 and Fig. 3.8(b). Since lines may have crossed before the field reaches 2.5 T, correspondence may appear in a pattern with four lines of Line 1..Line 8 that are not consecutive. Examples that roughly match are formed by:

| | Line 1 | Line 2 | Line 3 | Line 4 | Line 5 | Line 6 | Line 7 |
|---|---|---|---|---|---|---|---|
| **Line 2** | 3.4 | - | | | | | |
| **Line 3** | 7.4 | 4.0 | - | | | | |
| **Line 4** | 10.9 | 7.5 | 3.5 | - | | | |
| **Line 5** | 15.6 | 12.2 | 8.1 | 4.7 | - | | |
| **Line 6** | 18.2 | 14.8 | 10.8 | 7.3 | 2.6 | - | |
| **Line 7** | 22.1 | 18.7 | 14.7 | 11.2 | 6.5 | 3.9 | - |
| **Line 8** | 27.1 Other diam. | 23.7 Other diam. | 19.7 Other diam. | 16.2 Other diam. | 11.5 Other diam. | 8.9 Other diam. | 5.0 Other diam. |

**Table 3.2:** This table summarizes how the measured splitting between a Line $N$ and a Line $M$ (where $N,\ M = 1..8$) increases as a function of magnetic field. It is analyzed by fitting a linear dependence (through zero). The results are presented as a value in GHz $\mathrm{T}^{-1}$. The uncertainty for each value is about $\pm 1$ GHz $\mathrm{T}^{-1}$. The indications *Other diamagnetic shift* for Line 8 indicate that the splitting with the other Lines 1-7 is clearly not linear (see main text).

Line 1, 2, 4, 5;
Line 2, 3, 5, 6;
Line 3, 4, 6, 7.

However, none of these sets then also show consistent agreement with the values for $m_j$ as presented in Table 3.3 (not even separately for a pair $m_j = \pm\frac{3}{2}$ for the outer two levels, or $m_j = \pm\frac{1}{2}$ for the inner two). We thus conclude that we cannot convincingly identify a set of four (or even two) lines with the behavior of a manifold with $m_j = -\frac{3}{2}, -\frac{1}{2}, +\frac{1}{2}, +\frac{3}{2}$, that at the same time also all have the same quantum number $L = 0$ or $L = 1$.

Despite this limited success for assigning quantum numbers to $D^0X$ levels, our results do establish –in particular via the strong lines that we labeled $A$ (Line 2) and $B$ (Line 3)– the correspondence with related results in the literature [4, 5], both for the polarization selection rules and the magneto-spectroscopic shifts (see Appendix 3.9). There is only one outspoken difference with Ref. [5]: our data favors assigning $L = 0$ to level $A$ instead of $L = 1$.

| Line | Letter label | Selection rules | $L$ B = 0 extrapol. | $m_j$ sug. sel. rules |
|---|---|---|---|---|
| 1 | - | From $\|\uparrow\rangle$ weak V<br>From $\|\downarrow\rangle$ weak, not clear | $L$ = 0 | $m_j$ = +1/2 ? |
| 2 | A | From $\|\uparrow\rangle$ strong H<br>From $\|\downarrow\rangle$ strong V | $L$ = 0 | **$m_j$ = -1/2** |
| 3 | B | From $\|\uparrow\rangle$ strong H and V<br>From $\|\downarrow\rangle$ strong V | $L$ = 0 | $m_j$ = -1/2 ? |
| 4 | - | From $\|\uparrow\rangle$ very weak V<br>From $\|\downarrow\rangle$ weak V | ? | $m_j$ = -1/2 ? |
| 5 | - | From $\|\uparrow\rangle$ weak V<br>From $\|\downarrow\rangle$ weak, not clear | ? | $m_j$ = +1/2 ? |
| 6 | C | From $\|\uparrow\rangle$ strong V<br>From $\|\downarrow\rangle$ strong H | ? | **$m_j$ = +1/2** |
| 7 | D | From $\|\uparrow\rangle$ strong V<br>From $\|\downarrow\rangle$ strong H | ? | **$m_j$ = +1/2** |
| 8 | E | From $\|\uparrow\rangle$ strong H<br>From $\|\downarrow\rangle$ weak, not clear | $L$ = 1 | **$m_j$ = +3/2** |

**Table 3.3:** This table summarizes the analysis of the properties of the observed transitions and associated $D^0X$ states for Lines 1-8 of Fig. 3.6. The second column relates our numbering Line 1..8 to $D^0X$ level labeling $A..E$ that we and others used before. The column *Selection rules* presents whether a transition for Line 1..8 is relatively strong or weak, and to what polarization (H or V) it couples to most strongly, both for that transition out of $|\uparrow\rangle$ and $|\downarrow\rangle$. This information is used for identifying the $m_j$ quantum number of the hole in the associated $D^0X$ state, as presented in the last column. The column for quantum number $L$ presents whether the associated $D^0X$ level has $L = 0$ or $L = 1$, which we determined by checking whether the diamagnetic shift for a Line 1..8 at $B > 2$ T links convincingly to the low-field shifting of the $L = 0$ or the $L = 1$ transition, and by checking whether the splitting between a pair of Lines has a linear dependence on field (indicating that they are Zeeman sub-levels of a state with the same $L$ quantum number).

## 3.6 Conclusions

In this chapter we presented a full magneto-spectroscopic study of the lowest 8 optically-active $D^0X$ levels, and the associated optical transitions, for fields

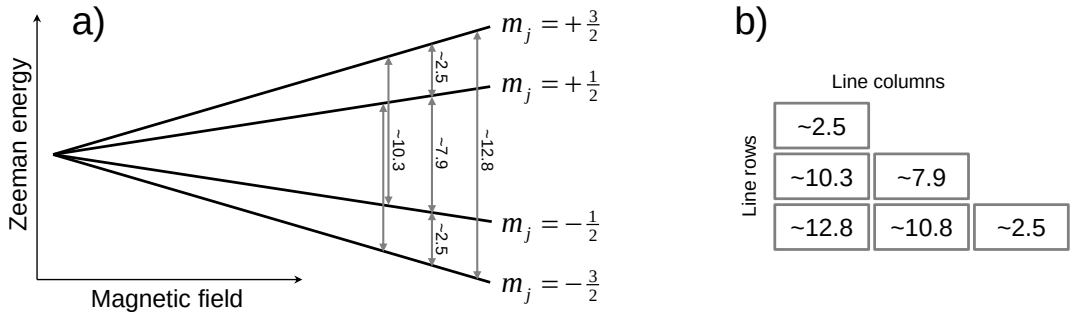


**Figure 3.7:** **(a)** A schematic illustrating the theoretically expected Zeeman shifts, and the corresponding splittings between levels (with values in GHz $T^{-1}$), for the four $m_j$ levels of a $j = \frac{3}{2}$ hole. **(b)** In relation to Table 3.2, the theoretically expected Zeeman splittings (in GHz $T^{-1}$) presented in table form.

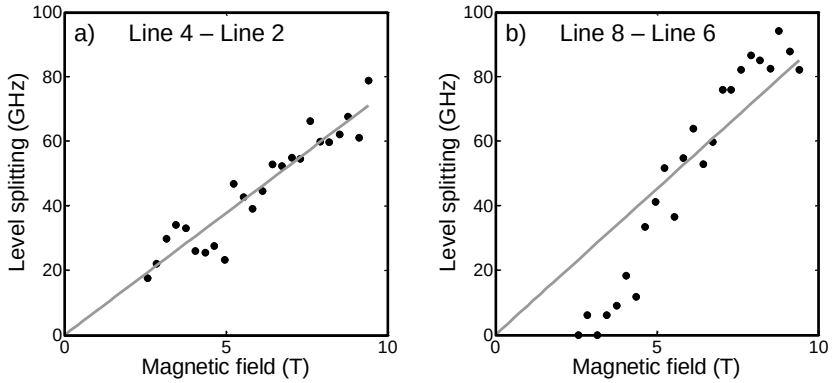


**Figure 3.8:** **(a)** The observed level splitting (dots) between Line 4 and Line 2 of Fig. 3.6(a). The gray line is a linear fit through the origin. **(b)** Similarly, the level splitting between Line 8 and Line 6 of Fig. 3.6(a).

between 0 and 9.4 T. We concentrated on the case where the field is applied along the [110] crystal direction. While the experimental results establish at a phenomenological level detailed information about the spectrum and the polarization selection rules, our goal to obtain insight in the quantum numbers $L$ and $m_j$ of the 8 $D^0X$ states had only limited success. The results do establish how the results obtained with our configuration and measurement method link to state-of-the-art results in the literature [4, 5]. The spectroscopic study did not reveal a reason for the large set of results by our team that indicate that observing the EIT effect between 7 T and 8 T is much more difficult than at other magnetic fields. Notably, related work in our team showed that this can also not be at-

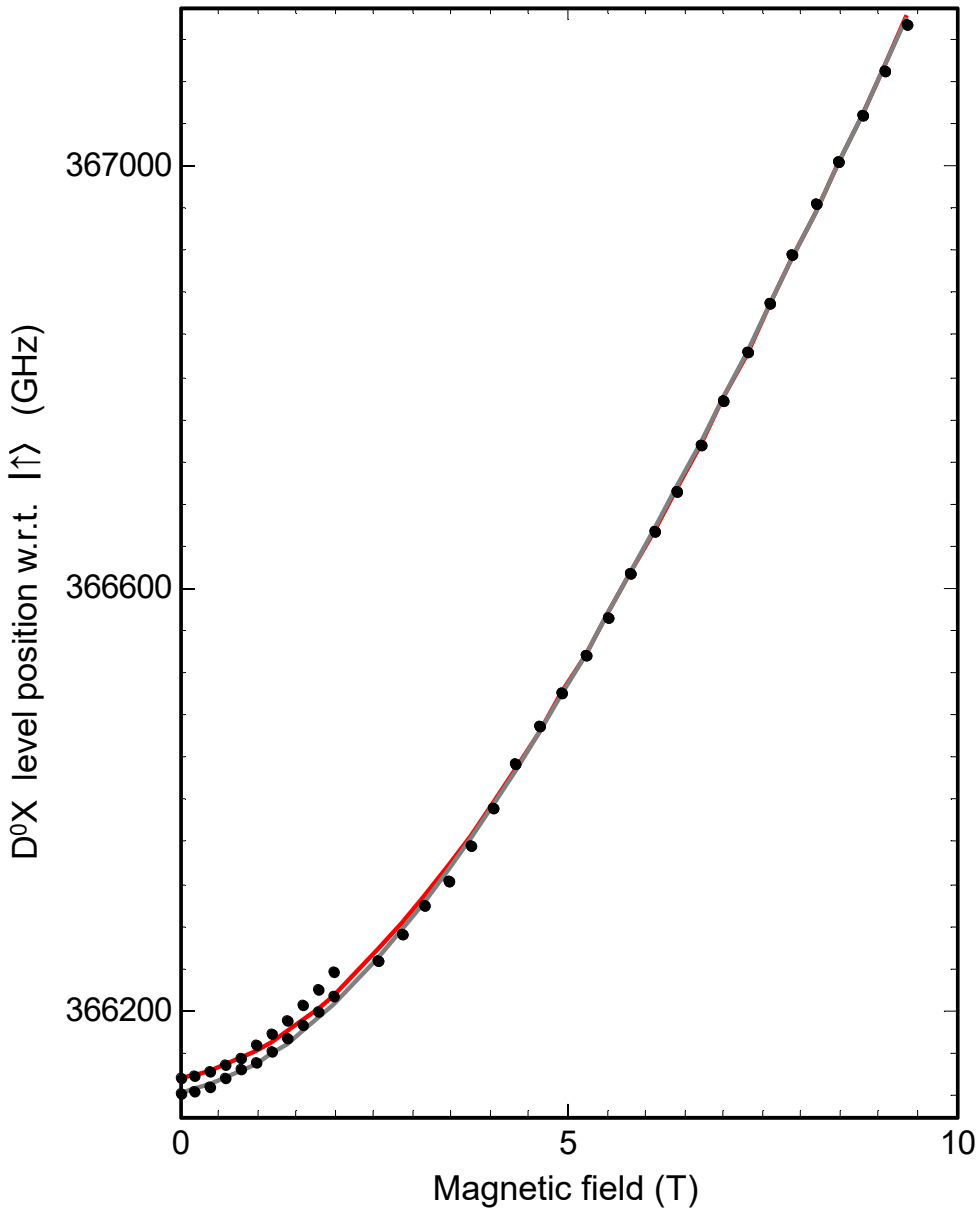


**Figure 3.9:** Fits (gray, red) of the combined diamagnetic and Zeeman shift for Line 2 (dots, high field) of Fig. 3.6(a), either assumed to link to the $L = 0$ (gray) or $L = 1$ (red) observations for low fields (see main text for details). For the Zeeman shift the fit assumes Line 2 is for a hole with $m_j = -\frac{1}{2}$.

tributed to Fabry-Pérot effects in the GaAs layer [3], and the physics behind this observation thus remains an open problem.

## Acknowledgements

We thank B. H. J. Wolfs for help and the Dutch Foundation for Fundamental Research on Matter (FOM), the Netherlands Organization for Scientific Research (NWO), and the German programs DFG-SFB 491 and BMBF-nanoQUIT for funding.

## 3.7 Appendix: Notes on notations used in the literature

Rather than using the labels Line 1..Line 8 for the observed $D^0X$ levels, in other chapters of this thesis and in related publications from our team we label $D^0X$ levels as $A$, $B$, $C$,.. (see Table 3.3). Here the associated *transitions* are labeled as $A$ when it is an excitation from $|\downarrow\rangle$, and $A^*$ when it is an excitation from $|\uparrow\rangle$, see Fig. 3.3.

We used this notation following the earlier work by Fu *et al.* [5, 18], and in particular assign the same label to the transitions $A$, $A^*$ and $B$, $B^*$. Fu *et al.* also applied the magnetic field along [110]. The difficulty in assigning quantum numbers to $D^0X$ levels is from this body of work also apparent from the fact they initially assigned $L = 0$, $m_j = -\frac{3}{2}$ to the $A$ level [18], while the later publication of the same data reported it as $L = 1$, $m_j = -\frac{1}{2}$ [5]. In other chapters of this work, $A$ and $B$ were associated with $L = 0$, while low-energy levels associated with $L = 1$ were labeled as $A_1$, $B_1$, *etc.*

In turn, Fu *et al.* used their notation following Karasyuk *et al.* [4]. The use of $A$, $A^*$ and $A_1$ *etc.* by Karasyuk *et al.* is thus very similar (while $a$, $a^*$ and $a_1$ refer to transitions that relax $D^0X$ states to $2p$ levels of $D^0$ rather than the $1s$ ground state). It should be noted that for most of the studies Karasyuk *et al.* applied the magnetic field along [100]. This also has consequences for the g-factors and order of $m_j$ labeling on Zeeman levels of the $D^0X$ hole (better defined in the next section): $g_{\frac{1}{2}} = -0.32$ is negative while $g_{\frac{3}{2}} = +0.35$ is positive. This notation and $m_j$ assignment is also used in the recent Refs. [19, 23]. Concerning Ref. [4], they use $J$ for the total angular momentum (electronic orbital and spin) of the full $D^0X$ system, while $j$ refers to that of the $D^0X$ hole alone (but not strictly consistent). A later part of the publication uses $I$, $M_I$ for the total angular momentum of the full $D^0X$ system. In other parts, they switch to using the notation $S_{3/2}$, $P_{3/2}$, *etc.* (where according to conventional spectroscopic notation $S$ refers to $L = 0$, $P$ to $L = 1$, and the subscript to the value of $J$ as introduced

in this paragraph).

In relation to the above, Ref. [11] uses different notation on a few aspects: they use $J$, $m_j$ (in some cases also for the $D^0$ electron spin) for $j$, $m_j$ and they use $l$ for $L$. Further, there seem to be typos: for the use of $J$ they still sometimes use $j$ or $\overrightarrow{j}$ at the end of the publication, and $l$ also appears as $\overrightarrow{I}$, $I$ or $\mathbf{1}$. Also this publication switches in part to the notation that uses $S_{3/2}$, $P_{3/2}$, *etc.* as in Ref. [4].

## 3.8 Appendix: Derivation of hole g-factors

In this Appendix we present the effective g-factors for the hole states for the situation that applies to our experiments. It should be noted that there are two different conventions in parallel for reporting g-factor values. In particular, the Zeeman energy of a (quasi-)spin *level* (not a spin splitting), characterized by a particular $m_j$ value, is either written as $E_{m_j} = g_{case1}\,\mu_B B$ or $E_{m_j} = m_j\,g_{case2}\,\mu_B B$ (the latter case is commonly used for the electron). For the expression with $g_{case1}$ the factor $m_j$ is incorporated in the g-factor. For the hole g-factors reported here we will use case 1.

For calculating the hole g-factors we use Ref. [7]. This publication gives for the Zeeman contribution $E_{m_j}$ to the energies of hole states with $j = \frac{3}{2}$ and $m_j = -\frac{3}{2}, -\frac{1}{2}, +\frac{1}{2}, +\frac{3}{2}$ (using Eq. 56a-d of this publication, which applies for $B$ along [110] and the $\Gamma_8$ representation of $j = \frac{3}{2}$ holes, see also Ref. [23], start of Section III). For introducing symbols and notation see Ref. [25]. This yields

$$E_{\pm\frac{3}{2}} = \mu_B g_2^{'} B[\pm\Delta \pm (\frac{1}{2}\frac{g_1^{'}}{g_2^{'}} + \frac{7}{8})], \tag{3.1}$$

and

$$E_{\pm\frac{1}{2}} = \mu_B g_2^{'} B[\pm\Delta \mp (\frac{1}{2}\frac{g_1^{'}}{g_2^{'}} + \frac{7}{8})]. \tag{3.2}$$

Notably, $m_j$ is for a strong field along [110] no longer a good quantum number (see Ref. [11], top left p. 7015 and top left p. 7017). We can still use $m_j$ as labels since the levels evolve out of these $m_j$ states at zero field. This is the reason that we should calculate effective g-factors $g_{\frac{3}{2}}$ and $g_{\frac{1}{2}}$ from the material parameters $g_1^{'}$ and $g_2^{'}$, which are the bare spherically symmetric and asymmetric g-factors.

The values for GaAs for $g_1^{'} = -0.40$ and $g_2^{'} = +0.33$ are given in Ref. [4] (Table III, which uses notation $g_1$ and $g_2$). When expressing the energies of the

(quasi-)spin levels as

$$E_{\pm\frac{3}{2}} = \pm g_{\frac{3}{2}}\mu_B B \tag{3.3}$$

and

$$E_{\pm\frac{1}{2}} = \pm g_{\frac{1}{2}}\mu_B B \tag{3.4}$$

the valid hole g-factor values are

$$g_{\frac{3}{2}} = +0.485, \tag{3.5}$$

$$g_{\frac{1}{2}} = +0.281. \tag{3.6}$$

For an applied field along [100] the equations corresponding to the above result in $g_{\frac{3}{2}} = g_1^{'} + \frac{9}{4}g_2^{'}$ and $g_{\frac{1}{2}} = g_1^{'} + \frac{1}{4}g_2^{'}$, which results in $g_{\frac{3}{2}} = +0.35$ and $g_{\frac{1}{2}} = -0.32$ [7](Eq. 19), [4].

## 3.9 Appendix: Fitting the magneto-spectroscopy results

The traces as in Fig. 3.9 contain energies $E_{\mathrm{Line}N}$ of $D^0X$ levels (each associated with a Line $N$), measured with respect to the energy of the state $|\uparrow\rangle$ of the $D^0$ system. Thus, to analyze and fit the energy shift in magnetic field, we set up an approach that accounts for four terms,

$$E_{\mathrm{Line}N} = E_0 + \frac{1}{2}E_{Zeeman} + E_{m_j} + E_{diam}. \tag{3.7}$$

The first term $E_0$, is a phenomenological constant, and is simply the observed energy associated with the $L = 0$ or $L = 1$ line at $B = 0$ T. The second term $+\frac{1}{2}E_{Zeeman}$ (see Section 3.4.2) accounts for the Zeeman shift of $|\uparrow\rangle$. The third term (in some cases applied by trial and evaluation for finding a consistent picture) is the Zeeman term for the $D^0X$ level, which is the term $E_{m_j}$ as presented in Appendix 3.8. For this we need to use (or try) an $m_j$ value, for which we use the findings presented in Table 3.3. The fourth term accounts for diamagnetic-shift contributions from both the $|\uparrow\rangle$ level and the relevant $D^0X$ level. We follow Ref. [4] and incorporate that into one single *phenomenological* expression for the two diamagnetic-shift contributions, since taking them separately gives too many free parameters. The expression used is

$$E_{diam} = \mu_B \frac{m_e}{m^*}\sqrt{B_0^2 + B_1 B + B^2}. \tag{3.8}$$

Here $m_e$ is the free electron mass, $m^*$ is a phenomenological effective mass value that is some mixed value for that of the electron and the hole (indicating the expected order of magnitude).

Thus, we set up least-squares fitting with only three free parameters: $m^*$, $B_0$ and $B_1$. Notably, for traces as in Fig. 3.9 (and after removing the Zeeman contributions), $B_1$ governs the slope at low fields, $m^*/m_e$ governs the asymptotic slope at high fields, and $B_0$ sets the field where the trace crosses over from parabolic to linear. Since the behavior of holes in GaAs is highly anisotropic, the values of $m^*$, $B_0$ and $B_1$ can show a weak dependence on the value of $L$ and $|m_j|$ [4].

The character of this model for fitting yields a strong inter-dependence between the resulting values for $m^*$, $B_0$ and $B_1$, and could yield good fits (similar to the lines in Fig. 3.9) for a range of such values (defining an error-bar range). Here the value for $m^*/m_e = 0.075 \pm 0.005$, with the best fits consistent with the value $m^*/m_e = 0.0739$ reported by Ref. [4], such that we continued with a two-free-parameter approach, and $m^*/m_e$ fixed at =0.0739. This did yield $B_0 = 5 \pm 1$ T and $B_1 = 0.8 \pm 0.2$ T, where the error bar is dominated by the fact that similar quality fits can be obtained via inter-adjustment of the two fit parameters. These values also show agreement with the results in Ref. [4], both in value and possible depth and error bar of the analysis.

# References

[1] Bernhard Urbaszek, Xavier Marie, Thierry Amand, Olivier Krebs, Paul Voisin, Patrick Maletinsky, Alexander Högele, and Atac Imamoglu, *Nuclear spin physics in quantum dots: An optical investigation*, Rev. Mod. Phys. **85**, 79 (2013).

[2] V. A. Karasyuk, M. L. W. Thewalt, and A. J. SpringThorpe, *Strain effects on bound exciton luminescence in epitaxial GaAs studied using a wafer bending technique*, Phys. Stat. Sol. B **210**, 353 (1998).

[3] J. P. de Jong, *Optically addressing semiconductor electron-spin ensembles with tunable nuclear-spin environments* (PhD thesis, Universisty of Groningen, 2016).

[4] V. A. Karasyuk, D. G. S. Beckett, M. K. Nissen, A. Villemaire, T. W. Steiner, and M. L. W. Thewalt, *Fourier-transform magnetophotoluminescence spectroscopy of donor-bound excitons in GaAs*, Phys. Rev. B **49**, 16381 (1994).

[5] K.-M. C. Fu, *Optical Manipulation of Electron Spins Bound to Neutral Donors in GaAs* (PhD thesis, Stanford University, 2007).

[6] R. R. Sharma and S. Rodriguez, *Exciton-Donor Complexes in Semiconductors*, Phys. Rev. **159**, 649 (1967).

[7] A. K. Bhattacharjee and S. Rodriguez, *Group-Theoretical Study of the Zeeman Effect of Acceptors in Silicon and Germanium**, Phys. Rev. B **6**, 3836 (1972).

[8] D. C. Reynolds, C. W. Litton, T. C. Collins, and S. B. Nam, *Zeeman studies of photolnminescence of excited terminal states of a bound-exciton-donor-complex in GaAs*, Phys. Rev. B **12**, 5723 (1975).

[9] D. C. Reynolds, C. W. Litton, T. C. Collins, and S. B. Nam, *Free-exciton energy spectrum in GaAs*, Phys. Rev. B **13**, 761 (1976).

[10] D. C. Herbert, *Electron correlation and bound excitons in semiconductors*, J. Phys. C: Solid State Phys. **10**, 3327 (1977).

[11] W. Rühle and W. Klingenstein, *Excitons bound to neutral donors in Inp*, Phys. Rev. B **18**, 7011 (1978); Erratum in Phys. Rev. B **20**, 818 (1979).

[12] J. Rorison, D. C. Herbert, P. J. Dean, and M. S. Skolnick *A model for the neutral donor bound exciton system in InP at high magnetic field*, J. Phys. C: Solid State Phys. **17**, 6435 (1984).

[13] F. Meier and B. P. Zakharchenya (eds.), *Optical orientation*, (Elsevier, Amsterdam, 1984).

[14] D. C. Herbert and J. M. Rorison, *Oscillator strengths for excitons bound to impurities and quantum wells*, Solid St. Comm. **54**, 343 (1985).

[15] D. C. Reynolds, D. C. Look, and B. Jogai, G. L. McCoy, and K. K. Bajaj, *Magnetophotoluminescence study of excited states associated with donor bound excitons in high purity GaAs*, Phys. Rev. B **53**, 1891 (1996).

[16] M. Cardona and P. Y. Yu, *Fundamentals of Semiconductors* (Springer-Verlag, 2001).

[17] D. G. Allen and M. S. Sherwin, *Optically detected measurement of the ground-state population of an ensemble of neutral donors in GaAs*, Phys. Rev. B **72**, 035302 (2005).

[18] K.-M. C. Fu, C. Santori, C. Stanley, M. C. Holland, and Y. Yamamoto, *Coherent Population Trapping of Electron Spins in a High-Purity n-Type GaAs Semiconductor*, Phys. Rev. Lett. **95**, 187405 (2005).

[19] T. Wang, R. Rajapakse, and S. F. Yelin, *Electromagnetically induced transparency and slow light with n-doped GaAs*, Optics Communications **272**, 154 (2007).

[20] M. Sladkov, A. U. Chaubal, M. P. Bakker, A. R. Onur, D. Reuter, A. D. Wieck, and C. H. van der Wal, *Electromagnetically induced transparency with an ensemble of donor-bound electron spins in a semiconductor*, Phys. Rev. B **82**, 121308(R) (2010).

[21] Mark Fox, *Optical Properties of Solids* ($2^{\text{nd}}$ ed., Oxford University Press, 2010).

[22] Ivan Pelant and Jan Valenta, *Luminescence spectroscopy of semiconductors* (Oxford University Press, 2012).

[23] R. M. Rajapakse and S. F. Yelin, *Optical coupling of a donor bound exciton under magnetic field and under applied stress* (Univ. of Connecticut preprint, 9 March 2012).

[24] Here we took the average energy of the two peak positions as observed H- and V-polarization, and added $\frac{1}{2}E_{Zeeman}$ using the data of Section 3.4.2.

[25] For a complete introduction of notation we refer to the original publication. Notably, in the main text we immediatly write $\frac{g_1}{g_2}$ rather than using $p$, where $p = \frac{g_1}{g_2}$. We apply the mentioned assumption that $s_2 = s_3 = 0$. This yields for the mentioned factors $\Delta = \Delta_\pm = \frac{1}{4}\sqrt{16p^2 + 68p + 79}$. Also note that for our analysis we can leave out the term $[s_1 + \frac{5}{4}(s_2 + s_3)]B$ since it is the same for all four $m_j$ levels.

# Chapter 4

# Electromagnetically induced transparency as probe for nuclear spin polarization around donor-bound electrons in GaAs

**Abstract**

We study how electromagnetically induced transparency (EIT) with donor-bound electrons in high-purity $n$-GaAs can be applied as a probe for the dynamics of nuclear spin polarization. The localized donor electrons have hyperfine interaction with surrounding nuclear spins, and probing the electron spin splitting with EIT thus reflects the nuclear spin polarization. We also apply that scanning spectroscopy around the EIT resonance predominantly acts as optical pumping on the electron spin, which provides a bidirectional pump for dynamic nuclear polarization (DNP). EIT spectroscopy can thus follow DNP both during build-up and its relaxation, and we characterize how such EIT probing can be tuned between a drive and weakly invasive probe for nuclear spin polarization.

This chapter is based on Ref. 4 on p. 127.

## 4.1 Introduction

Localized electrons in semiconductors have received attention in recent years for the possibility of preparation, manipulation and detection of the electron-spin state. Examples of these systems are quantum dots [1, 2, 3, 4], rare earth doped crystals [5, 6], color centers [7] and donors in semiconductors [8, 9, 10]. A common challenge in these systems is to control their interaction with the crystal in which they are embedded. Of particular interest is counteracting the coupling to thermally fluctuating variables of the environment, which generally is detrimental to the electron-spin coherence. In the group III-V semiconductors, the nuclei possess non-zero spin, whose fluctuating polarization interacts with the localized electron spin via hyperfine interaction [11, 12, 13, 14, 15]. This results in the lowered value of the spin dephasing time, $T_2^*$. With emerging research showing the possibility to enhance $T_2^*$ by controlling the nuclei, it is important to be able to measure this nuclear-spin environment and exert control over it.

Here we present measurements on the nuclear spin environment of donor-bound electrons ($D^0$) in gallium arsenide (GaAs) using the all-optical technique of electromagnetically induced transparency (EIT). We show how EIT can be used to precisely measure the effect of a polarized nuclear spin environment on the donor-bound electrons. Further, we explore how the EIT-control lasers themselves can play a role for controlling the nuclear spin environment via dynamic nuclear polarization (DNP), which is relevant for making EIT an effect that can improve itself by suppression of the detrimental influence of disordered nuclear spin orientations [16]. Quantitative measurements of the invasive behavior of EIT driving and interplay with DNP are presented. An advantage of this method, over nuclear magnetic resonance, is that it probes nuclear spin polarization locally at the position of the $D^0$ wave function.

## 4.2 Material

We use $n$-doped GaAs with a silicon doping concentration of $\sim 3 \times 10^{13}\,\mathrm{cm}^{-3}$. At 4.2 K, the $D^0$ electrons are localized around the silicon atoms. The $D^0$ electron wave functions have a hydrogenic energy spectrum, thus forming a solid-state analog of an alkali atom inside the crystal. With an effective Bohr radius of 10 Å they are well separated from each other at the mentioned concentration, forming a homogeneous ensemble localized electrons. These systems have an optically excited state, the neutral donor-bound exciton ($D^0$X), consisting of two electrons

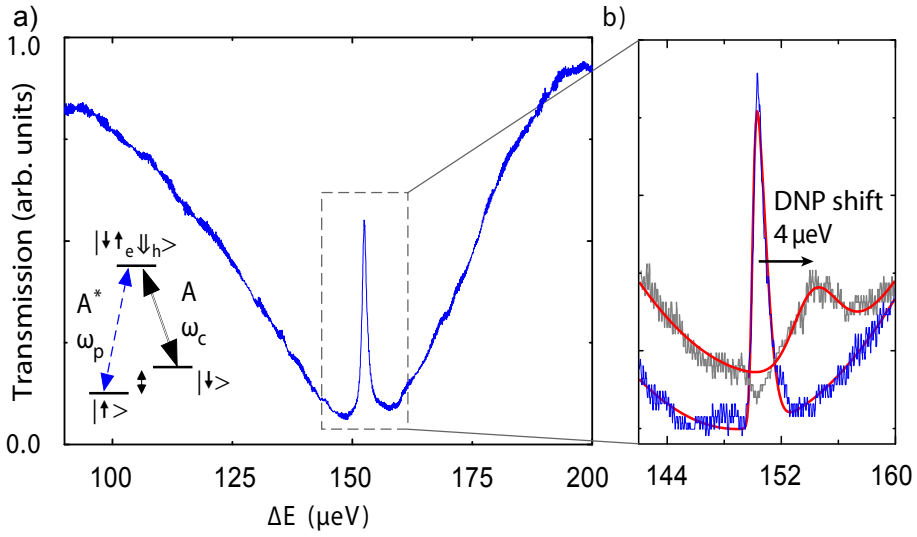


**Figure 4.1:** **(a)** Electromagnetically induced transparency (EIT), observed as a narrow peak in the transmission spectrum from a two-laser experiment on an ensemble of the donor-bound electrons in $n$-GaAs. The ensemble is addressed in a $\Lambda$-configuration (see inset), using the two Zeeman-split levels of the donor electrons and the lowest optically-active level of the donor-bound exciton complex. The control laser is fixed at the $A$-transition while a probe laser scans across the $A^*$-transition, the photon-energy difference, $\Delta E$, between the lasers is along the horizontal axis. Intensities are $3.7\,\mathrm{W\,cm^{-2}}$ and $0.18\,\mathrm{W\,cm^{-2}}$ for control and probe respectively. **(b)** Magnified view of the central part of the spectrum in (a), showing the EIT peak before (blue) and after (gray) inducing nuclear spin polarization. The EIT peak in the gray trace (arrow) shows a shift and is broadened. Red lines are Gaussian fits to the data (see main text for details) yielding peak positions of $(150.47 \pm 0.01)\,\mu\mathrm{eV}$ and $(154.47 \pm 0.05)\,\mu\mathrm{eV}$ respectively

and a hole bound to the donor. To perform EIT experiments it is required to have a three-level system. This is achieved by applying a 6.5 T magnetic field from a superconducting coil to lift the spin degeneracy in the $D^0$ and the $D^0$X. The Zeeman split $D^0$-spin states and lowest energy $D^0$X-state (of levels that can be easily observed) form a three level $\Lambda-$system as shown in the inset of the Fig. 4.1(a), where the $D^0$X-state is denoted as $|\uparrow\downarrow_e\Downarrow_h\rangle$. Following Refs. [17, 9] we denote the optical transition from $|\downarrow\rangle$ by $A$ and from $|\uparrow\rangle$ by $A^*$.

## 4.3 Spectroscopy method

For our experiments we use the setup as described in Ref. [18] where two laser beams co-propagate through the sample and are collected immediately behind the sample on a photodiode. The spot diameter of both lasers at the sample is approximately 10 µm. One of the laser beams is modulated by a chopper at 6 kHz and we isolate the modulated part of the total transmission signal by lock-in detection (for details see [19]). Measurements are performed in Voigt geometry (laser propagation perpendicular to magnetic field direction) such that the $A$- and $A^*$-transitions couple to V- and H-polarized light respectively. To perform EIT measurements one laser is kept resonant (denoted as the control laser) and the frequency dependent transmission is recorded while scanning the other laser (denoted as probe laser) over the other transition. The 55 µeV broad (FWHM) absorption dip is observed in Fig. 4.1(a) with a sharp, 1 µeV wide, enhanced transmission window inside it due to destructive quantum interference. This EIT resonance appears exactly at the two-photon Raman resonance condition where the energy difference between the laser photons equals the electron spin splitting [20, 21].

## 4.4 Dynamic nuclear spin polarization by optical excitation

The nuclear spins at the $D^0$ centers can be polarized in a process known as dynamic nuclear polarization (DNP). This is an indirect method where first the electron spin is brought out of thermal equilibrium, which can be done by optical pumping techniques. Subsequently, angular momentum gets transferred to the nuclear spins in the environment through hyperfine interaction [15], creating a net spin polarization of the nuclei. The hyperfine coupling to (partially) spin polarized nuclei induces an effective magnetic (Overhauser) field felt by the electron spin, causing a change in the electron spin splitting. Here we use resonant optical excitation of either one of the Λ-system transitions to drive the DNP process. After such optical pumping the resulting Overhauser field causes a shift in the EIT peak position. This shift is shown in Fig. 4.1(b). A change in line shape is also apparent, this originates in the fact that we observe an ensemble of $D^0$ systems with a slight spread in spin splitting. The width of the EIT peak relates to this spread and results in the $T_2^*$ of approximately 3 ns for the equilibrium case (blue line) [9, 10]. In the next section we comment on how this inhomogeneity is

reflected in the transmission signal.

## 4.5 Relation between EIT line shape and Overhauser field

The line shape of the EIT resonance contains information on the spin polarization of the nuclei near the donors. In two-laser spectroscopy the measured transmission of each of the lasers through the GaAs sample is determined by the amplitude transfer function $T(\omega_i, \Omega_i|\omega_j, \Omega_j) = \exp\left(i\omega_i nd/c\chi(\omega_i, \Omega_i|\omega_j, \Omega_j)/2\right)$, where $d$ is the thickness of the medium, $n$ is the refractive index of GaAs and $c$ is the speed of light, $i, j \in 1, 2$ with $i \neq j$ labels the laser frequencies $\omega$ and intensities expressed as Rabi frequency $\Omega$, as also introduced in Fig. 4.2. The notation of separating the variables in $T$ and $\chi$ by a vertical line is meant to indicate that we consider the transfer function with variables $\omega_i$, $\Omega_i$ conditional on $\omega_j$, $\Omega_j$ which then assume the role of parameters. The susceptibility $\chi$ is obtained by considering the polarization density of a medium filled with donors with concentration $\rho$, each represented as a $\Lambda$-system as described in Fig. 4.2. The dependence of the transmittance on the decay and dephasing parameters of the $\Lambda$-system is implicit.

The susceptibility is made up from the polarizabilities of individual systems $\beta$ which can, and generally will, show small differences, thus forming an inhomogeneous ensemble. We focus on the inhomogeneity arising from the nuclear spin polarization. This inhomogeneity gives rise to a distribution of Overhauser shifts $P(\delta)$. Here the value of $\delta = p\delta_{\max}$ is proportional to the nuclear spin polarization $p \in [-1, 1]$, where $\delta_{\max}$ is the maximum shift set by the hyperfine interaction strength. For the donor electron in GaAs $\delta_{max} = 24.5$ GHz (obtained from the maximum Overhauser field [22] via $\delta = g\mu_B B_n/2\hbar$ with g-factor $g = -0.41$ [10]). We express the susceptibility for the medium accordingly as

$$\chi(\omega_i, \Omega_i|\omega_j, \Omega_j) = \rho \int P(\delta)\beta(\omega_i, \Omega_i|\omega_j, \Omega_j, \delta)\mathrm{d}\delta. \tag{4.1}$$

The polarizability $\beta$ exhibits an EIT resonance ($\beta$ decreases as the transmission increases). When this resonance is narrow as compared to $P(\delta)$ (such that it can be approximated by a Dirac delta function), Eq. 4.1 implies that the transmission near EIT resonance has the shape of $P(\delta)$. The approximation is valid for the ensemble of $D^0$ electrons, because their measured individual decoherence time (at least $(7 \pm 3)$ µs [23]) implies a very narrow (sub MHz) EIT feature. This

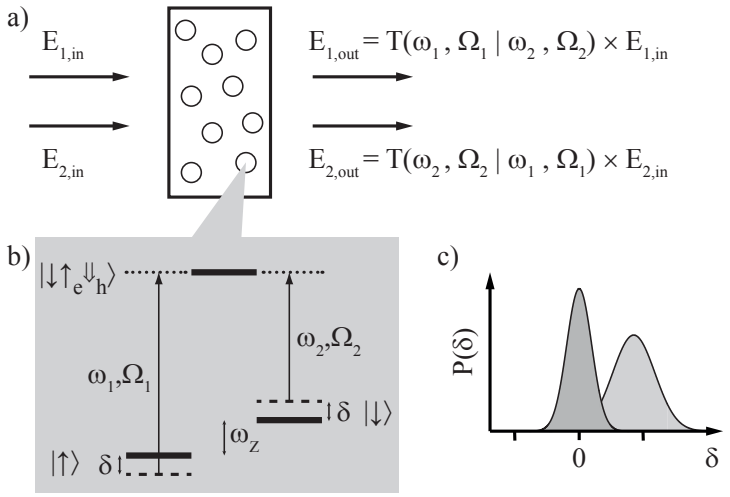


**Figure 4.2:** Transmission through a medium containing inhomogeneous Λ-systems. **(a)** The transmission of each of the two laser fields is determined by an amplitude transfer function, $T$, which is conditional on the intensity and frequency of the other laser when the lasers are both close to resonance with the transitions of a Λ-system. $T$ follows from the susceptibility, which is an effective description of the medium and is in turn derived from the polarizabilities of the individual Λ-systems. One of these is depicted in **(b)**. Nonzero nuclear spin polarization causes a shifting of the electron-spin states by $\pm\delta$. This changes the two-photon resonance condition. **(c)** The inhomogeneity in nuclear spin polarization is introduced through having $\delta$ governed by a probability distribution $P(\delta)$. Dynamic nuclear polarization can change the position and shape of the initial $P(\delta)$ (dark gray), such that the mean shifts away from zero (*e.g.* light gray area).

property is used to extract the average Overhauser field by fitting the data as shown in Fig. 4.1(b). A second order polynomial is used to fit the background (areas left and right of the peak) and a skew-Gaussian fit is used for the EIT resonance. The fitted curves are shown as red lines in Fig. 4.1(b), with peak positions at $(150.47 \pm 0.01)\,\mu$eV for the case where the nuclear spins are at thermal equilibrium (blue data) and $(154.47 \pm 0.05)\,\mu$eV for the case after DNP pumping (grey data). The error bounds indicate the 95 % confidence interval of the least-squares Gaussian fit. In following figures we take the peak positions of such fits to extract the average Overhauser field, *i.e.* $(4.00 \pm 0.05)\,\mu$eV for the case shown in Fig. 4.1(b).

From the fits to the blue and gray traces it is apparent that this EIT-based measurement is very accurate for extraction of the average spin splitting of the

$D^0$ electrons. The error of approximately one part in ten thousand is comparable to spin-noise measurements on similar samples [24]. For the case after optical pumping a broadening of the resonance is visible, resulting in a larger error bound for the fit. We attribute this to the fact that the pump induced DNP is intensity dependent, and the intensity of the laser field throughout the sample is not uniform because of the (radial) Gaussian spot and (longitudinal) Fabry-Pérot interference (see also our discussion on this in [16, 25]). Nevertheless it is possible to determine the average Overhauser field with high accuracy since the measured EIT spectrums directly reflect $P(\delta)$ (see above). In the following sections we use this method to investigate the build-up and decay of DNP in time.

## 4.6 Build-up of nuclear spin polarization

By taking EIT measurements during optical pumping of the electron spin we measure the build-up time of DNP. In this case the control laser, which is at higher intensity, causes the optical pumping leading to DNP (and we refer to it as the pump laser in this context). The experimental protocol to induce and simultaneously detect the DNP is shown in the inset of Fig. 4.3(b): After having the sample in the dark for tens of minutes (fully relaxing the DNP effects) the pump laser is switched on at $t = 0$, at an intensity of $6\,\mathrm{W\,cm^{-2}}$. While the weak probe laser is repeatedly scanned to take EIT spectra, the pump laser fulfills the role of the control laser required to make the EIT resonance visible. The pump is optically exciting the $A^*$-transition and spectra are recorded with a probe laser of intensity $0.1\,\mathrm{W\,cm^{-2}}$ by scanning across the $A$-transition. The transmission spectra, Fig. 4.3(a), show how the position of the EIT resonance changes as a function of time. The spectra are plotted on top of each other with an offset along the vertical axis for clarity. The time difference between two consecutive spectra is 65 s, which is the duration of a single scan. The shift in the peak position indicates a change in the electron spin splitting. Since this is observed at a constant external magnetic field it means the control laser acts as a pump to induce DNP in $n$-GaAs at the donor sites. The peak positions are extracted from Fig. 4.3(a) and plotted as a function of time in Fig. 4.3(b). This shows the build-up of the Overhauser field with a time constant $\tau_{\mathrm{build}} \approx 340\,\mathrm{s}$, obtained by a least squares fit to the exponential association function $\Delta E = \Delta E_{max}(1-\exp(-t/\tau_{\mathrm{build}}))$. This way of monitoring the Overhauser field during its build-up can be used to study the evolution of the nuclear field and its time scale.

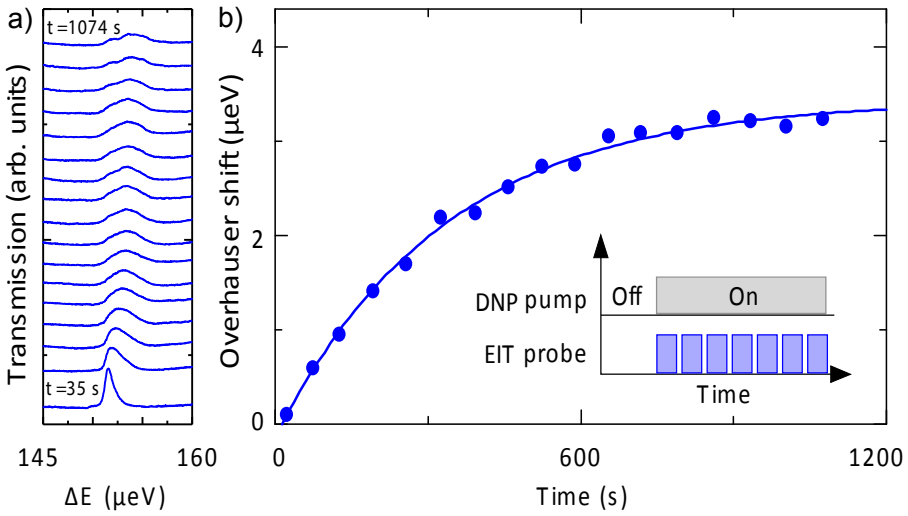


**Figure 4.3:** **(a)** The effect of optical pumping on the EIT peak shape and position (traces offset for clarity), in an experiment where a strong laser ( $6\,\mathrm{W\,cm^{-2}}$) drives the $A^*$-transition, acting simultaneously as pump laser for DNP and control laser for EIT probing. A weak probe laser ($0.1\,\mathrm{W\,cm^{-2}}$) periodically scans the $A$-transition (see time labels). Time $t = 0$ is defined as the moment where the pump laser is switched on after the sample has been in the dark (see inset of (b)). **(b)** The Overhauser shift as derived from the data in (a) as a function of time (dots). The solid line is a fit for exponential build-up, with a time constant $\tau_{\mathrm{build}} = 340\,\mathrm{s}$.

## 4.7 Decay of nuclear spin polarization and bi-directionality of DNP

Detection of nuclear polarization by EIT can also be used to monitor decay of nuclear spin polarization after it first has been induced by optical pumping. The experimental protocol is explained in the Fig. 4.4(c) inset where, in a first step, the pump laser excites one transition of the $\Lambda-$system at intensity $6\,\mathrm{W\,cm^{-2}}$ for 30 minutes to induce DNP. Then, in a second phase, the probe and control laser are used to perform EIT measurements, with the control laser addressing the $A$-transition. This experiment is performed in two distinct ways, one by optical pumping on the $A^*$-transition (Fig. 4.4(a)) and another by optical pumping on the $A$-transition (Fig. 4.4(b)), as indicated by the displayed energy level schematics.

After optical pumping on the $A^*$-transition, subsequent EIT measurements are collected with the control and probe laser intensity of $2.37\,\mathrm{W\,cm^{-2}}$ and $0.1\,\mathrm{W\,cm^{-2}}$ respectively. The first spectrum in the Fig. 4.4(a) shows the EIT

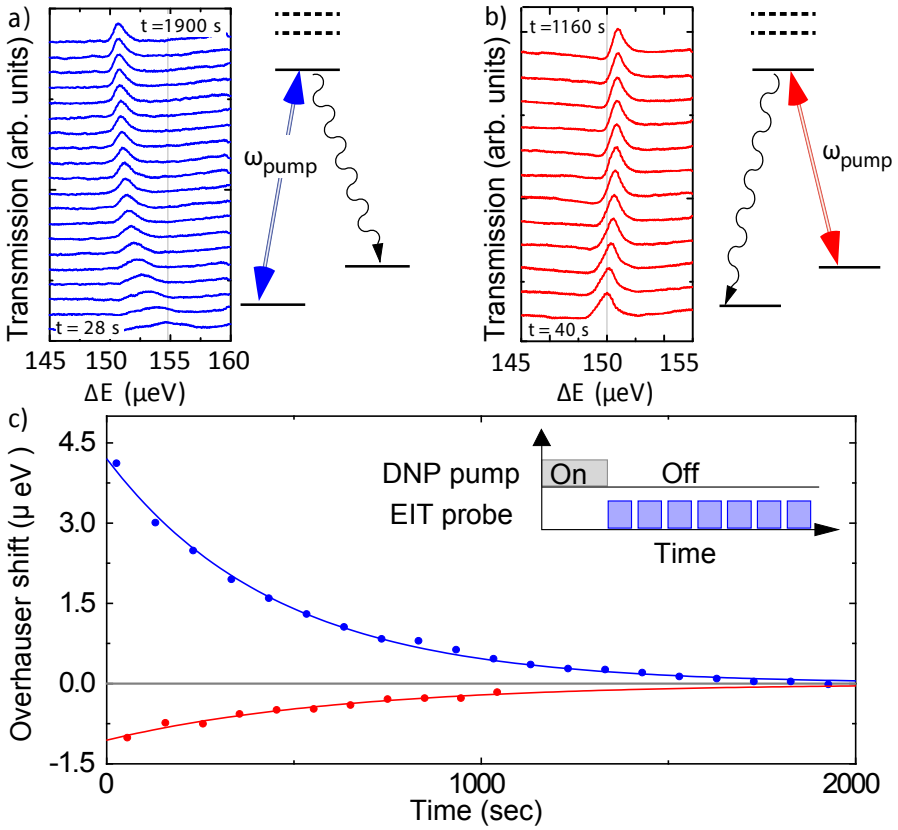


**Figure 4.4:** Bi-directionality and decay times of the induced Overhauser shift. **(a)** Evolution of the EIT peak shape and position after a single laser ($6\,\mathrm{W\,cm^{-2}}$) has been driving the $A^*$-transition for 30 min for inducing DNP (traces offset for clarity). Time $t = 0$ is defined as the moment where the DNP driving is stopped, and EIT probing starts with the control ($2.37\,\mathrm{W\,cm^{-2}}$) on the $A$-transition and scanning probe ($0.109\,\mathrm{W\,cm^{-2}}$) on the $A^*$-transition (see inset of (c)). **(b)** Similar to (a), EIT data taken after pumping the $A$-transition ($6\,\mathrm{W\,cm^{-2}}$) for 30 min. The EIT probing is realized in the similar manner as for (a) by keeping control to probe ratio the same. **(c)** The Overhauser shift as derived from the data in (a) and (b) as a function of time (dots). The solid lines are fits for exponential decay, with time constants $\tau_\mathrm{d}$ of 600 s (after pumping $A$-transition) and 480 s (after pumping $A^*$-transition).

peak shifted to higher energy as compared to its equilibrium position in the last (upper) trace. The time difference between two consecutive spectra is 93 s, which is the time required to collect one scan. The sequence shows the evolution of the EIT peak position and shape towards equilibrium. It shows that the nuclei become polarized in the direction of the applied magnetic field when the $A^*$-transition is pumped, because spin splitting is enhanced. This implies the optical pumping creates an Overhauser field along the applied magnetic field.

For the measurement in Fig. 4.4(b), the pump laser was resonant with the $A$-transition. The same EIT measurement protocol is followed as for Fig. 4.4(a). The control and the probe intensity are $4.7\,\mathrm{W\,cm^{-2}}$ and $0.2\,\mathrm{W\,cm^{-2}}$ respectively during the EIT measurements. These spectra are plotted in the same manner as in Fig. 4.4(a). The time difference between recording two consecutive spectra is 93 s. In this sequence, the first EIT peak at time $t = 40$ s appeared at lower energy as compared to the Zeeman energy at the applied magnetic field. It shows that the Overhauser field opposes the applied magnetic field when the $A$-transition is pumped.

In Fig. 4.4(c) the peak positions from Fig. 4.4(a) and Fig. 4.4(b) are plotted as a function of time exhibiting exponential decay curves that can be fitted with time constants of 600 s and 480 s. The intensity of the pump laser was equal for acquisition of both data sets. It shows that the DNP can be induced in either parallel or antiparallel to the external magnetic field, depending on the transition the pump addresses. This is consistent with the effect of DNP originating from an induced out-of-equilibrium spin polarization of the electron. The magnitude of the induced Overhauser shifts and their decay times are not symmetric. For the induced Overhauser field we attribute this to the fact that the electron spin population at thermal equilibrium is $n_\uparrow/n_\downarrow = \exp(g\mu_B B/kT)$ (Boltzmann factor), which at 4.2 K and 6.4 T implies that approximately 60 % of the population resides in the ground state. Hence, a greater difference (with respect to thermal equilibrium) in spin population can be created by pumping the $A^*$-transition than by pumping the $A$-transition. The observed relaxation of the nuclear spin polarization at the $D^0$ electrons can be ascribed to diffusion of nuclear spin polarization away from the donor site [22], that it is different for the different directions of Overhauser field is a peculiar observation. However, it should be taken into account that when taking EIT scan with the control laser on the $A$-transition, the electron spin is polarized in the same way as for the optical pumping performed before acquiring the data in Fig. 4.4 b. Hence, the EIT scans themselves induce DNP, making the decay appear slower. This invasiveness of EIT is analyzed in

the next section.

## 4.8 Invasive character of EIT as a probe

Optical excitation of the transitions of the lambda systems cause nuclear spin polarization. This implies that it is possible to disturb the nuclear spin environment during EIT measurements.To investigate the invasive behavior of EIT measurements the control laser (with intensity $2.16\,\mathrm{W\,cm^{-2}}$) is kept in resonance with $A$-transition and a transmission measurement is performed using the probe with intensity $0.216\,\mathrm{W\,cm^{-2}}$ across the $A^*$-transition. The recorded transmission spectrum is shown as the red line in Fig. 4.5(a). When the control is instead resonant with the $A^*$-transition (at $1.65\,\mathrm{W\,cm^{-2}}$) a transmission measurement is recorded using the probe with $0.093\,\mathrm{W\,cm^{-2}}$ scanning across the $A$-transition (blue line in Fig. 4.5(a)). The EIT resonances ar located at 150.87 µeV (red) and 151.66 µeV. The difference of 0.79 µeV in the EIT peak positions implies that the electron spin splitting is influenced by the sign of the electron spin polarization during EIT scans.

Since the EIT probing causes unwanted nuclear spin polarization, we quantify its effects by measuring the decay times of the nuclear spin polarization in the dark as well as illuminated. DNP is induced in the same way as for Fig. 4a. The EIT peak position is plotted as a function of time, shown in Fig. 4.5(b) (black circles). This result is compared with the situation where the system is kept in the dark. To achieve this, optical pumping is performed for 30 minutes, followed first by EIT measurement immediately after. After this initial EIT measurement the system is kept in the dark by blocking all the lasers. Then another EIT measurement is performed after an elapsed time (indicated on the horizontal axis Fig. 4.5(b)). The EIT peak positions are plotted as a function of time as the grey data triangles in Fig. 4.5(b). For this data set the decay takes place almost entirely in the dark and we expect the invasiveness of the EIT measurement to be minimized. Exponential fit to the black data points gives decay time constant of 600 s and exponential fit to the grey data points gives decay time constant of 260 s, the latter is indeed faster as expected.

To be able to monitor the decay of nuclear spin polarization by more closely, it is required to eliminate the effect that an out-of-equilibrium spin polarization during the EIT scan induces DNP itself. To counter this, ideally, the intensities of control and probe laser should be tuned such that the spin polarization during the scan equals the equilibrium spin polarization. We show how this situation can

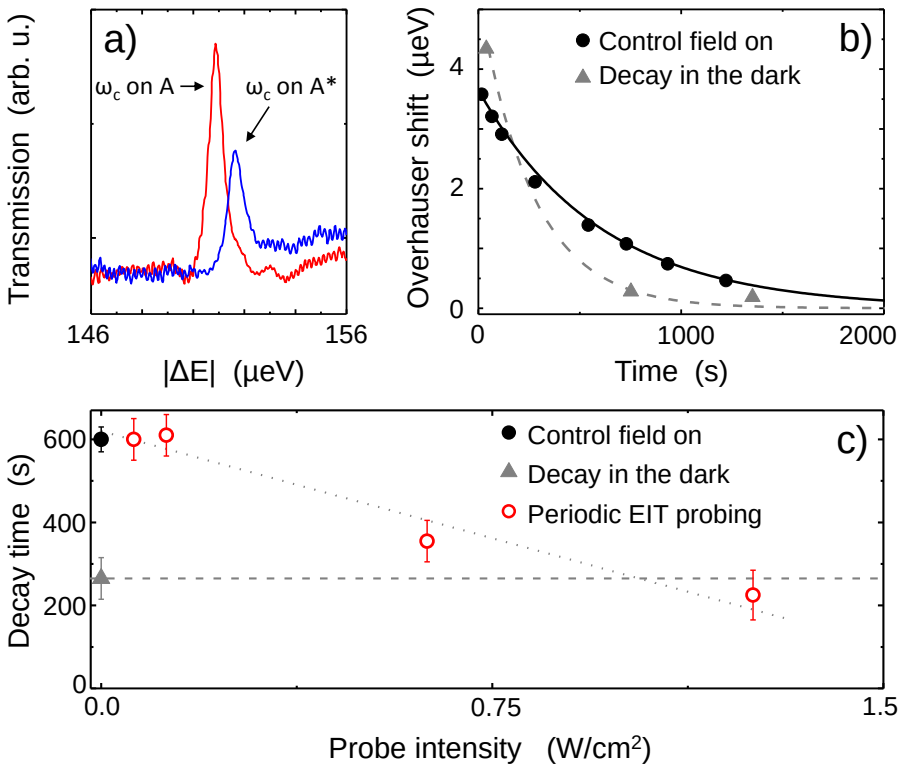


**Figure 4.5: (a)** Studies of the invasive character of EIT as a probe. (a) The difference in EIT peak position for the control (photon energy $\hbar\omega_c$) on the $A$- and $A^*$-transition, taken with similar intensities for the control ($2\,\mathrm{W\,cm^{-2}}$) in the two cases, and weaker probe lasers (see main text). **(b)** Decaying Overhauser shifts, derived from EIT scans taken after pumping the $A^*$-transition ($6\,\mathrm{W\,cm^{-2}}$) (dots). The decay with the sample in the dark between initial and subsequent EIT probing goes faster than decay with an EIT control laser continuously on the $A$-transition (EIT probing in both cases with control on $A$. Lines are fits for exponential decay, yielding time constants of 280 s (in dark) and 600 s (control on). **(c)** Time constants from exponential-decay fits for the data of (b), and similar data from periodic EIT probing with a control of $6\,\mathrm{W\,cm^{-2}}$ on $A$- and a probe of varying intensity (see horizontal axis) scanning over the $A^*$-transition (dashed/dotted lines are a guide to the eye).

be approached empirically by varying the intensities of the optical fields for the EIT measurements. The measurement protocol of Fig. 4.5(b) is repeated. And, while all other factors remain constant, the intensity of the probe laser is varied from $0.06\,\mathrm{W\,cm^{-2}}$ to $1.5\,\mathrm{W\,cm^{-2}}$. The resulting decay times are represented by red data points (black and grey data points correspond to panel (a)). It is observed that the relaxation time as the ratio of the probe to control intensity is approximately one, is identical to the relaxation time when system is kept in the dark in between the measurements. In this regime EIT can be treated as a weakly invasive tool to probe the nuclear dynamics. An alternative approach to this problem where both control and probe intensities are lowered to be incapable of inducing DNP is not possible. This is because to observe EIT it is required that the control laser coupling has a Rabi frequency exceeding the excited state decay time.

## 4.9 Conclusion

To be able to create internal magnetic Overhauser fields in a material is useful for spintronics applications. Monitoring the dynamics of nuclear spin polarization associated with this gives valuable insight in the electron-nuclear spin dynamics. The all-optical method presented here can be used as a weakly invasive method to locally probe these fields. It compares in accuracy with other all optical techniques, such as the recently demonstrated measurement of Overhauser fields by spin noise measurement [26]. An important advantage is that the technique used in our work, using two CW lasers in EIT configuration, already fulfills the requirements for techniques of light storage on spin states [27, 28, 29] and coherent control of electron spin states [30] which are important precursors for achieving quantum information applications with spins and photons.

## Acknowledgements

We thank B. H. J. Wolfs and R. S. Lous for help and valuable discussions. Further, we acknowledge the Dutch Foundation for Fundamental Research on Matter (FOM), the Netherlands Organization for Scientific Research (NWO), and the German programs DFG-SFB 491 and BMBF-nanoQUIT for funding.

# References

[1] S. W. Brown, T. A. Kennedy, and D. Gammon, *Optical NMR from single quantum dots*, Solid State Nucl. Magn. Reson. **11**, 49 (1998).

[2] J. R. Petta, A. C. Johnson, J. M. Taylor, E. A. Laird, A. Yacoby, M. D. Lukin, C. M. Marcus, M. P. Hanson, and A. C. Gossard, *Coherent Manipulation of Coupled Electron Spins in Semiconductor Quantum Dots*, Science **309**, 2180 (2005).

[3] A. Greilich, R. Oulton, E. A. Zhukov, I. A. Yugova, D. R. Yakovlev, M. Bayer, A. Shabaev, Al. L. Efros, I. A. Merkulov, V. Stavarache, D. Reuter, and A. D. Wieck, *Optical Control of Spin Coherence in Singly Charged (In,Ga)As/GaAs Quantum Dots*, Phys. Rev. Lett. **96**, 227401 (2006).

[4] X. Xu, Y. Wu, B. Sun, Q. Huang, J. Cheng, D. G. Steel, A. S. Bracker, D. Gammon, C. Emary, and L. J. Sham, *Fast Spin State Initialization in a Singly Charged InAs-GaAs Quantum Dot by Optical Cooling*, Phys. Rev. Lett. **99**, 97401 (2007).

[5] J. J. Longdell, E. Fraval, M. J. Sellars, and N. B. Manson, *Stopped Light with Storage Times Greater than One Second Using Electromagnetically Induced Transparency in a Solid.*, Phys. Rev. Lett. **95**, 063601 (2005).

[6] Georg Heinze, Christian Hubrich, and Thomas Halfmann, *Stopped Light and Image Storage by Electromagnetically Induced Transparency up to the Regime of One Minute*, Phys. Rev. Lett. **111**, 033601 (2013).

[7] C. Santori *et al.*, *Coherent Population Trapping of Single Spins in Diamond under Optical Excitation*, Phys. Rev. Lett. **97**, 247401 (2006).

[8] T. Wang, R. Rajapakse, and S. F. Yelin, *Electromagnetically induced transparency and slow light with n-doped GaAs*, Optics Communications **272**, 154 (2007).

[9] K.-M. Fu, C. Santori, C. Stanley, M. Holland, and Y. Yamamoto, *Coherent Population Trapping of Electron Spins in a High-Purity n-Type GaAs Semiconductor*, Phys. Rev. Lett. **95**, 187405 (2005).

[10] Maksym Sladkov, A. U. Chaubal, M. P. Bakker, A. R. Onur, D. Reuter, A. D. Wieck, and C. H. van der Wal, *Electromagnetically induced transparency with an ensemble of donor-bound electron spins in a semiconductor*, Phys. Rev. B **82**, 121308(R) (2010).

[11] A. Abragam, *The Principles of Nuclear Magnetism* (Oxford University Press, 1961).

[12] Walter D. Knight, *Nuclear Magnetic Resonance Shift in Metals*, Phys. Rev. **76**, 1259 (1949).

[13] Albert W. Overhauser, *Polarization of Nuclei in Metals*, Phys. Rev. **92**, 411 (1953).

[14] Georges Lampel, *Nuclear Dynamic Polarization by Optical Electronic Saturation and Optical Pumping in Semiconductors*, Phys. Rev. Lett. **20**, 491 (1968).

[15] Bernhard Urbaszek, Xavier Marie, Thierry Amand, Olivier Krebs, Paul Voisin, Patrick Maletinsky, Alexander Högele, and Atac Imamoglu, *Nuclear spin physics in quantum dots: An optical investigation*, Rev. Mod. Phys. **85**, 79 (2013).

[16] A. R. Onur, J. P. de Jong, D. O'Shea, D. Reuter, A. D. Wieck, and C. H. van der Wal, *Stabilizing nuclear spins around semiconductor electrons via the interplay of optical coherent population trapping and dynamic nuclear polarization*, Phys. Rev. B **93**, 161204(R) (2016).

[17] V. A. Karasyuk, D. G. S. Beckett, M. K. Nissen, A. Villemaire, T. W. Steiner, and M. L. W. Thewalt, *Fourier-transform magnetophotoluminescence spectroscopy of donor-bound excitons in GaAs*, Phys. Rev. B **49**, 16381 (1994).

[18] M. Sladkov, M. P. Bakker, A. U. Chaubal, D. Reuter, A. D. Wieck, and C. H. van der Wal, *Polarization-preserving confocal microscope for optical experiments in a dilution refrigerator with high magnetic*, Rev. Sci. Instr.**82**, 043105 (2011).

[19] J. P. de Jong, A. R. Onur, D. Reuter, A. D. Wieck, and C. H. van der Wal, *Analysis of optical differential transmission signals from co-propagating fields in a lambda system medium*, arXiv:1409.7679 (2014).

[20] K. J. Boller, A. Imamoglu, and S. E. Harris, *Observation of electromagnetically induced transparency*, Phys. Rev. Lett **66**, 2593 (1991).

[21] M. Fleischhauer, A. Imamoglu, and J.Marangos, *Electromagnetically induced transparency: Optics in coherent media.*, Rev. Mod. Phys. **77**, 633 (2005).

[22] D. Paget, G. Lampel, B. Sapoval, and V. I. Safarov, *Low field electron-nuclear spin coupling in gallium arsenide under optical pumping conditions*, Phys. Rev. B **15**, 5780 (1977).

[23] S. M. Clark, K.-M. C. Fu, Q. Zhang, T. D. Ladd, C. Stanley, and Y. Yamamoto, *Ultrafast optical spin echo for electron spins in semiconductors*, Phys. Rev. Lett. **102**, 247601 (2009).

[24] M. Oestreich, M. Römer, R. J. Haug, and D. Hägele, *Spin noise spectroscopy in GaAs*, Phys. Rev. Lett **95**, 216603 (2005).

[25] J. P. de Jong, *Optically addressing semiconductor electron-spin ensembles with tunable nuclear-spin environments* (PhD thesis, University of Groningen, 2016).

[26] I. I. Ryzhov *et al.*, *Spin noise explores local magnetic fields in a semiconductor*, Sci. Reports (NPG) **6**, 21062 (2016).

[27] C. Liu, Z. Dutton, C. H. Behroozi, and L. V. Hau, *Observation of coherent optical information storage in an atomic medium using halted light pulses*, Nature **409**, 490 (2001).

[28] D. F. Phillips, A. Fleischhauer, A. Mair, R. L. Walsworth, M. D. Lukin, *Storage of light in atomic vapor*, Phys. Rev. Lett **86**, 783 (2001).

[29] A. V. Turukhin, V. S. Sudarshanam, M. S. Shahriar, J. A. Musser, B. S. Ham, and P. R. Hemmer, *Observation of ultraslow and stored light pulses in a solid*, Phys. Rev. Lett **88**, 023602 (2001).

[30] C. G. Yale, B. B. Buckley, D. J. Christle, G. Burkard, F. J. Heremans, L. C. Bassett, and D. D. Awschalom, *All-optical control of a solid-state spin using coherent dark states*, Proc. Nat. Ac. Sc. **110**, 7595 (2013)

# Chapter 5

# Polarization-preserving confocal microscope for optical experiments in a dilution refrigerator with high magnetic field

**Abstract**

We present the design and operation of a fiber-based cryogenic confocal microscope. It is designed as a compact cold-finger that fits inside the bore of a superconducting magnet, and which is a modular unit that can be easily swapped between use in a dilution refrigerator and other cryostats. We aimed at application in quantum optical experiments with electron spins in semiconductors and the design has been optimized for driving with, and detection of optical fields with well-defined polarizations. This was implemented with optical access via a polarization maintaining fiber together with Voigt geometry at the cold finger, which circumvents Faraday rotations in the optical components in high magnetic fields. Our unit is versatile for use in experiments that measure photoluminescence, reflection, or transmission, as we demonstrate with a quantum optical experiment with an ensemble of donor-bound electrons in a thin GaAs film.

This chapter is based on Ref. 3 on p. 127.

## 5.1 Introduction

Fundamental research on quantum coherence in solid state is currently strongly driven by the goal to implement quantum information tasks [1, 2, 3]. Electron and hole spins in semiconductors are here of special interest since these material systems give access to realizing compact devices where quantum correlations between coherence of spins and optical signal fields can be established. However, optical manipulation and detection of spins is a challenging task since experiments demand a combination of conflicting requirements such as cryogenic temperatures, high optical intensities, high magnetic fields, and precise control of the optical polarizations.

In recent years research in this direction nevertheless developed into a very active field that showed many impressive results, in particular with localized spins in quantum dots or spins bound to donor sites [4, 5, 6, 7, 8, 9, 10, 11, 12]. Most of these experiments were carried out at temperatures of a few Kelvin. Lower temperatures were till now typically not useful since spin states can be prepared via optical pumping, and the coherence of localized spins is in all III-V and most II-VI semiconductors limited by hyperfine coupling to fluctuating nuclear spins. We anticipate, however, that dephasing by nuclear spins can be removed with controlled dynamical nuclear polarization effects [10, 12] or with spin echo techniques [13]. If such techniques are fully exploited, optical experiments at milliKelvin temperatures become of interest, since freezing out the phonons at energies of the Zeeman splitting of electron or hole spins will be important for exploring the ultimate limit of controlling spin coherence in solid state. We report here the design and operation of a fiber-based confocal microscope in a dilution refrigerator that is suited for this research. This instrument also has relevance for related quantum optical studies with spin coherence of quantum Hall states [14, 15], or optical studies of the Kondo effect [16, 17, 18].

When designing optical experiments in a dilution refrigerator one has to deal with a number of restrictions. (*i*) The sample space is typically inside a series of heat shields that forbid free-space optical access to the sample. The sample volume can be reached with optical fibers, but this requires a method to couple light from the fiber to the sample. (*ii*) The limited sample volume requires compact solutions which can withstand cryogenic temperatures and high magnetic fields. (*iii*) Using high optical intensities is in conflict with the need to maintain low power dissipation. High intensity at low optical power can obviously be realized with tight focussing, but this requires a microscope with good performance in

the sample volume. (*iv*) If the experiments require well-defined polarizations, one needs to deal with the fact that in high fields most optical components will cause a substantial Faraday rotation of the polarization.

To address all these constraints we build on an earlier design of a fiber-based confocal microscope for use at 4.2 Kelvin [19, 20]. Our key innovations are that we circumvent Faraday rotations by using a polarization maintaining fiber and by using a compact cryogenic microscope with all propagation through free-space elements in a direction that is orthogonal to the magnetic field. In addition, we make the approach suited for application at milliKelvin temperatures and we report how we deal with stronger constraints for the heat load from various functions, as for example the wiring to piezo motors that drive the microscope focussing.

We demonstrate application of the microscope on an ensemble of donor-bound electrons in a thin GaAs film. We performed optical spectroscopy of spin-selective transitions of the donor-bound electron states to donor-bound trion states, both via photoluminescence and in direct transmission experiments. We also directly demonstrate a quantum optical effect, known as electromagnetically induced transparency, with this material system.

## 5.2 Microscope design and operation

### 5.2.1 Modular compact microscope unit

We designed the confocal microscope as a compact cold-finger that fits inside the bore of a superconducting magnet, and which is a modular unit that can be easily swapped between use in a dilution refrigerator (Leiden Cryogenics DRS1000) and a helium bath cryostat. Both systems are equipped with a superconducting magnet (Cryogenics Ltd.), with a bore that yields a cylindrical sample space of 60 mm diameter (for the dilution refrigerator this concerns a 78 mm bore with a series of heat shields around the sample volume). In both cryostats the magnetic field is applied along the vertical direction (defined as $z$-direction).

### 5.2.2 Polarization maintaining fiber

For delivering light into the sample volume we use a single-mode polarization-maintaining PANDA-type fiber [21] (PMF) with $NA = 0.13$. Its mode-field diameter is 5 $\mu$m and the cut-off wavelength is 700 nm. Operation of the PMF

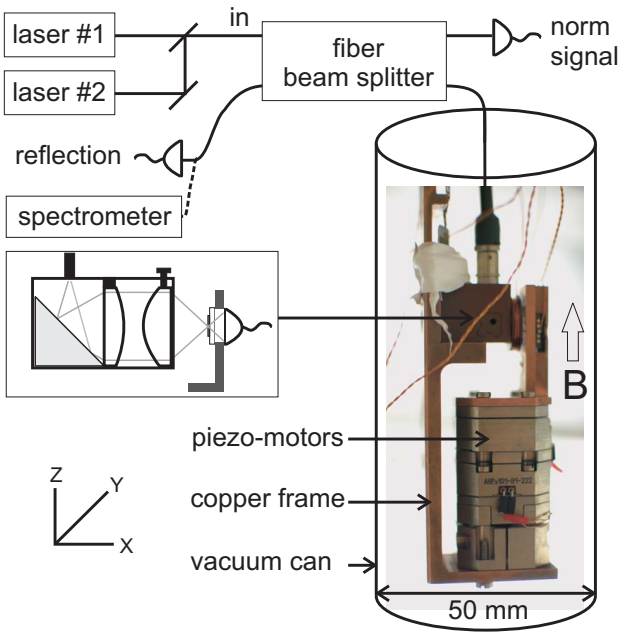


**Figure 5.1:** (color online) Schematics of the experimental setup. Excitation light of two tunable lasers is coupled into a polarization-preserving fiber-based beam splitter (port IN) and one of the outputs is connected to the fiber that runs to the microscope. This fiber delivers excitation light to the sample, which is mounted on an $xyz$-stack of piezo-motors. The sample position can be tuned to be in or out of the focal spot of the two-lens microscope. The microscope is mounted in a tube, which is vacuum pumped and immersed in a Helium bath (4.2 K) or used in a dilution refrigerator. A superconducting coil provides magnetic fields up to 9 T. A silicon *pin*-photodetector is positioned right behind the sample for detection of the optical transmission. Both the sample and the detector are mounted on a Γ-shaped sample holder. The second output of the beam splitter is coupled to a photodetector for monitoring the optical powers. Signals that come from reflection on the sample, as well as emission by the sample, retraces the optical path through the fiber. After passing the beam splitter is can be diverted to a regular photodetector, or to a spectrometer. Inset: microscope components mounted on the copper frame that forms the cold finger.

is based on built-in stress that induces a linear birefringence (different index of refraction, $n_V$ and $n_H$) for two TEM propagation modes with orthogonal linear polarizations. Linear light coupled into one of these two modes does not couple into the other mode during propagation. We apply this for delivering fields with polarization parallel (defined as V polarization) and orthogonal (defined as H polarization) to the magnetic field.

Using a PMF has the advantage that we can deliver well-defined polarizations that remain pure in the field range -9 T to +9 T. This removes the need for *in-situ* polarization analysis for calibrating and pre-compensating Faraday rotations and other effects that influence the polarizations [19]. In addition, the polarizations remain pure when the fiber is subject to stress from bending and thermal gradients, and the polarization purity is thereby also more resilient against mechanical vibrations.

To evaluate whether the PMF will indeed suppress all Faraday rotations in fields up to ±9 T we need to compare the stress induced birefringence to the Faraday effect. This can be quantified by comparing the associated beat length and rotation length, respectively. If linearly polarized light is coupled into the PMF but not along one of the TEM eigenmodes, its polarization will undergo periodic unitary transformation due to the difference between $n_V$ and $n_H$. The period of transformation is the linear birefringence length $L_{LB}$ (the smaller $L_{LB}$, the better the polarization maintaining properties of the fiber). For the fiber in use [21] $L_{LB} = 2.4$ mm. The Faraday effect occurs when an optical fiber is a subject to magnetic field along its optical axis. It then shows circular birefringence and its strength is characterized by the Verdet constant. This yields a circular birefringence rotation length $L_{CB} = 2\pi/(V \cdot B) \approx 4$ cm for a magnetic field $B = 9$ T and with the Verdet constant of the fiber [21] $V = 6$ rad $\mathrm{T^{-1}m^{-1}}$. Our fiber thus has $L_{LB} < L_{CB}$ and we therefore expect that linear polarization of light coupled into one of the fiber TEM eigenmodes will not be affected by magnetic field. We do check that this is indeed the case by using polarization selective optical transitions of donor-bound electrons as a polarization probe (further discussed in Sec. 5.3).

The single-mode nature of the PMF is useful for experiments where two co-propagating fields should drive the same system. The beam overlap for these two fields will then be ideal in the sample volume.

### 5.2.3 Confocal microscope in Voigt geometry

To focus light from the fiber in the sample volume we use a compact home-built microscope objective, based on two aspheric lenses. The approach is similar to the system used by A. Högele [19] *et al.*, but we incorporated changes that avoid circular birefringence that occurs when light propagates through lens material in high fields. This can rotate linear polarizations by several degrees in 1 mm lens material in a 9 T magnetic field [22] (typical values for the Verdet constant of materials [23, 24] as BK7 and Corning glass are 1–10 rad $\mathrm{T}^{-1}\mathrm{m}^{-1}$). Before light is collimated and focused its propagation direction is diverted $90^o$ by means of a surface mirror (dielectric prism, Thorlabs MRA05-E02) after which its $\vec{k}$-vector is orthogonal to the direction of the magnetic field and this eliminates the magnetic field induced rotation of the polarization.

Another advantage of this approach is that it gives access to optical experiments in Voigt geometry (light propagation direction orthogonal to the magnetic field direction). In this geometry, light with V polarization can drive atomic $\pi$-transitions (no change in angular momentum), and light with H polarization can drive atomic $\sigma$-transitions (a change in angular momentum of $\pm\hbar$). Thus, this yields that for the typical optical selection rules of electron spins in semiconductors, transitions that start from the electron spin-up or spin-down state can be addressed selectively with two orthogonal linear polarizations. Another advantage is that one of these two fields can be easily blocked by polarization filtering before the two co-propagating modes reach a detector (as required for several resonant-Raman control schemes [25]). Such a filter with high extinction ratio can be realized before any propagation through glass material as a metal nanowire-grid polarizer on a transparent substrate [26].

The first lens of the microscope objective collimates the light from the fiber. We use an aspheric lens (Thorlabs 350430) with focal length $f = 5.0$ mm, numerical aperture $NA = 0.15$ and clear aperture 1.5 mm. After collimating, light is focused by a second aspheric lens (Thorlabs 350140) with focal distance $f = 1.45$ mm, $NA = 0.55$ mm and clear aperture 1.6 mm. Since we do not have perfect $NA$ matching between the fiber and the collimating lens, the numerical aperture of the full objective system will be less than that of the focusing lens, resulting in $NA_{obj} = 0.45$. Using this we can estimate the theoretical value for the spot diameter to be $D_{spot} = 1.42 \cdot \lambda$.

The prism mirror and the collimating lens are firmly glued into a DuPont Vespel-SP1 housing. This material was chosen since it is dimensionally stable during cryogenic application, while it is easy to machine at room temperature.

**Figure 5.2:** Photo of a home-built heat-sink for use in cryogenic coaxial lines, with SMA connectors and a gold-plated sapphire substrate in a copper housing unit.

In addition, its slightly plastic character facilitates a safe initial placement of fragile optical components. The focusing lens is fixed inside a separate Vespel-SP1 frame and then fitted into the housing of the objective. This allows for removing the focusing lens from the objective while aligning the fiber with respect to the collimating lens (procedure discussed below). In addition, the focussing lens has a certain positioning freedom (along the propagation direction, about 1 mm). This can be used to fit in a plastic thin-film $\lambda/4$ retardation plate [27], which can be used if one wishes to transform the linear polarizations into circular polarizations.

In order to align the fiber with respect to the collimating lens, we position the fiber roughly in the right position without clamping it yet to the objective. Instead, the fiber ferrule is clamped on a translation stage, while the objective with collimating lens is firmly attached to a 3-axis kinematic mount. Light is coupled into the fiber from the other end. We use here a diode laser, operated below threshold to avoid interference effects in the fiber. The light is delivered via a fiber beam splitter to allow monitoring the intensity of light that is reflected back into the fiber. During the alignment this is used by directing the outgoing beam from the objective onto a mirror which reflects it back to the objective. The reflected beam is imaged with the help of a CCD camera (Watec WAT-120N+), which allows both a visual inspection of the quality of the collimated beam and helps directing the reflected beam back to the objective. By adjusting the position of the fiber inside the objective while tracing the back-reflected intensity together with visual inspection of the collimated beam we thus optimize a maximally collimated beam.

### 5.2.4 Focussing mechanics and wiring to the piezo motors

For positioning the sample in the focus of the objective we use a three-axes $xyz$-translation stage on the cold finger in the form of slip-stick piezo-motors (Attocube, model ANP101). This gives a travel range of 5 mm in all three directions. Both the piezo stack and the objective are fixed on a home-built copper frame (Fig. 5.1).

Applying such piezo motors in a dilution refrigerator is not straightforward since the wires to the motors should have a resistance of 5 Ω at most. In the dilution refrigerator the length of the wires exceeds a few meters, such that wires with low resistivity must be used. This, however, creates an unacceptable heat load on the mixing chamber with most types of wiring. We circumvented this problem by using coaxial lines with low DC resistance values. This works very well since the need for the low resistance values is partly driven by the need for high bandwidth for getting triangular control pulses (∼100 V) with a fast edge to the piezo-motors without much smoothing.

We implemented this by installing a set of 7 of multi-purpose coaxial lines to the mixing chamber (Micro-Coax, semi-rigid model UT 85-B-SS, 60 GHz bandwidth, stainless steel outer conductor, silver-plated BeCu inner conductor, ∼0.5 $\Omega m^{-1}$ DC resistance). These have an excellent trade-off between low electrical resistance and low thermal conductance at low temperatures. The piezo-motors use 3 of these coaxial lines.

Realizing a low heat load on the mixing chamber still requires to heat-sink the inner conductor of the coaxial lines at several stages between room temperature and base temperature. We use home-built heat sinks at 4.2 K, the 1K-pot (∼1.5 K), the still (∼600 mK), the cold plate (∼100 mK) and at the mixing chamber. The heat sinks are made with sapphire substrates in a copper housing unit (Fig. 5.2), since sapphire combines high electrical resistance with good thermal conductivity at low temperatures. We gold-plated one of the surfaces of the sapphire. The non-plated sapphire surface is then glued onto a copper plane in the housing unit with thin stycast. Two SMA connectors are then mounted on this unit, and we solder the inner conductors on opposite sides of the gold plated sapphire surface. Our units show more than sufficient bandwidth (a few MHz) for the piezo-motor application, but this can be increased by engineering the sapphire plates as microwave strip lines. After installing these coaxial lines we did not observe an effect on the cooling power of the dilution refrigerator (base temperature well below 20 mK), and we achieved driving of the piezo-motors via these coaxial lines without any problems.

### 5.2.5 Optical detection and cooling down procedure

For optical detection in transmission experiments we use a photodiode (Hamamatsu, *pin*, 5106) on the Γ-shaped copper sample holder that is mounted on the piezo-motor stack (Fig. 5.1). The sample can be mounted in front of the photodiode. The detection of signals from reflection and photoluminescence experiments is discussed below.

The use of the photodiode on the cold finger shows in practice the risk that it breaks while cooling down the system. Most likely, this is because thermal shrinking causes a crack in the plastic laminate of the diode that also breaks the semiconductor chip underneath. To avoid this, we cool down with He contact gas at a pressure which does not exceed $10^{-2}$ mbar. This enforces the system to cool very slowly (in about 6 hours). With this approach, our photodiodes survive in 9 out of 10 cases.

### 5.2.6 Focal plane positioning and spot size

Since we do not have direct free optical access to the system, it is necessary to design a procedure for positioning and focussing that rely on using the transmitted and reflected signal only. For positioning in the plane orthogonal to the optical axis, we use the trivial approach with high-contrast markers on the sample that can be detected in the transmission signal. For positioning the sample plane in the focal point of the objective (along $x$-axis), we use the fact that the output of the fiber and the objective unit together constitute a confocal microscope. We use this in a procedure with a fiber-coupled diode laser (Thorlabs LPS-785-FC) operated below the lasing threshold (incoherent light for avoiding interferences in the back-reflected signal). The light is delivered into the sample volume via the optical fiber, with a fiber-based beam splitter (OZ optics) in its path (Fig. 5.1). This allows for measuring the reflected signal while the position of the sample surface is scanned along the $x$-axis through the focus of the objective.

A typical focal plane scan is shown in Fig. 5.3(b). As expected, the reflected signal reaches a maximum when the sample plane is positioned exactly in the focus of the objective and drops smoothly while going out of focus. In contrast to the previously reported microscopes [19] we observe not a single Lorentzian reflection profile but a superposition of two Lorentzians, which indicates a small misalignment within the confocal microscope. This is most likely due to a non-uniaxial arrangement of the lenses with respect to the optical axis of the fiber that results from a small misalignment of the prism mirror. We did not correct

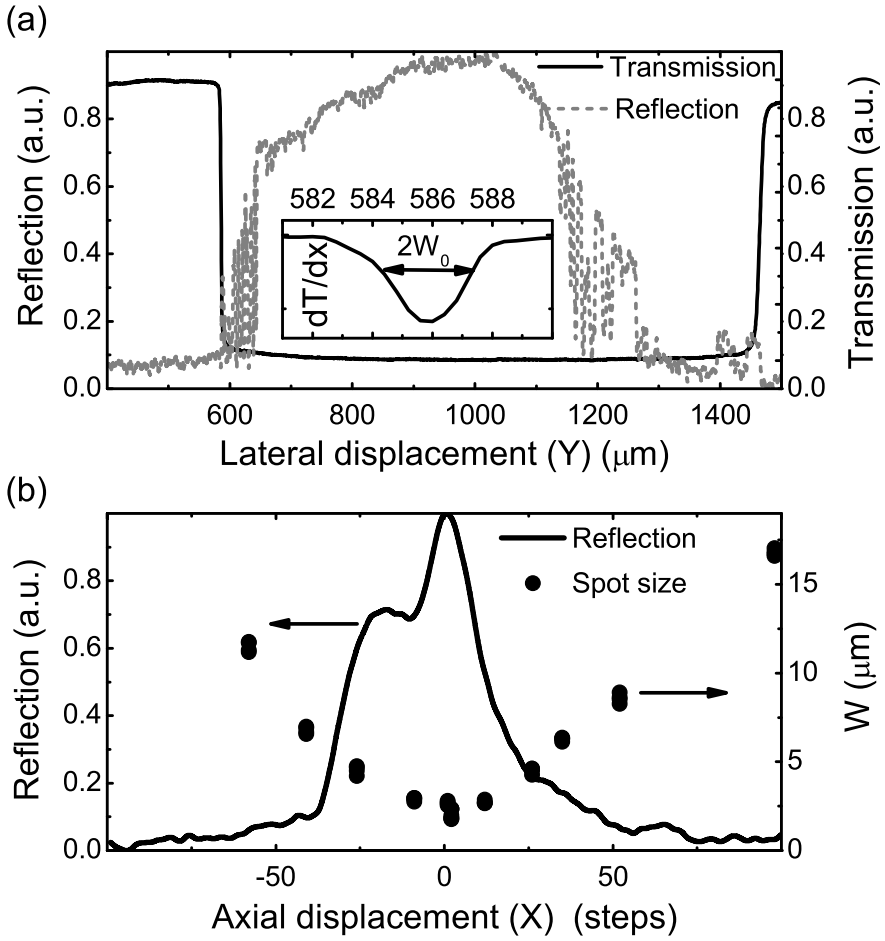


**Figure 5.3: (a)** Reflected and transmitted signal as a function of the lateral position ($y$-axis) of the sample. The spot size $W$ of the beam on the sample surface (waist $W_0$ when in focus) is determined with the knife-edge technique (inset). **(b)** Reflected signal (solid line) and the spot size $W$ (dots) as a function of the axial displacement ($x$-axis) of the sample.

this for the data presented here since we have the prism mirror firmly glued in the objective housing, and it did not compromise the experiments we present below.

To determine the spot size we use the knife-edge technique, where we fix the axial position (along the $x$-axis) of the microscope at different locations on the reflection curve (Fig. 5.3(b)) and perform a lateral scan ($y$-direction) across the sample. A typical scan, taken with the sample plane in focus, is shown in the Fig. 5.3(a). The solid black curve is the transmitted signal and the dashed gray curve is the reflected signal. As expected, a high signal level in reflection

corresponds to low signal level in transmission since we use here an $n$-GaAs sample that is opaque for the used wavelength, on a transparent substrate. Light that is reflected from the sample surface is efficiently collected back into the fiber because of the confocal geometry. The reflection profile is also influenced by the morphology of the sample surface, which is not uniform due to fabrication imperfections. It is, however, always possible to find a spot on the sample with a clean reflection profile.

Since we know the size of the sample we can calculate the lateral ($y$-axis) step size of the piezo-motors (which depends on temperature and mechanical load). From the slope of the transmission signal when scanning across a sharp edge we can determine the spot size of the beam (inset of the Fig. 5.3(a)). We define the spot size on the surface of the sample as the radius $W$ of a Gaussian beam (waist $W_0$ when in focus). The black dots in the Fig. 5.3(b) are results for $W$ after fitting the knife-edge profile with a Gaussian function.

The measured beam waist was found to be $W_0 = 2.3$ $\mu$m, which is almost four times larger than our theoretical estimate for the diffraction limited spot size. This is related to the small misalignment, since the aspheric lenses are highly optimized for realizing a small focus exactly on the optical access, and with correcting the alignment this type of objective at low temperatures can yield a spot size that is well within a factor 2 from the diffraction limit [19, 20]. The larger spot was compromising the efficiency of collecting light in our photoluminescence experiments, but it did not compromise our transmission experiments (further discussed below). In the transmission experiments we also work at least a small amount out of focus in order to eliminate interference effects that occur when working in focus. These then result from the Fabry-Pérot cavity that is formed between the sample surface and the facet of the fiber output.

## 5.3 Characterization of performance

A characterization of the focussing protocol and the spot size was already included in the previous section. In this section we focus on the polarization purity and achieving a low heat load and good heat-sinking on the cold finger.

### 5.3.1 Polarization purity

In order to characterize the polarization preserving properties of the setup we used the optical transitions of donor-bound electrons ($D^0$ system) to a donor-

bound trion state (the lowest [optically-active] level of the $D^0X$ complex) in a strong magnetic field. Our sample was a thin GaAs epilayer with Si doping at very low concentration (further discussed below). The relevant level scheme with transitions labeled $A$ and $A^*$ is presented in Fig. 5.4(a). The states $|\uparrow\rangle$ and $|\downarrow\rangle$ are the spin-up and spin-down state of the electron in the $D^0$ system, which is localized at the donor site in a Hydrogen-like $1s$ orbital. These two states are Zeeman-split by the applied magnetic field. The optical transitions $A$ and $A^*$ are to the lowest optically-active energy level of the $D^0X$ system (state $|e\rangle$, well separated from the next level $|e'\rangle$), which has two electrons in a singlet state and a spin-down hole with $m_h = -\frac{1}{2}$ localized at the donor site [13]. The optical selection rules of this system have been characterized very well [28] and show a strong polarization dependence. For the $D^0$ system, H-polarized light couples to the $A^*$ transition (with a change in angular momentum of $\hbar$) but not to the $A$ transition. In contrast, V-polarized light couples to the $A$ transition (and not to $A^*$), since this is a transition without a change in angular momentum.

For performing this test we took scanning-probe transmission spectra with tunable CW Ti:sapphire lasers (Coherent MBR-110, linewidth below 1 MHz) around the $D^0X$ resonances (Fig. 5.4(b,c)). These spectra are results of pump-assisted transmission spectroscopy. This approach is needed for avoiding bleaching of transitions due to optical pumping by the probe, and it is also useful for identifying whether spectral lines are from transitions that start from $|\uparrow\rangle$ or from $|\downarrow\rangle$. For further explanation it is best to focus on a typical result (Fig. 5.4(c)): Here, we fixed the pump laser on the frequency of the $A^*$ transition with H polarization, while we scan the probe laser frequency with V polarization and study its transmission. We then observe that the absorption of the $A$ transition is strongly enhanced by the pump (compare to absorption by $A$ in Fig. 5.4(b)). These results appear with respect to a background signal with slower modulation of the transmission that is due to a Fabry-Pérot effect in the sample (further discussed below). In these experiments we use a chopper in the probe beam and lock-in techniques for separating the detected signal from the pump and probe beam.

The strong polarization dependence of the absorption lines $A$ and $A^*$ in the transmission spectra in Fig. 5.4(b,c) demonstrates that the linear polarizations H and V are indeed well preserved in our setup. We performed such experiments with magnetic fields in the range from $B = 5$ to 9 T, and the effective polarization selectivity did not show a dependence on $B$. We analyzed that in our experiments the characterization of the polarization purity is in fact limited by the accuracy of the polarization preparation on the optical table, and the alignment of the H and

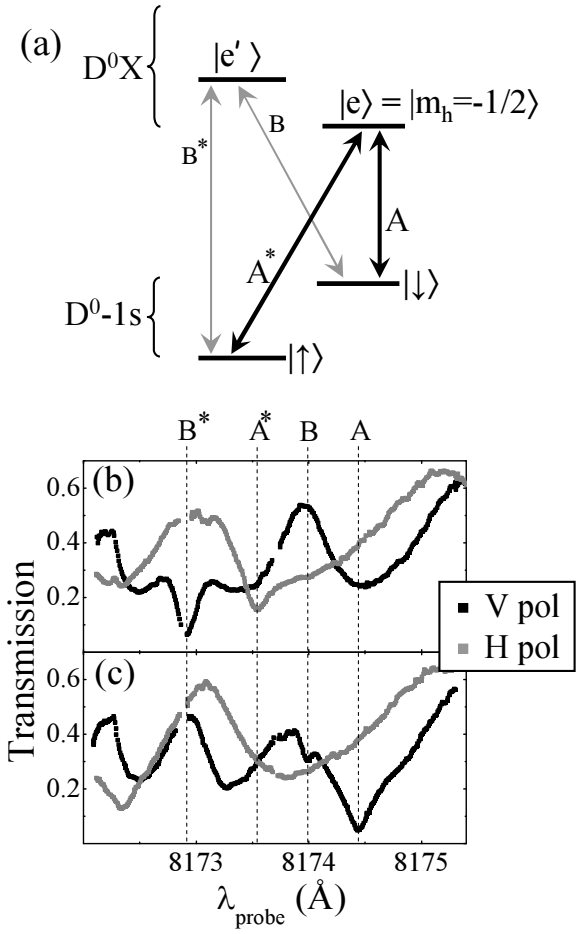


**Figure 5.4:** **(a)** Energy level diagram and optical transitions for the $D^0$-$D^0X$ system in GaAs. **(b)** Pump-assisted spectroscopy with pumping V-polarized light at the $A$ transition (at 8174.45 Å). This results in enhanced absorption for H-polarized light at the $A^*$ transition (8173.55 Å). **(c)** Complementary to the observation of (b), pumping with H-polarized light at the $A^*$ transitions results in enhanced absorption for V-polarized light at the $A$ transition. Similar cross-pumping effects are observed for the nearby $B$ and $B^*$ transitions. Data taken at $B = 8$ T.

V mode of the PMF fiber output with respect to the direction of the magnetic field. Characterizing this with all instrumentation at room temperature showed that the error from coupling light purely into one of the eigenmodes of the PMF is at the level of 1 part in 100. In our experiment this was sufficiently low, evidenced by the fact that an attempt to pump transition $A$ with H-polarized light did not induce any changes in the transmission spectrum from such pump-assisted spectroscopy.

For characterizing the polarizations we could not implement the approach of A. Högele *et al.* [19] with cryogenic polarizing beam splitters near the sample volume. Our sample space is too small, and it would also be difficult to deal with Faraday rotations in the beam splitter cube itself.

### 5.3.2 Heat load and heat-sinking of optical power

With our unit installed in the dilution refrigerator, we could cool down to milliKelvin temperatures without any problems, and running the optical experiments with typical conditions did not show excessive heating. In particular, in the next section we discuss experiments in which we drive the $A$ transition with optical Rabi frequencies $\Omega_c$ up to $2\pi \cdot 2$ GHz. We performed this with a spot size as large as 200 $\mu$m$^2$, where this driving corresponds to an optical heat load of 20 $\mu$W. This is well below the cooling power of our dilution refrigerator at 100 mK.

Obviously, the semiconductor material in the focus of the optical fields can be at a much higher temperature than the mixing chamber material. We indeed found that it is crucial to thoroughly heat-sink our $n$-GaAs epilayers. The only experiments where we could avoid this heating used $n$-GaAs epilayers that were directly attached to a sapphire substrate with binding by van der Waals forces, and a good thermal contact between the sapphire and the cold finger. These samples were prepared by first using an epitaxial lift-off technique [29] for removing the GaAs epilayers from the original GaAs wafer. This was followed by transferring the epilayer to a wedged sapphire substrate.

While we thus successfully operated this unit at sub-Kelvin temperatures, the experimental data did not show features that differed from the 4.2 K data. For the experiments on $D^0$ system that we present below, this could be expected. The optical transitions at 4.2 K show an inhomogeneous linewidth of 6 GHz, which is not expected to narrow at lower temperatures. Also, the electron spin dephasing time for the $D^0$ system is limited by hyperfine coupling to fluctuating nuclear spins, and this mechanism is temperature independent in the range 10 mK to 4.2 K. Our attempts to suppress these fluctuations via dynamical nuclear polarization (DNP) only showed a very small improvement of the dephasing time till now, since the optically induced DNP effects appeared to be very weak in our experiments [30]. For the discussion of applications of our system we therefore focus on data taken at 4.2 K.

## 5.4 Application: Spectroscopy and EIT with $n$-GaAs

In order to demonstrate the versatility of our setup we performed an optical study of the coherent properties of an ensemble of $D^0$ systems in GaAs. This system was already introduced in Sec. 5.3.1. We present here data from epitaxially grown 10 $\mu$m films of GaAs with Si doping at $n_{Si} = 3 \times 10^{13}$ cm$^{-3}$. At such low concentrations the wave function of the neighboring donors do not overlap, which yields an ensemble of non-interacting $D^0$ systems.

To study the coherent properties of such ensembles we first find the spectral position of the relevant optical transitions [31] with photoluminescence and transmission spectroscopy. We then resolve the fine spectra of the Zeeman-split levels [28] with the pump-assisted transmission spectroscopy. After identifying the $D^0$-$D^0X$ system in this manner, we could demonstrate electromagnetically induced transparency [32] (EIT) with this medium, which is a quantum optical effect that uses the $D^0$ spin coherence.

### 5.4.1 Photoluminescence

We performed photoluminescence experiments to identify the spectral region where emission by the donor-bound excitons occurs. We brought excitation light (wavelength $\lambda = 8050$ $\mathring{A}$) to the sample with a fiber-based beam splitter in the optical path (Fig. 5.1). The reflection channel of the beam splitter is coupled to a PI Acton spectrometer, equipped with a nitrogen cooled CCD camera. The light at the excitation wavelength was suppressed by passing the reflected signal through a bandpass filter $\lambda_c = 8200$ Å, $\Delta\lambda = 100$ Å). The sample surface was positioned in the focus of the confocal microscope in order to maximize efficiency of the luminescence collection.

A typical photoluminescence spectrum taken at $B = 5$ T is shown in Fig. 5.5. The spectrum is dominated by three structured peaks, which result from emission by free excitons ($X$), excitons bound to neutral donor sites ($D^0X$), and excitons bound to ionized donor sites in the sample's depletion layer near the surface ($D^+X$). The fine structure due to the Zeeman splitting of the electron and hole spins of the ($D^0X$) and ($D^+X$) bound excitons is observed, but does not provide sufficient information for identifying all the transitions due to the highly unequal oscillator strengths [4].

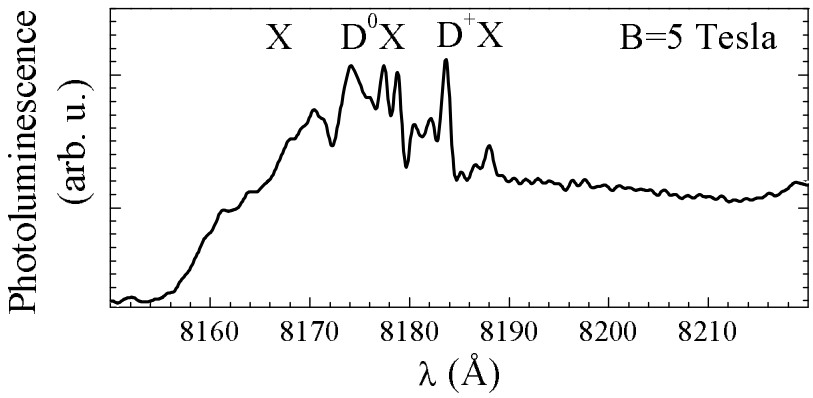


**Figure 5.5:** Photoluminescence spectrum of low-doped $n$-GaAs, showing luminescence by free excitons ($X$), excitons bound to neutral donor sites ($D^0X$), and excitons bound to ionized donor sites in the sample's depletion layer ($D^+X$). Data taken at $B = 5$ T, the resolution of the spectrometer is $\sim 0.2$ Å.

### 5.4.2 Transmission spectroscopy

While photoluminescence is useful for initial characterization of a material and for finding the main spectral features, a more detailed characterization of the $D^0$ systems requires transmission spectroscopy with tunable CW lasers. A few results of this approach were already presented in Fig. 5.4 and discussed in Sec. 5.3.1. Before performing such pump-assisted transmission spectroscopy on the $D^0$ systems, we first take scans with a single laser over a much larger wavelength region for finding the $D^0$ lines. Figure 5.6(a,b) show such transmission spectra taken with H and V-polarized probe light. These results show a strong free-exciton absorption band (labeled $X$), and weaker $D^0X$ resonances. The oscillating background that is superimposed on the transmission spectra is due to a Fabry-Pérot effect in the 10 $\mu$m GaAs film, and its chirped wavelength dependence is due to the wavelength-dependent refractive index associated with the strong free exciton absorption. After locating the $D^0$ lines, we zoom in on this region for identifying the $A$ and $A^*$ transitions with the pump-assisted spectroscopy, as presented in Fig. 5.4(b,c).

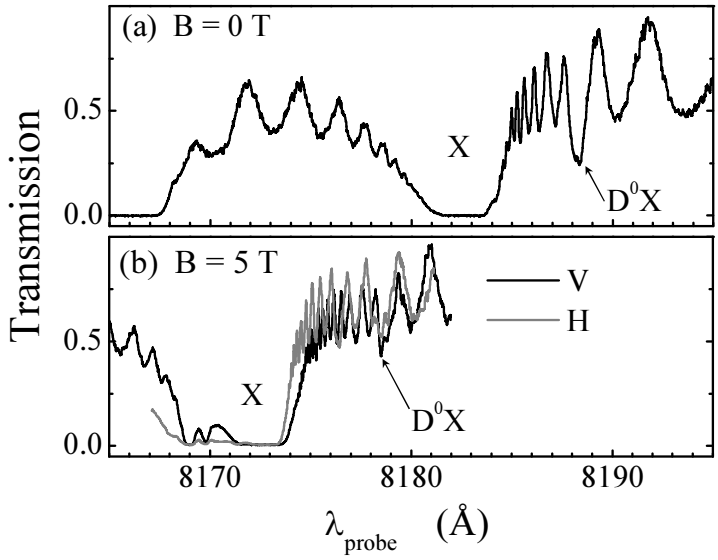


**Figure 5.6:** Scanning-probe transmission spectra taken at $B = 0$ T **(a)** and $B = 5$ T **(b)**. Traces were recorded with linear H or V polarization for the probe light (giving identical results at 0 T). For performing these experiments the microscope was defocussed to a spot diameter of about 16 $\mu$m. The strong absorption due to free excitons ($X$) and much weaker features due to donor-bound excitons ($D^0X$) are labeled. The data at 5 T shows a diamagnetic shift of about 10 Å with respect to the data at 0 T.

### 5.4.3 Electromagnetically induced transparency with donor-bound electrons

We identified the $A$ and $A^*$ transitions because it was our goal to investigate whether these could be used for implementing electromagnetically induced transparency (EIT) with electron spin coherence in a semiconductor. EIT is the phenomenon that an absorbing optical transition becomes transparent because destructive quantum interference with another driven optical transition prohibits populating the optically excited state [32]. This phenomenon lies at the heart of various quantum-optical control schemes that have been designed for preparing nonlocal entanglement between spins, quantum communication, and applying strong optical nonlinearities [25, 32].

EIT can occur with three-level systems as formed by the states $|\uparrow\rangle$, $|\downarrow\rangle$ and $|e\rangle$ (Fig. 5.4(a)), for which it is then essential that the two low-energy spin states can have a long-lived quantum coherence and that one can selectively address the two optical transitions. An ensemble of these systems can become transparent

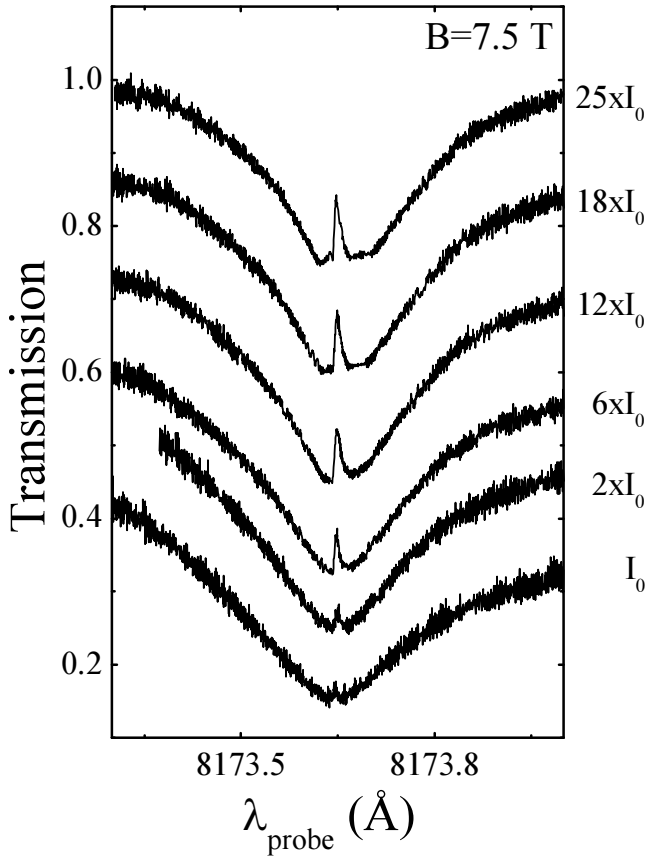


**Figure 5.7:** Electromagnetically induced transparency within the $A^*$ absorption dip, induced by a strong control field that addresses the $A$ transition. Spectra are taken for different intensities $I$ of the control field, with $I_0 = 0.4$ Wcm$^{-2}$. Traces are offset vertically for clarity.

for a probe field that drives one of the transitions (in our case $A^*$) when this meets the condition for a two-photon Raman resonance with an applied control field (in our case driving of transition $A$). Under these conditions the systems are trapped in a dark state which is in the ideal case $(\Omega_c \,|\uparrow\rangle - \Omega_p \,|\downarrow\rangle)/\sqrt{|\Omega_c|^2 + |\Omega_p|^2}$, where $\Omega_c$ and $\Omega_p$ are the Rabi transition frequencies of the control and probe field [32, 26]. Photoluminescence studies on GaAs already showed that optical control can prepare $D^0$ systems in this dark state [4].

We could demonstrate EIT, and typical results are presented in Fig. 5.7. For these results we fixed the control laser on resonance with the $A$ transition (V polarization), while the probe laser is scanned across the $A^*$ transition (H polarization) and we measure its transmission. When the control and probe field

meet the condition for two-photon Raman resonance (the difference in photon energy exactly matches the $D^0$ spin splitting), a narrow peak with enhanced transmission appears inside the broader $A^*$ absorption dip. This is the fingerprint of EIT. In Fig. 5.7 we present traces for various intensities of the control field. We observe a wider and higher EIT peak for stronger driving with the control field, in agreement with theory for EIT.

EIT relies on quantum coherence between the electron spin states, and in systems with a very long electron spin dephasing time $T_2^*$ EIT can fully suppress absorption. The EIT peak then reaches up to ideal transmission. The EIT peaks in Fig. 5.7 are clearly lower, even in the trace for the strongest control field. From fitting these EIT traces to the established theory [32] we derive that the $T_2^*$ value for our system is about 2 ns, and this compromises the EIT peak height. This $T_2^*$ value is consistent with earlier work [4, 13] that showed that electron spin dephasing results from hyperfine coupling between each electron spin and $\sim 10^5$ fluctuating nuclear spins (the $D^0$ systems have a $\sim$ 10 nm Bohr radius). Our EIT studies also showed weak signatures of dynamical nuclear polarization (DNP) which confirmed the role of nuclear spin fluctuations. We anticipate that $T_2^*$ can be enhanced with controlled DNP effects that suppress the nuclear spin fluctuations. A longer account of this EIT study can be found in Ref. [30].

## 5.5 Summary

We presented the realization of a fiber-based confocal microscope that can be used in a dilution refrigerator (base temperature well below 20 mK) with high magnetic field. Faraday rotations in optical materials were circumvented by using a polarization maintaining fiber and by having the light propagation in the sample volume in a direction orthogonal to the applied magnetic field. This also gives access to performing experiments in Voigt geometry, which has several advantages. With experiments on an ensemble of donor-bound electrons in GaAs we confirmed the ability to focus optical control fields with a small spot on any desired point of a sample. We also confirmed that pure linear polarizations can be delivered to the sample, and that this instrument can perform optical experiments at milliKelvin temperatures without excessive heating.

## Acknowledgements

We thank B. Wolfs, A. Slachter, M. Schenkel, J. Sloot and A. Onur for contributions, and J. De Hosson and D. Vainchtein for lending of a spectrometer. Financial support by the Dutch NWO and FOM, and the German programs DFG-SPP 1285, BMBF nanoQUIT and Research school of Ruhr-Universität Bochum is acknowledged.

## References

[1] D. D. Awschalom, D. Loss, and N. Samarth, *Semiconductor Spintronics and Quantum Computation*, (Springer Verlag, Berlin, 2002).

[2] P. Zoller *et al.*, *Quantum information processing and communication*, Eur. Phys. J. D **36**, 203 (2005).

[3] K. Southwell, *Quantum coherence*, Nature **453**, 1003 (2008).

[4] K.-M. Fu, C. Santori, C. Stanley, M. Holland, and Y. Yamamoto, *Coherent Population Trapping of Electron Spins in a High-Purity n-Type GaAs Semiconductor*, Phys. Rev. Lett. **95**, 187405 (2005).

[5] M. Atatüre, J. Dreiser, A. Badolato, and A. Imamoglu, *Observation of Faraday rotation from a single confined spin*, Nature Physics **3**, 101 (2007).

[6] K.-M. C. Fu, S. M. Clark, C. Santori, C. R. Stanley, M. C. Holland, and Y. Yamamoto, *Ultrafast control of donor-bound electron spins with single detuned optical pulses*, Nat. Phys. **4**, 780 (2008).

[7] D. Press, T. D. Ladd, B. Zhang, and Y. Yamamoto, *Complete quantum control of a single quantum dot spin using ultrafast optical pulses*, Nature **456**, 218 (2008).

[8] J. Berezovsky, M. H. Mikkelsen, N. G. Stoltz, L. A. Coldren, and D. D. Awschalom, *Picosecond Coherent Optical Manipulation of a Single Electron Spin in a Quantum Dot*,Science **320**, 349 (2008).

[9] A. Greilich, Sophia E. Economou, S. Spatzek, D. R. Yakovlev, D. Reuter, A. D. Wieck, T. L. Reinecke and M. Bayer, *Ultrafast optical rotations of electron spins in quantum dots*, Nature Physics **5**, 262 (2009).

[10] X. Xu, W. Yao, B. Sun, D. G. Steel, A. S. Bracker, D. Gammon, L. J. Sham, *Optically Controlled Locking of the Nuclear Field via Dark State Spectroscopy*, Nature **459**, 1105 (2009).

[11] D. Brunner, B.D. Gerardot, P. A.Dalgarno, G. Wüst, K. Karrai, N. G. Stoltz, P. M. Petroff, and R. J. Warburton, *A coherent single-hole spin in a semiconductor*, Science **325**, 70 (2009).

[12] C. Latta, A. Högele, Y. Zhao, A. N. Vamivakas, P. Maletinsky, M. Kroner, J. Dreiser, I. Carusotto, A. Badolato, D. Schuh, W. Wegscheider, M. Atature and A. Imamoglu, *Confluence of resonant laser excitation and bidirectional quantum-dot nuclear-spin polarization*, Nature Physics **5**, 758 (2009).

[13] S. M. Clark, K-M. C. Fu, Q. Zhang, T. D. Ladd, C. Stanley, and Y.Yamamoto, *Ultrafast optical spin echo for electron spins in semiconductors*, Phys. Rev. Lett. **102**, 247601 (2009).

[14] C. H. van der Wal and M. Sladkov, *Towards quantum optics and entanglement with electron spin ensembles in semiconductors*, Solid State Sciences **11**, 935 (2009).

[15] A. Imamoglu, *Electromagnetically induced transparency using two dimensional electron spins*, Opt. Comm. **179**, 179 (2000).

[16] H. Türeci *et al.*, *Shedding light on non-equilibrium dynamics of a spin coupled to fermionic reservoir*, arXiv:0907.3854 (2009).

[17] N. A. J. M. Kleemans *et al.*, *Many-body exciton states in self-assembled quantum dots coupled to a Fermi sea*, Nature Physics **6**, 534 (2010).

[18] C. Latta *et al.*, *Quantum quench of Kondo correlations in optical absorption*, Nature **474**, 627 (2011).

[19] A. Högele *et al.*, *Fiber-based confocal microscope for cryogenic spectroscopy*, Rev. Sci. Instr. **79**, 023709 (2008).

[20] P. J. Rizo *et al.*, *Compact cryogenic Kerr microscope for time-resolved studies of electron spin transport in microstructures*, Rev. Sci. Instr. **79**, 123904 (2008).

[21] Purchased and data sheet from Schäfter und Kirchhoff (Germany), (http://www.sukhamburg.de).

[22] E. Munin, J. Roversi, and A. Villaverde, *Magneto-optical constants of fluoride optical crystals and other $AB_2$ and $A_2B$ type compounds*, J. Phys. D: Appl. Phys. **25**, 1635 (1992).

[23] V. K. Valev, J. Wouters, and T. Verbiest, *Precise measurements of Faraday rotation using ac magnetic fields*, Amer. J. Phys. **76**, 626 (2008).

[24] C. C. Robinson, *The Faraday Rotation of Diamagnetic Glasses from 0.334 $\mu$ to 1.9 $\mu$*, Appl. Optics **3**, 1163 (1964).

[25] L. M. Duan, M. D. Lukin, J. I. Cirac, and P. Zoller, *Long-distance quantum communication with atomic ensembles and linear optics*, Nature **414**, 413 (2001).

[26] T. Wang, R. Rajapakse, and S. F. Yelin, *Electromagnetically induced transparency and slow light with n-doped GaAs*, Optics Communications **272**, 154, (2007).

[27] For example available at Knight Optical (UK).

[28] V. A. Karasyuk, D. G. S. Beckett, M. K. Nissen, A. Villemaire, T. W. Steiner, and M. L. W. Thewalt, *Fourier-transform magnetophotoluminescence spectroscopy of donor-bound excitons in GaAs*, Phys. Rev. B **49**, 16381 (1994).

[29] E. Yablonovitch, T. Gmitter, J. Harbison, and R. Bhat, *Extreme selectivity in the lift-off of epitaxial GaAs films*, Appl. Phys. Lett. **51**, 2222 (1987).

[30] M. Sladkov, A. U. Chaubal, M. P. Bakker, A. R. Onur, D. Reuter, A. D. Wieck, C. H. van der Wal, *Electromagnetically induced transparency with an ensemble of donor-bound electron spins in a semiconductor*, Phys. Rev. B **82**, 121308(R) (2010).

[31] E. H. Bogardus and H. B. Bebb, *Bound-Exciton, Free-Exciton, Band-Acceptor, Donor-Acceptor, and Auger Recombination in GaAs*, Phys. Rev. **176**, 993 (1968).

[32] M. Fleischhauer, A. Imamoglu, and J. Marangos, *Electromagnetically induced transparency: Optics in coherent media*, Rev. Mod. Phys. **77**, 633 (2005).

# Chapter 6

# Coupled confocal microscopes with polarization-selective outputs and fiber access in a cryogenic system

**Abstract**

This chapter presents the design and performance analysis of instrumentation that allows for optically accessing a small measurement volume with two uniaxial confocal microscopes in series. For application in a helium bath cryostat, it can be accessed with three fibers: one single-mode polarization-maintaining fiber as input, and two multi-mode fibers as outputs that are connected to collect two orthogonal linear polarizations of light. The polarization filtering is realized with a compact wire-grid polarizer inside the output microscope. The unit is made to fit in the bore of a superconducting magnet of 5 cm diameter, and aligned for measuring in Voigt geometry. This setup is designed for quantum-optical experiments with donor-bound electrons in GaAs, and optimized for wavelengths around 820 nm. Preliminary spectroscopic experiments on a thin layer of $n$-GaAs material are presented as examples that can assess the performance of the setup.

## 6.1 Introduction

Building on the instrumentation development that was reported in Chapter 5, we present here further development of a cryogenic microscope system for the research project of this thesis. The key innovation is that a second confocal microscope was added, in a uniaxial manner, that allows for coupling light out of the measurement volume and cryostat for further processing on an optical table in our laboratory (all the work presented up to this point had a photodetector in the cryogenic measurement volume). While the incoming fiber used remained a single-mode polarization-maintaining fiber, for the output two large-core multi-mode fibers were used, since using a single-mode fiber as well would give extremely challenging alignment and stability issues. To still maintain clear polarization information for the outcoming light, a wire-grid polarizer is placed in the measurement volume, for steering two orthogonal linear polarizations into the two different multi-mode fibers. This instrumentation has not been used for the results presented in the previous chapters, but has been essential for new experimental studies by our team on the GaAs $D^0$ system [1, 2, 3]. In the remainder of this chapter we first focus on design and construction aspects, before presenting results of testing the instrument performance.

## 6.2 Three-fiber coupled confocal microscopes: design and construction

Figure 6.1 presents a schematic overview of the three-fiber coupled confocal microscope system. It is a compact instrument where two microscopes are aligned along one axis. Light of two orthogonal linear polarizations can be fed into (or collected, see Chapter 5) the measurement volume, as carried by a polarization-maintaining fiber. In the sample space these polarizations are identified with respect to the direction of the applied magnetic field: H-polarization (orthogonal to field) and V-polarization (parallel to field). For the ability to analyze (or do other further processing) signal fields that have been transmitted through a material in the sample volume, a second microscope, coupled to a pair of large-core fibers, is added along the optical path. These efficiently-coupled (for collecting light) large-core fibers also facilitate highly-efficient detection of luminescence signals from the sample volume. The output confocal microscope is axially aligned to the light propagation direction of the input confocal microscope, and has lenses that have about a factor four larger diameter lenses as compared to the input

microscope (see Chapter 5). The unit is mounted in a small vacuum chamber (dipstick approach) that fits in the bore of a superconducting magnet (5 cm diameter), in a cryogenic helium-bath environment (but it can in principle be used at any temperature that is created around the vacuum chamber). The alignment of the optical path in the measurement volume corresponds to measuring in Voigt geometry.

The design accounts for the technological challenge to have a setup that can sustain the temperature of liquid helium, while it remains compatible with an (only) three-axis control and feedback mechanism for placing a sample in the focus of the input microscope (see Chapter 5). Notably, this function should be robust against thermal displacements of parts of microscopes over tens of micrometers when the temperature is changed from 300 K to 4.2 K. Further, also this system should be compatible with applying magnetic fields up to about 10 T. The coupled microscopes are designed in such a way that –if required– they can be easily disassembled and reassembled. To minimize stray reflections the overall structure and lens mounts are made of Vespel, a type of plastic developed for space technology. This also avails easy engineering and a way to fix the optical parts with minimum risk of damaging them. The optical parts are selected for using them at wavelengths near 820 nm, which is optimal for spectroscopic studies of the $D^0$ system in GaAs.

### 6.2.1 Input part, sample space and sample holder

To send polarized light in, we use a PANDA-type polarization-maintaining single-mode fiber with a numerical aperture (NA) of 0.13 and a core diameter of 5 $\mu$m. This fiber has different refractive indices for H- and V-polarization and maintains the propagating polarizations in a locked manner, even in strong magnetic fields. The polarization is tested to be maintained up to 9 T [4, 5]. It circumvents the need for building a (bulky) setup for polarization purification inside the dipstick. The light propagation direction out of the polarization-maintaining fiber (Fig. 6.1) is altered by 90° using a prism mirror (part Thorlabs MRA05-E02) to give Voigt geometry in the sample volume. The light coming out of the fiber has a divergent output. This beam is collimated with an aspheric lens of 1.5 mm clear aperture, and 5 mm focal distance and a NA of 0.15 (part Thorlabs 350430). The light is focused in the sample volume with another aspheric lens with focus at 1.45 mm and a NA of 0.55 (part Thorlabs 350140).

The sample space is after the input microscope and is available for use over

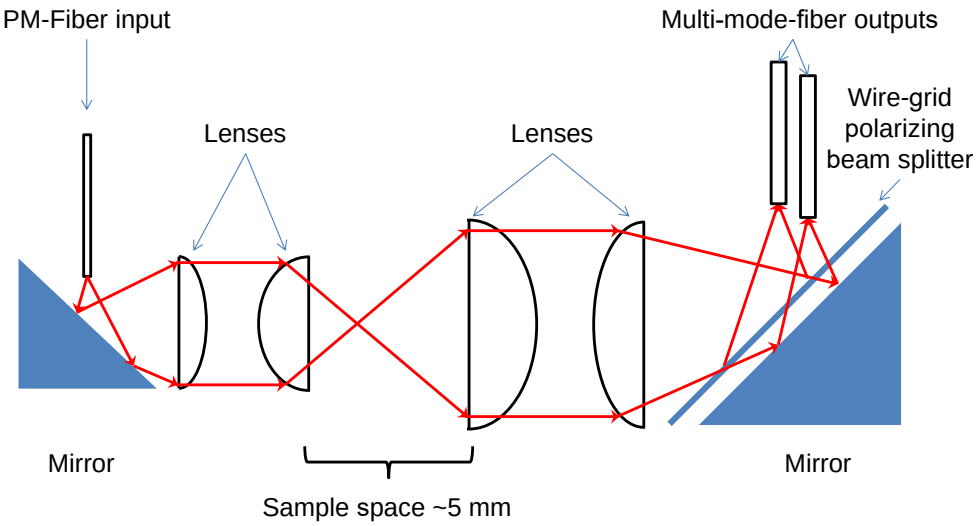


**Figure 6.1:** Schematic representation of the coupled confocal microscope setup. The single-mode polarization-maintaining fiber (PM Fiber), mirror, and a set of two aspheric lenses, form the input part of the setup. It is followed by the sample space, which contains the overlapping focus of the incoming and outgoing optical paths. The sample space along the optical path is about 5 mm. Samples are placed on a copper cold finger which is attached to a three-axes ($xyz$) piezo-motor control stage for controlling the the sample position with respect to the focus. The next pair of aspheric lenses form a second confocal microscope which has a wire-grid polarizer in the optical path according to two linear orthogonal polarizations, which each couple into one of two multi-mode fibers that carry light out of the dipstick.

a distance of about 5 mm along the optical path (Fig. 6.1). For our studies on $n$-GaAs, we typically adhere thin $n$-GaAs layers on a sapphire substrate. In turn, the sapphire is mounted on a narrow copper cold finger using silver paint. The copper cold finger is attached to a piezo-motor control stage (part Attocube ANC120) for precise control in $x$-, $y$- and $z$-direction.

### 6.2.2 Output part

Along the optical path, after the sample volume, light is collected and collimated using an aspheric lens with a clear aperture of 4.95 mm, focal distance of 4.51 mm, and a NA of 0.55 (Fig. 6.1). The second lens of the output microscope is an aspheric lens with a focal distance of 13.86 mm and clear aperture of 5.1 mm. This lens focusses the collimated light on the end facets of multi-mode fibers with

a core of 1000 $\mu$m diameter (part OZ Optics VAC-01-V-QMMJ-3, XF-IRVIS-1000/1100-3- 6.6, 1.4:AR2).

For separating this output according to linear H- and V-polarizations, a wire-grid polarizing beam splitter (WGP) (part Edmund Optics #48-544), made of silver wires on a 700 $\mu$m-thick Corning glass plate (type 1737F, refractive index $\sim$1.51) is placed in the converging output path of the microscope, before the fiber entries. This WGP provides a selective reflectivity and transmission for the H- and V-polarized light. Before we placed the WGP inside the output microscope we carried out an experimental analysis of the reflection and transmission of this system for defining the optimal orientation of the WGP. The WGP is coated on one side with anti-reflection coating for wavelengths between 420 and 670 nm, for minimizing the Fabry-Pérot effect in the glass layer. This means that at our operating wavelengths of $\sim$820 nm, a weak Fabry-Pérot effect is expected, since we use the WGP outside the specified application range (a better model was not available). The results from the above considerations match well with the observations of the polarization filtering by WGP. Hence, we decided to place WGP in such a way that H- (in WGP documentation S-)polarized light will be reflected from the front side (with the wires) of the WGP and V- (in WGP documentation P-)polarized light will be transmitted through the WGP surface.

This results in the following design for light that travels out of the sample volume to the WGP. The part with H-polarized light is reflected from the surface of the WGP and is collected in the first multi-mode fiber. The V-polarized part of the light, which is transmitted through WGP, gets reflected from a mirror (part Thorlabs MRA05-E02) and passes again through the same WGP, before it comes to its focus at the entry of the second multi-mode fiber.

## 6.3 Performance tests

For testing this system's performance we carried out several experiments with or without an $n$-GaAs layer in the system, and both for the system at room temperature and 4.2 K. It includes checks of the output stability as a function of time, as a function of wavelength, and test of the polarization separation in the two output channels. Further, we used this system for performing transmission and photoluminescence spectroscopy on a thin $n$-GaAs layer. We used here again GaAs layers of 10 $\mu$m thickness, with Si doping at $\sim 3 \times 10^{13}$ cm$^{-3}$ (for details see Chapters 2, 3).

### 6.3.1 Two-channel output stability

The stability of coupling light into the output channels is important for sensitive quantum-optical experiments to be performed in the future. The output stability for the system at 4.2 K was monitored as a function of time for both the output channels, such that it also recorded cross talk between the two output channels. For this test there was no GaAs sample in the optical path. The results are presented in Fig. 6.2. These signals are normalized to a reference signal from the laser to remove the influence of drifts in laser power. For these results, either H-polarized light or V-polarized light was sent into the setup via the single-mode fiber, while the optical powers coming out of the H- and V-polarization output channels were monitored.

For both input polarizations the strongest output signal appears in the corresponding channel (for this check the desired transfer H to H and V to V). However, for both cases there also appears significant output in the other channel (H to V, and V to H), on the order of 50% of the desired signal. For a small part ($\sim$5%) this is due to imperfect alignment of the polarization orientation as it enters the measurement volume. However, it also shows that at 4.2 K thermal contractions (possibly giving alignment distortions) reduce the WGP performance to levels that are far from ideal. Nevertheless, with this degree of polarization-selective output one can still analyze the polarization of signal from the measurement volume (below, Ref. [1]). Concerning the stability in time, these transfer properties show slow drifts of a few percent, which we consider satisfactory.

Results of a second test that we performed are presented in Fig. 6.3 (system again at 4.2 K, no GaAs material in the optical path). The goal of this test was to investigate the variation of coupling efficiencies into the output channels as as a function of wavelength. There is indeed such a dependence, which appears in the form of a weak Fabry-Pérot modulation. It occurs both for the H- and V-polarized case, with opposite phase. Since the WGP has clearly non-ideal behavior (see above), this can indeed be expected. The weak Fabry-Pérot effects then occur for both reflection on, and transmission trough the glass plate of the WGP.

### 6.3.2 Transfer losses and two-channel polarization analysis

As an extension of the above tests, we performed a study that compared the performance at room temperature and 4.2 K. Further, we more precisely follow

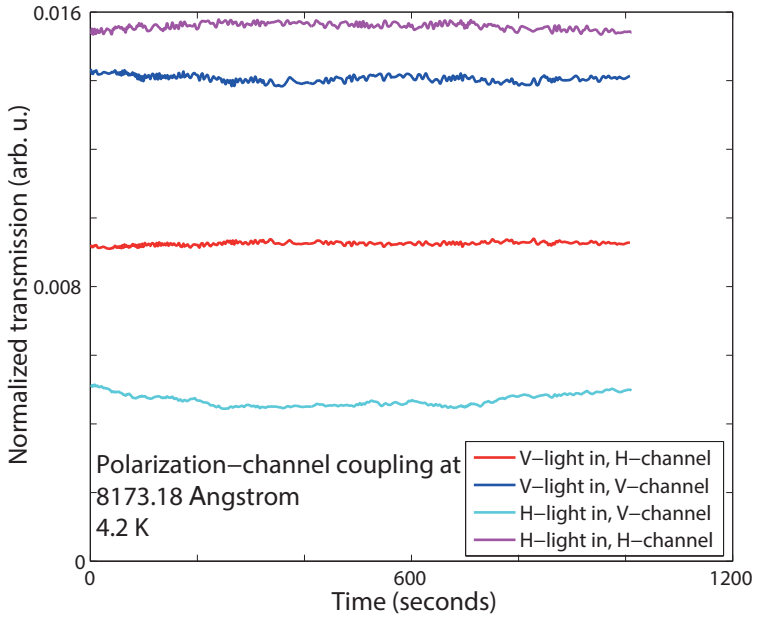


**Figure 6.2:** The output stability of the H- and V-polarization channels as a function of time. H-polarized light was sent into the setup and detected for the two outputs. For this case, the desired output (H-channel) is measured (purple trace), while the undesired cross-talk into the V-channel is measured as well (light-blue trace). For similar measurements carried out with sending V-polarized light into the system, the V-polarized channel output is presented with the dark-blue trace, and the H-channel output is presented with the red trace.

the normalized power transfer of laser beams entering and leaving the system, and better measure the behavior of the two-channel power distribution by the WGP as a function of polarization.

For these tests we fixed the input wavelength, and determined the power output of the H- and V-channel, each normalized to the laser power sent into the polarization-maintaining fiber. As a first step (at room temperature and with the measurement volume open), we confirmed the proper alignment of the H- and V-axis of the polarization-maintaining-fiber connection (the output) at the entry of the measurement volume. In addition, we marked the rotation settings of a half-wave plate that was placed right before the entry of this polarization-maintaining fiber that give pure H- and V-polarization in the sample space inside the microscope (before this half-wave plate we purified the beam to a linear polarization at the level of $10^5$ to 1). These angles were 238° for V-polarization, and 328° for H-polarization (measured with respect to an arbitrary reference point

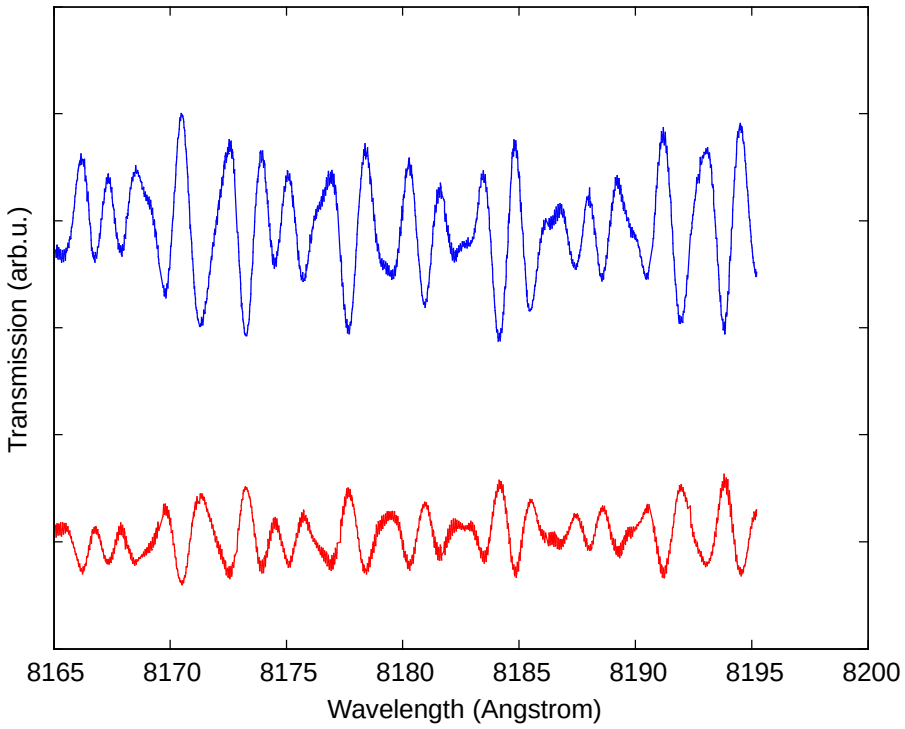


**Figure 6.3:** The output of the H- and V-polarization channels as a function of input wavelength, measured with input polarization aligned to the relevant output channel. The measured output signals show weak out-of-phase Fabry-Pérot oscillations.

in the mechanical mount), and are marked as vertical black lines (separated by 90°) in Fig, 6.4.

In turn, with the full system assembled, we studied the powers coming out of the H- and V-channel output fibers as a function of the rotation of the half-wave plate. Figure 6.4(a) presents the results of this test (with sinusoidal fits to the measured dependence on angle). Qualitatively, these two output signals show the expected sinusoidal behavior with opposite phase. The angles of the half-wave-plate rotation that lead to maximum power in the H- or V-channel are close to the expected setting: there is a $\sim 4^\circ$ offset, which is compatible with the precision of mounting that could be achieved for the polarization-maintaining fiber. Further, the measured power levels confirm a power loss of only a few percent, compatible with the performance of the anti-reflection coatings at all parts.

Figure 6.4(b) presents the results of performing the same measurements after cooling the system to 4.2 K. The outcome of these experiments was similar, but there are two significant differences. The power transfer through the entire system

decreased by about a factor 10, and the rotation offset between controlling pure H- and V-polarization and the observed maximum powers in the H- and V-output channels changed from ∼4° to ∼14° in the opposite direction. This indicates that the thermal contractions of the system indeed lead to a significant alignment disturbance. The behavior of the system on this aspect can probably be improved by designing a mechanical construction (Fig. 6.1) that is fully symmetric around the optical axis.

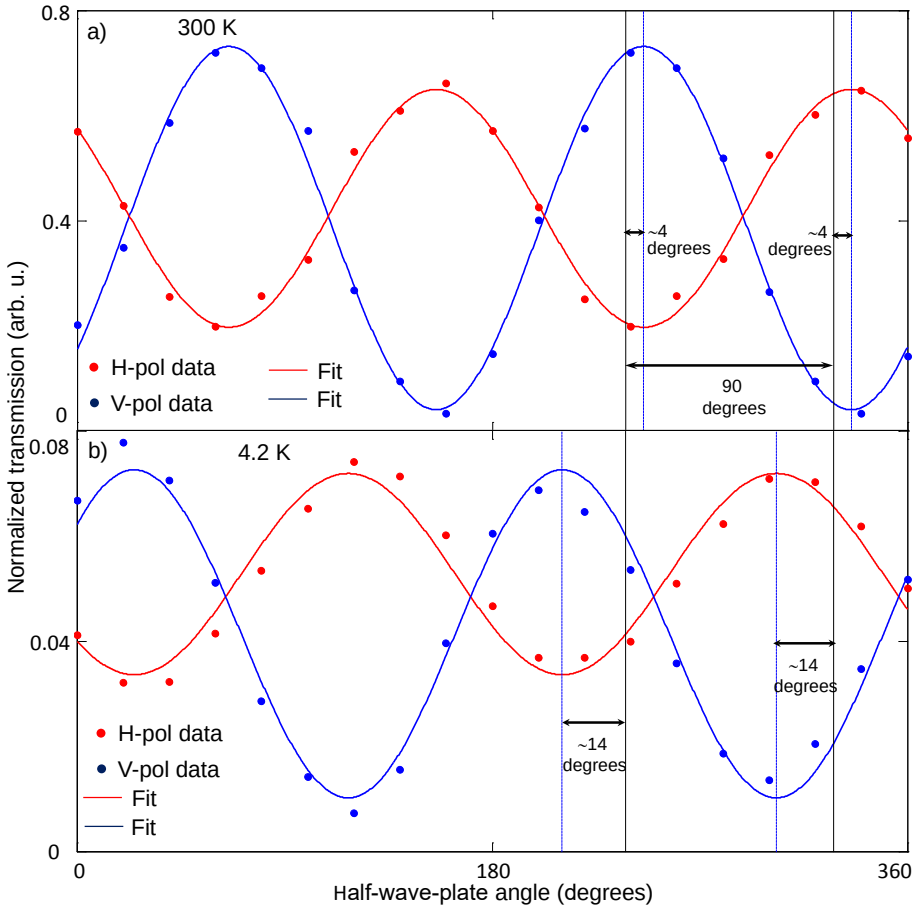


**Figure 6.4:** Results from testing polarization separation into the H- and V-polarization output channels, obtained with the system at room temperature **(a)** and 4.2 K **(b)**. The measured results (dots) represent normalized intensity output from the two different multi-mode-fiber output channels (as labeled) as a function of input polarization (controlled with a half-wave plate before the input of the polarization-maintaining fiber at room temperature). The solid traces are the result of fitting a sinusoidal dependence on the measurement results.

### 6.3.3 Spectroscopy tests on $n$-GaAs

Further performance tests were carried out by executing measurements on the $n$-GaAs layer. We first present transmission and photoluminescence spectroscopy results, before presenting tests of using the setup as an imaging tool.

**Transmission spectroscopy**

Figure 6.5(a) presents results from a single-laser-scan transmission spectroscopy study on the $n$-GaAs layer (see also Chapter 3). Here the detector measured light collected via the V-channel output. The material was at 4.2 K and in zero magnetic field. The results demonstrate that detection of transmitted light gives spectroscopy results that are in quality at least similar to the results in Fig. 3.2. The spectrum shows again the typical features for low-doped $n$-GaAs (absorption from free-exciton $X_{n=1}$ transitions, and $D^0$-$D^0X$ transitions).

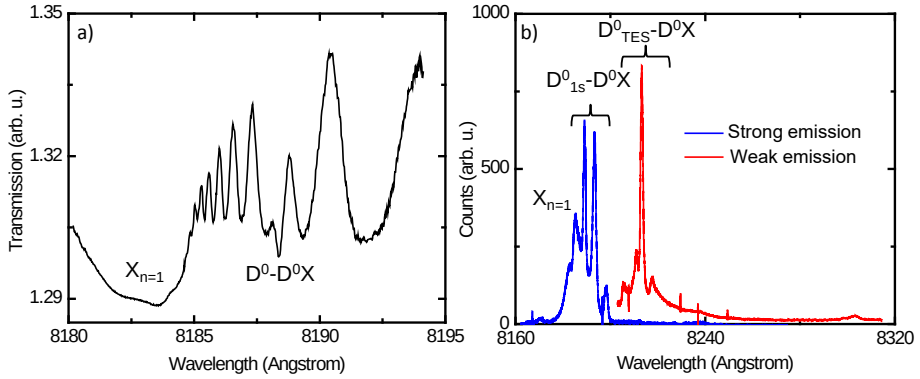


**Figure 6.5: (a)** Transmission spectrum for the $n$-GaAs layer at 0 T field. The observed transitions are identified and labeled as $D^0$-$D^0X$ transitions, and the free-exciton $X_{n=1}$ transition. **(b)** Photoluminescence spectrum from the $n$-GaAs layer. The observed spectral lines are identified and labeled as emission from $X_{n=1}$ free-exciton transitions, several lines of $D^0_{1s}$-$D^0X$ transitions, and several lines of $D^0_{TES}$-$D^0X$ transitions (see main text). These spectra were detected via the channel that collects V-polarized light. The red trace (for weaker emission) was obtained by spectral blocking of the stronger emission (peaks in the blue trace), and using a 100 times longer integration time for the CCD camera.

**Photoluminescence spectroscopy**

Figure 6.5(b) presents results that demonstrate the use of the new output channels for collecting photoluminescence (PL) signals from the $n$-GaAs layer. The results were obtained with the sample at 4.2 K, and in zero magnetic field.

The sample was illuminated via the polarization-maintaining fiber, with a laser tuned to a photon energy higher than the band gap (blocked from the spectra in Fig. 6.5(b)). For detection the V-polarization output channel was used, and this output was aligned on a 75-cm grating spectrometer (PI Acton), equipped with a liquid-nitrogen cooled CCD camera. As compared to PL readout that used back scattering into the singe-mode fiber (Fig.5.5), the data quality shows a great improvement. It shows several features of sub-band-gap emission by low-doped $n$-GaAs: emission by free excitons, neutral donor-bound excitons, ionized donor-bound excitons, acceptor-bound excitons, as well as the so-called two-electron satellites (TES) [6, 7] of the neutral donor-bound excitons (transitions from $D^0X$ levels to an excited state of the $D^0$ system, which has the electron in a $2s$ or $2p$ orbital of the envelope wave function, see also Chapter 1).

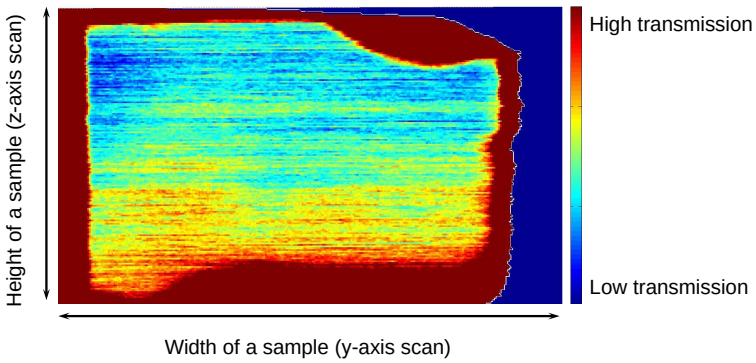


**Figure 6.6:** Result of imaging a ∼1.5 by ∼2.5 mm$^2$ $n$-GaAs sample via the free-exciton response, measured in transmission. The image is built via two-dimensional scanning of the sample position with the $x$- and $z$-direction piezo motors (directions as defined in Fig. 5.1). The experiment used a single excitation laser, with the wavelength fixed in the transmission window between the $X_{n=1}$ and $X_{n=2}$ free-exciton absorption resonances (see also Fig. 3.2(a)). The results reflect both the sample geometry and small changes in the transmission due to position-dependent shifts of the bang gap and excitonic transitions (which provides a signal for strain in the material). The resolution of this image is limited by the minimum spot-size in the focus of the setup (∼2 $\mu$m diameter).

### 6.3.4 Imaging tests on $n$-GaAs sample

Our approach to studying thin $n$-GaAs layers is based on transferring them onto a sapphire substrate (Chapter 2, 5). This process may result in local strain at

a few places in such a $n$-GaAs layer. The presence of strain causes shifts in the GaAs band gap, and shifts and splittings of spectral lines of excitonic transitions [8, 9, 10]. Thus, while scanning the sample position with respect to the focus of the laser beam, and with the laser at a fixed wavelength near an excitonic transition, transmission studies of the material can give an imaging signal that reflects local strain. We apply this approach by applying a single laser that is fixed at a wavelength between the free-exciton $X_{n=1}$ and $X_{n=2}$ absorption resonances, with the sample at 4.2 K and in zero magnetic field (see Fig. 3.2(a)). For having a strong response to the occurrence of strain (which shifts the free exciton lines [9, 10]) the laser is tuned to a steep part in the absorption spectrum, at the edge of the $X_{n=2}$ transition. Next, we use the piezo-motor stage for scanning the sample position with respect to the laser focus. Results of sample transmission as a function of position in the sample, obtained in this manner, are presented in Fig. 6.6. After obtaining this data, spectroscopy as a function of laser frequency is performed on a region of well-defined transmission, such that the transmission information can be turned into information about the local spectral shift for the material.

This imaging method saves a lot of time in finding a suitable spot on a $\sim$2 by $\sim$2 mm$^2$ GaAs layer: for our research we need areas that have homogeneous strain properties (to avoid inhomogeneous broadening of optical transitions), for laser beams that are typically tuned to give 2 to 50 $\mu$m spot diameters on the sample. In addition, it is desirable to select areas with either no significant strain, or strain that is high enough to cause significant shifts and splittings of spectral lines [8]. Further application of this approach is reported in Ref. [2].

## 6.4 Summary and outlook

This chapter presented further development of the cryogenic microscope that has been central for obtaining the results in this thesis. While the performance of the new part (polarization-selective output from the measurement volume) is not ideal, it clearly improved the experimental setup. Besides use for the tests presented in this chapter this instrument has recently been essential for a range of GaAs $D^0$ studies in our team [1, 2, 3]. In addition, it realizes a significant instrumentation step for experiments that make further use (beyond only direct detection) of quantum-optical light pulses that have been emitted by a material system in the sample volume.

# Acknowledgements

We thank B. H. J. Wolfs for help and acknowledge the Dutch Foundation for Fundamental Research on Matter (FOM), the Netherlands Organization for Scientific Research (NWO), and the German programs DFG-SFB 491 and BMBF-nanoQUIT for funding.


# References


[1] A. R. Onur, *Optical control of mesoscopic spin ensembles in gallium arsenide* (PhD thesis, University of Groningen, 2015).

[2] J. P. de Jong, *Optically addressing semiconductor electron-spin ensembles with tunable nuclear-spin environments* (PhD thesis, University of Groningen, 2016).

[3] A. R. Onur, J. P. de Jong, D. O'Shea, D. Reuter, A. D. Wieck, and C. H. van der Wal, *Stabilizing nuclear spins around semiconductor electrons via the interplay of optical coherent population trapping and dynamic nuclear polarization*, Phys. Rev. B **93**, 161204(R) (2016).

[4] Maksym Sladkov, M. P. Bakker, A. U. Chaubal, D. Reuter, A. D. Wieck, and C. H. van der Wal, *Polarization-preserving confocal microscope for optical experiments in a dilution refrigerator with high magnetic field*, Rev. Sci. Instr. **82**, 023709 (2011).

[5] Purchased and data sheet from Schäfter und Kirchhoff (Germany), (http://www.sukhamburg.de).

[6] V. A. Karasyuk, D. G. S. Beckett, M. K. Nissen, A. Villemaire, T. W. Steiner, and M. L. W. Thewalt, *Fourier-transform magnetophotoluminescence spectroscopy of donor-bound excitons in GaAs*, Phys. Rev. B **49**, 16381 (1994).

[7] K.-M. C. Fu, *Optical Manipulation of Electron Spins Bound to Neutral Donors in GaAs* (PhD thesis, Stanford University, 2007).

[8] V. A. Karasyuk, M. L. W. Thewalt, and A. J. SpringThorpe, *Strain effects on bound exciton luminescence in epitaxial GaAs studied using a wafer bending technique*, Phys. Stat. Sol. B **210**, 353 (1998).

[9] W. Schairer, D. Bimberg, W. Kottler, K. Cho, and M. Schmidt, *Piezospec- troscopic and magneto-optical study of the Sn-acceptor in GaAs*, Phys. Rev. B **13**, 3452 (1976).

[10] D. C. Reynolds, C. W. Litton, T. C. Collins, and S. B. Nam, *Free-exciton energy spectrum in GaAs*, Phys. Rev. B **13**, 761 (1976).

# Academic summary

### Electromagnetically induced transparency with localized impurity electron spins in a semiconductor

This PhD thesis contributes to a research field that aims to understand and extend the limits of how well quantum states of matter and electromagnetic fields can be prepared, controlled and detected. On the one hand, this field is driven by fundamental questions that are not yet fully answered: can we better understand the transition between quantum physics and classical physics that is observed in the behavior of several material systems, and what are the limits for obtaining purely quantum mechanical behavior for suitably designed systems? On the other hand, this field is driven by proposed applications from quantum information science. These proposals consider that the state of a bit of information (which classically can only be in the state 0 or 1) can behave quantum-mechanically (such that the bit can be in a quantum state that is 0 and 1 at the same time). The performance of quantum information processing can be dramatically superior to classical information processing, but it is currently still a scientific challenge to realize quantum information systems that are large and stable enough for actual application in society. Just as for the fundamental questions, progress here requires better understanding of how a material system can have pure quantum mechanical behavior that is only weakly and slowly disturbed by noise from its environment.

The research presented in this PhD thesis investigated questions with relevance for this field with laser control of the quantum state of electron spins in a semiconductor. It thereby addressed the challenge of realizing quantum information systems with semiconductor technology, for which it is anticipated that it is (relative to other material systems) well suited for scaling small units to large-scale systems. The focus was on the spin of donor electrons, which occur as localized singe-electron systems at donor atoms (intentionally added impurities) in the semiconductor gallium arsenide (GaAs). The rational for working with this

material system is that it has good optical properties that are well understood, and that the material can be grown as very pure and high quality crystals.

Central to this PhD research was the question whether Electromagnetically Induced Transparency (EIT) could be realized with the spin of donor-impurity electrons in GaAs. This effect, EIT, had already been realized and widely studied with laser control of atomic vapors, but was not yet widely explored with atom-like systems in a solid-state material. EIT is the phenomenon that (near-) resonant laser driving of an electronic transition of a medium does not behave as an optically absorbing resonance, but allows the laser field to propagate as in a transparent medium because a second laser field also influences the medium. In particular, it can occur when the two lasers each drive a transition from one of two spin states to the same excited state. The electronic system is then trapped in a controllable quantum superposition of the two spin states, and the system's driven dynamics does not give transitions to the excited state because the two paths in parallel interfere destructively. EIT forms the basis of many quantum-optical control schemes that use long-lived spin states that must be coupled to optical signal fields.

After an introductory chapter, *Chapter 2* presents an approach to, and successful demonstration of EIT with an ensemble of donor-bound electron spins in GaAs. It used optical transitions from the Zeeman-split electron spin states of the donors to an excited state where an additional electron-hole pair is localized around the donor impurity (donor-bound exciton). The quality of the spectral signature of EIT could be used to derive that the electron spin dephasing time was about 2 ns. The behavior of the spectral EIT signature also indicated that the electron spin coherence was limited by the coupling of the electron spin to the spins of many surrounding nuclei in the GaAs lattice (hyperfine interaction).

Next, in *Chapter 3*, we report a further investigation of the optical transitions between the donor ground state and the donor-bound-exciton states. Our approach to EIT also yields a method for high-resolution optical spectroscopy of these transitions in a transmission experiment. The results do not only contribute to ongoing research into the fundamental properties of donor-bound excitons, but are also relevant for optimizing EIT control with this material system. We compare our results to existing theory, and conclude that existing models do not yet fully describe our observations. At the same time, our results do establish what the suitable optical transitions are for EIT, and how nearby transitions to other levels of the donor-bound-exciton system can possibly influence the behavior of EIT.

*Chapter 4* of this thesis described results of exploring how driving EIT with donor electrons in GaAs can influence and probe the interactions between each donor electron spin and the ensemble of nuclear spins in its direct surroundings (hyperfine interaction). We observe how EIT can both drive and probe dynamic nuclear polarization (DNP). DNP can occur when one drives the electron spin polarization out of thermal equilibrium (as we can do with the EIT laser control scheme), while relaxation of the electron spin polarization to its equilibrium value causes polarization of the nuclear spins (the hyperfine interaction gives electron-nuclear-spin flip-flop as relaxation processes). Since nuclear spin polarization influences the energy splitting between the electron spin states, it should also influence the spectral signature of EIT. We indeed observe that EIT can be used for influencing and monitoring the build-up and decay of DNP. This observation is of value as a first step towards laser control of the nuclear spins into a state that gives less dephasing for the electron spin coherence.

In *Chapters 5 and 6* we report on the design, development and testing of dedicated instrumentation that was required for the research of the previous chapters. We did all experiments in a helium-bath cryostat with applied magnetic fields up to 9 Tesla in the measurement volume. For sending well-defined laser beams to GaAs samples we developed an approach with a polarization-maintaining optical fiber and a compact confocal microscope in the measurement volume, with a piezo-motor driven focussing mechanism. Initial work used detection signals from photodiodes inside the cryogenic measurement volume. At later stages this instrumentation was developed further to one where a pair of multi-mode fibers was aligned to collect light after transmission through GaAs (or emitted by GaAs) for more advanced light detection and signal analysis outside the cryostat. This set-up allows for recording an EIT spectrum much faster, and will be useful for future quantum-optical and DNP experiments with our GaAs material system.

# Wetenschappelijke samenvatting

### Elektromagnetisch geïnduceerde transparantie met gelokaliseerde elektronspin van onzuiverheden in een halfgeleider

Dit proefschrift geeft een bijdrage aan een onderzoeksveld dat zich tot doel stelt te begrijpen hoe goed we de kwantumtoestanden van materie en elektromagnetische velden kunnen prepareren, controleren en detecteren. Dit onderzoeksveld wordt aan de ene kant gedreven door fundamentele vragen die nog niet volledig zijn beantwoord: kunnen we de overgang van kwantumfysica naar klassieke fysica die we waarnemen met verschillende materiaalsystemen beter begrijpen, en wat zijn de grenzen die bestaan voor het krijgen van puur kwantummechanisch gedrag bij systemen die specifiek hiervoor zijn ontworpen? Aan de andere kant wordt dit veld voortdurend geïnspireerd door toepassingsvoorstellen vanuit de kwantuminformatie wetenschap. Deze veronderstellen dat de toestand van een informatie-*bit* (die klassiek alleen in de toestand 0 of 1 kan zijn) zich kwantummechanisch kan gedragen (zodat de bit in een kwantumtoestand kan zijn die tegelijk 0 en 1 is). De prestaties van kwantuminformatie-verwerking kunnen ontzettend ver uitstijgen boven de prestaties van klassieke informatieverwerking. Echter, het is op dit moment nog een wetenschappelijke uitdaging om kwantuminformatie-systemen te realiseren die groot en stabiel genoeg zijn voor daadwerkelijke toepassing in de maatschappij. Net als voor de fundamentele vragen, is voor vooruitgang hier behoefte aan beter inzicht in hoe een materiaalsysteem zuiver kwantummechanisch gedrag kan hebben dat slechts zwak en langzaam wordt verstoord door ruis vanuit zijn omgeving.

Het onderzoek dat dit proefschrift presenteert richtte zich op vragen met relevantie voor dit onderzoeksveld, door met lasers de kwantumtoestand van de spin van elektronen in een halfgeleider te controleren. Hiermee richtte het onderzoek zich op het realiseren van kwantuminformatie-systemen met halfgeleidertechnologie, waarvoor geldt dat het opschalen van een kleine basiseenheid naar een groot systeem waarschijnlijk makkelijker is dan voor andere materiaalsystemen. De

focus lag op de spin van donor-elektronen, die als gelokaliseerde enkel-elektron-systemen voorkomen bij donor-atomen (bewust toegevoegde onzuiverheden) in de halfgeleider galliumarsenide (GaAs). De keuze voor dit materiaalsysteem was gebaseerd op het feit dat GaAs zeer goede optische eigenschappen heeft, en het feit dat dit materiaal gegroeid kan worden als kristallen die extreem zuiver zijn en een bijna perfecte kristalstructuur hebben.

Een centrale thema in dit promotieonderzoek was de vraag of elektromagnetisch geïnduceerde transparantie (EIT) kan optreden met de spin van donor-elektronen in GaAs. Dit effect, EIT, was al gerealiseerd en uitgebreid bestudeerd met laser-controle van atoomdampen, maar was nog vrijwel niet onderzocht met kwantumsystemen in vaste stof. EIT is het verschijnsel dat het (bijna) resonant aandrijven met lasers van een elektronische overgang in een medium niet leidt tot een resonante absorptie, maar dat de laserbundel zich door het medium voortplant als bij een transparant materiaal. Dit treedt dan op omdat een tweede laser het medium ook beïnvloedt. Dit kan optreden wanneer twee lasers elk een overgang aandrijven vanuit één van twee spintoestanden naar dezelfde geëxciteerde toestand. Het elektronische systeem wordt dan in een controleerbare kwantum-superpositie toestand van de twee spintoestanden geduwd. De dynamica van het aangedreven systeem geeft dan geen overgangen naar de geëxciteerde toestand omdat de twee parallelle excitatie-routes destructief met elkaar interfereren. EIT vormt de basis van veel kwantum-optische controlemethodes die gebruik maken van langlevende spintoestanden die aan optische signaalvelden moeten worden gekoppeld.

Na een inleidend hoofdstuk, presenteert *Hoofdstuk 2* een benadering voor, en succesvolle demonstratie van EIT met een ensemble van donor-gebonden elektronspins in GaAs. De aanpak maakt gebruik van optische overgangen vanuit de Zeeman-opgesplitste elektron-spintoestanden van de donoren naar een geëxciteerde toestand waarbij er een extra elektron-gat paar gelokaliseerd is bij het donor-atoom (donor-gebonden exciton). De kwaliteit van de spectrale verschijning van EIT kon worden gebruikt om te bepalen dat de defaseringstijd voor de elektronspin 2 ns was. Het gedrag van de EIT resonantie in het spectrum gaf ook aan dat de elektronspin-coherentie beperkt wordt door koppeling van de elektronspin met de spins van vele kernen in het GaAs rooster, in de directe omgeving van elk donor-atoom (hyperfijn-interactie).

In het volgende *Hoofdstuk 3* rapporteren we verder onderzoek naar de optische overgangen tussen de grondtoestand van de donor en de donor-gebonden-exciton toestanden. Onze benadering voor EIT geeft ook een methode om met

zeer hoge resolutie optische spectroscopie uit te voeren voor deze overgangen met een transmissie-experiment. De resultaten hiervan geven niet alleen een bijdrage aan lopend fundamenteel onderzoek naar de eigenschappen van donor-gebonden-exciton systemen, maar zijn ook relevant voor het optimaliseren van EIT-controle met dit materiaalsysteem. We vergelijken onze resultaten met bestaande theorie, en concluderen dat de bestaande modellen nog niet volledige onze waarnemingen kunnen beschrijven. Tegelijkertijd leggen onze resultaten wel vast welke optische overgangen geschikt zijn voor EIT, en hoe de overgangen naar andere dichtbij gelegen toestanden van het donor-gebonden-exciton systeem mogelijk invloed uitoefenen op het gedrag van EIT.

*Hoofdstuk 4* van dit proefschrift beschrijft onderzoek naar de vraag hoe EIT met donor-elektronen in GaAs zowel invloed kan uitoefenen op, als de effecten kan weergeven van de interacties tussen elke donor elektronspin en het ensemble van kernspins in zijn directe omgeving (hyperfijn-interactie). Onze waarnemingen laten zien dat EIT dynamische nucleaire polarisatie (DNP) zowel kan aansturen als meten. DNP kan optreden als men de elektronspin-polarisatie uit thermisch evenwicht brengt (hetgeen we kunnen doen met EIT-controle), terwijl relaxatie van de elektronspin-polarisatie naar zijn evenwichtswaarde nucleaire spinpolarisatie kan aandrijven (de hyperfijn-interactie geeft elektron-nucleaire-spin flip-flop processen als relaxatieproces). Omdat nucleaire spinpolarisatie invloed heeft op de waarde van de energie-opsplitsing tussen de twee elektronspintoestanden, moet deze ook zichtbaar zijn in de spectrale weergave van het EIT effect. Onze waarnemingen laten inderdaad zien dat EIT kan worden gebruikt voor het beïnvloeden en volgen van de opbouw en relaxatie van DNP. Deze resultaten zijn van belang als een eerste stap voor de realisatie van lasercontrole die nucleaire spins in een toestand brengt die minder defasering geeft voor de elektronspin coherentie.

De *Hoofdstukken 5 en 6* rapporteren het ontwerp, ontwikkelen en testen van specifieke meetinstrumentatie die nodig was voor het onderzoek van de voorgaande hoofdstukken. Alle experimenten zijn uitgevoerd in een helium-badcryostaat, waarbij een magneetveld tot 9 Tesla kon worden aangelegd in het meetvolume. Voor het aanleggen van goed gedefinieerde laserbundels in de GaAs onderzoeksmaterialen hebben we een benadering ontwikkeld met polarisatie-behoudende optische fibers en een compacte confocale microscoop in de cryogene meetruimte, met piezo-motoren voor het scherp stellen van de optische focus. Onze eerste experimenten gebruikten voor het detecteren van optische signalen fotodiodes binnenin de cryogene meetruimte. In de tweede helft van dit pro-

motieonderzoek is aan dit systeem de mogelijkheid toegevoegd om optische signalen (van transmissie door GaAs, of emissie door GaAs) ook vanuit de cryostaat naar buiten te voeren. Dit is van belang voor betere detectie van de optische signalen, en betere signaalanalyse. Hiermee is het mogelijk de EIT spectra veel sneller te meten, wat verdergaand onderzoek naar kwantum-optische effecten en DNP met het donor-elektron materiaalsysteem in GaAs mogelijk maakt.

# Acknowledgements

For me it took a little long to finish my thesis. The work presented in this thesis is executed and completed between August 2009 and October 2013 in the group of Physics of Nanodevices, in Zernike Institute for Advanced Materials, at University of Groningen. Further till 2017 the thesis got finalized and got into the shape where it can be defended. When I look back in time, I would say, for me, it was a spectacular journey. Not only the part when I worked on PhD, but also till the time I got this rare opportunity to work in an experimental physics laboratory. Several people and research organizations have contributed directly or indirectly in helping me complete the journey. I would like to express my humble gratitude towards all the contributors.

First and foremost I would like to thank my parents and paternal aunt for their love, patience, and trust. They have played a big role in building up my personality during my upbringing which helps me to blend in with my surrounding. I would like to thank my wife and PhD time girlfriend Mayuri Nalawade for all the love, care, and patience she had with me during all these years of PhD.

My research experience started in 2006 in TIFR, Mumbai, India. I worked in Prof. S. S. Prabhu's Laboratory. I enjoyed working in a laboratory that was the time I realized I want to do PhD. When I was about to join TIFR, I got an offer to work in industry with better remuneration. I took a chance to work in research field instead of working in the industry. I have no regrets taking this decision. It opened a new world of semiconductor industry, possibility to work internationally, and to work in research and high-tech environment. I dared to dream big because of Prof. S. S. Prabhu. I thank Prof. S. S. Prabhu for mentoring me, supporting me, and motivating me. I learned from you how to be humble, expressive, polite and a nice human being.

When I was still working at TIFR, I started looking for PhD positions. I must say it was a tough time to find a position at that time due to economic crises. After getting denied from several universities during economic crises around 2008, I decided for myself to make a last and final application for PhD. I was almost

instructed by Prof. S. S. Prabhu to apply for a position at University of Groningen. Actually, as soon as I wrote application I started looking for jobs in finance sector in India thinking I am not going to make it through the first screening itself. I was surprised to receive an email from Prof. Tamalika Banerjee with an opportunity to have a skype interview. Further, I came here for an interview, got selected, and started working with Prof. Caspar van der Wal. It all happened in such a short period of time that I was still digesting the fact that I am already in Groningen and working on my PhD. I would like to thank Prof. Tamalika Banerjee, Prof. Caspar van der Wal, and Prof. Bart van Wees for giving me an opportunity to discuss my work, and my ambition and of course to offer me a position in their group. During this step Prof. Tamalika Banerjee gave me critical opinions about content of the presentation, timelines to prepare myself for the interview within the group and giving me insight about dutch culture. I express my gratitude towards Prof. Tamalika Banerjee without whom it could have been difficult to face interviews.

I want to say a big thank you to Prof. Caspar van der Wal. You have always helped me and you were always a person I counted on at very critical moments, be it research or personal life situations. You are a nice human being, a proud father, and a successful academician. I want to thank you for a long list of things. On top of that list, you taught me how to be critical, and organized. There are qualities in you which separates you from indifferent supervisors. There is a small kid in your heart which keeps you going with a lot of energy and enthusiasm. It was not always easy to keep up with your enthusiasm and perfection. It caused plenty of rework and some arguments. It helped me getting into pace of dutch way of working. I am benefitting from hard and soft skills I learned during this entire process. I must say I got my first job, just because you insisted I shall learn a few hard skills during last few months of my PhD. I appreciate that you have actively participated in the research and experiments by being physically present in the laboratory from time to time. I must confess that sometimes I was worried when you used to voluntarily spend time in the laboratory doing measurements.

I thank Prof. Bart van Wees for giving me opportunity to work in his group. Your gut feelings and ability to ask critical questions on the loose ends of the topic always impressed me. I was always afraid to hear your statement, " But wait a minute my friend, we have to be very careful here now" this statement always came up as precursor of upcoming question.

Research is fun only when instruments and set-up works. There is a big contribution from a very young and retired boy Bernard Wolf. Bernard I owe

you a lot. You were there for weekend refills, fixing my set-ups, organizing helium on 11th hour notice and I cannot even count where you have covered up for my mistakes in the laboratory. I think I was best at breaking things and Bernard, you used to fix them. We also shared dark humor and crazy jokes, few jokes I don't even want to mention here. I am very happy that you are married now and enjoying a healthy retired life with lot of sports and activities. It is my pleasure to work with you. I thank you Martijn. After Bernard's retirement you kept the same energy and spirit in the group. I must say that you were there exactly when I wanted to finish a lot of measurements in a short time. You kept on soldering and welding detectors for me. Remember a hole in the dipstick? Thanks for fixing that! I want to thank Johan for giving right advice. You also helped me in the cleanroom, specially while handling HF acid. You were strict but that's why safety was always maintained in the FND cleanroom. I had rather a small overlap with Simon. I knew him as a happy and healthy man. Somehow being fit did not go in his favor. May his soul rest in peace. I always had interesting discussions with him specially about cultures, capital punishments, terrorism and so on.

Anna, you are the most efficient secretary I have ever seen. You could bond with all the young nerds in the group and you could handle all the crazy last minute requests they came up with. Of course I was one of them.

I thank Maksym Sladkov for transferring all Laboratory tricks. By the way you introduced me to very sophisticated spirits and they are awesome! I thank you Sergii Denega, you were an angel who never let me get fat by eating chocolates from my drawer. I thank you Javaid Iqbal. Making videos for your defense was a lot of fun. I tried my best to help you even though our topics were different. I thank the three musketeers Sander Onur, Jakko de Jong, Olger Zwier. Guys we had a lot of borrels and dinners together. It was a lot of fun, specially we had similar nerdy jokes and of course "famous sayings". I thank you all because I learned to co-operate, collaborate and brainstorm together. I also learned importance of forwarding the knowledge and skills. I thank you Jorrit Sloot, you were an amazing Master student with gut feelings and new experimental ideas. I thank Danny O'Shea for helping me with English. I hope things turn good for you in coming future.

I have special thanks to Thomas Massen, Marta Walasek, Marcos Guimaraes, Lara Sanchez for baring with me for all these years specially during the time when I was off all the stimulants for 3 months. Life becomes much easier when you meet friends who think alike specially when it is about dark humor. Now we

are having equally damaged brains and you are welcome! I thank Csaba Josza, Jean-Paul Adam, Vincent Castel I was afraid that they will be very serious but I think the discussions in our office were hilarious! Thank you Paul Zomer, Joost Flipse, Jasper van den Berg for letting me in dutch culture. You are the first few dutch friends I made. I want to thank Nilesh Awari (You will be a Dr. soon right?), you always stood by me in my tough times. I want to thank Alina Veligura, you are a dependable friend who cared and gave advices on right time to avoid mistakes and make right choices.

I thank FND group members, Frank Bakker, Bram Slachter, Subir Parui, Gaurav Rana, Saurabh Roy and so many others that it is impossible to memorize all names. Please excuse me if you don't find your name here.

I want to say thanks to Anca Dranca Iacoban and Maja Kutlaca, you were my first two friends in Groningen. You always stood by me in my thick and thin. Life in Groningen would have been difficult without you girls. Jana, I know I was a mess to share a house with but I want to give you an award and thank you for baring with me. I thank you Nikola Valacev for giving a shelter during last months in Groningen.

I also express my gratitude towards my friends Chaitanya Bivalkar, and Tanmay Desale, my family Kanchan Nalavade and Priyanka Nalawade, my cousins Mansi, Shaishavi and Shalomi, to support me by being there with my parents. I heavily depend upon them specially when I am only child and living far away from my parents.

I thank Bright Society colleagues Stijn Berden, Leon van Gerwen, Marcel Borst, Carel Verspaget for all the efforts they put to motivate me to finish my journey, and trust they had while offering me a job of a PhD when I was still improving my thesis.

Last but not the least, I thank all my friends and colleagues which made my life in Groningen not only livable but worth to maintain memories of!

Alok Chaubal

# Curriculum vitae

**Alok U. Chaubal**

| | |
|---|---|
| 20 October 1983 | Born in Mumbai, India. |
| 1989-1999 | Primary and Secondary School Education at Balmohan Vidyamandir, Mumbai, India. |
| 1999-2001 | Higher Secondary Education at D. G. Ruparel college, Mumbai, India. |
| 2001-2004 | B.Sc. in Physics with Instrumentation at D. G. Ruparel college, Affiliated to University of Mumbai, Mumbai, India. |
| 2004-2006 | M.Sc. in Physics with Electronics at D. G. Ruparel college, Affiliated to University of Mumbai, Mumbai, India. |
| 2007-2009 | Junior Research Fellow at Tata Institute of Fundamental Research, Mumbai, India. |
| 2009-2014 | Ph.D. research at the Zernike Institute for Advanced Materials, University of Groningen, The Netherlands under the supervision of prof. dr. ir. C. H. van der Wal. Subject: Electromagnetically induced transparency with localized impurity electron spins in a semiconductor. |

# List of publications

1. *Electromagnetically induced transparency with an ensemble of donor-bound electron spins in a semiconductor*
   M. Sladkov, A. U. Chaubal, M. P. Bakker, A. R. Onur, D. Reuter, A. D. Wieck, and C. H. van der Wal,
   Phys. Rev. B **82**, 121308(R) (2010).

2. *Electromagnetically induced transparency in low-doped n-GaAs*
   C. H. van der Wal, M. Sladkov, A. U. Chaubal, M. P. Bakker, A. R. Onur, D. Reuter, and A. D. Wieck,
   AIP Conf. Proc. **1399**, 1039 (2011).

3. *Polarization-preserving confocal microscope for optical experiments in a dilution refrigerator with high magnetic field*
   M. Sladkov, M. P. Bakker, A. U. Chaubal, D. Reuter, A. D. Wieck, and C. H. van der Wal,
   Rev. Sci. Instr. **82**, 043105 (2011).

4. *Electromagnetically induced transparency as probe for nuclear spin polarization around donor-bound electrons in GaAs*
   A. U. Chaubal, A. R. Onur, J. Sloot, D. O'Shea, D. Reuter, A. D. Wieck, and C. H. van der Wal,
   submitted to J. Appl. Phys.

5. *High-resolution spectroscopy of the donor-bound exciton complex in GaAs*
   A. U. Chaubal*, A. R. Onur*, D. Reuter, A. D. Wieck, and C. H. van der Wal,
   in preparation (* equal contributions).

6. *Spectral dependence of optically induced dynamic nuclear spin polarization in n-GaAs*
   A. R. Onur, A. U. Chaubal, D. Reuter, A. D. Wieck, and C. H. van der Wal,
   in preparation.